Geochronology of impact structures - constraining syn- and post-impact processes using the 40Ar/39Ar and U-Pb techniques

Herrmann, Maria

2020

Document Version:
Publisher's PDF, also known as Version of record

LITHOLUND THESES 34

Geochronology of impact structures - constraining syn- and post-impact processes using the $^{40}Ar/^{39}Ar$ and U-Pb techniques

Maria Herrmann

LUND
UNIVERSITY

Lithosphere and Biosphere Science
Department of Geology

DOCTORAL DISSERTATION
by due permission of the Faculty of Science, Lund University, Sweden.
To be defended in Pangea, Department of Geology, Sölvegatan 12, Lund,
on the 18th of September at 9:00.

Faculty opponent
Karin Högdahl
Geocentrum, Uppsala Universitet

Lithosphere and Biosphere Science
Department of Geology
Faculty of Science

ISBN 978-91-87847-48-6 (print)

ISBN 978-91-87847-49-3 (pdf)

ISSN 1651-6648

Printed in Sweden by Media-Tryck, Lund University, Lund 2015

Organization

LUND UNIVERSITY
Department of Geology
Sölvegatan 12
SE-223 62 Lund
Sweden

Author: Maria Herrmann

Document name

DOCTORAL DISSERTATION

Date of issue: 18th September 2020

Sponsoring organization: -

Title: Geochronology of impact structures - constraining syn- and post-impact processes using the $^{40}Ar/^{39}Ar$ and U-Pb techniques

Abstract

The discovery, at the beginning of the 20th century, that elements can transform into other elements, due to the spontaneous decay of an instable to a stable atomic nuclei, gave rise to a powerful source for age information in many fields of earth science. For impact structures, it is crucial to establish well-defined and precise ages in order to understand how impact events affect the Earth's geo and biosphere and also with regard to possible future events that can have devastating effects on our civilization.

During the impact cratering process immense amount of energy is released in relatively short time, resulting in extreme temperature and pressure conditions that can even melt and vaporize rocks. The thermal impact is so high that in consequence, the composition between instable and stable nuclei in a melted rock or mineral is changed due to the loss of stable nuclei through diffusion. Thus, the atomic or isotopic clock of a rock or mineral is reset and the accumulation of new stable nuclei starts again, preserving the imprint of the impact event. Traditionally, impact structures are dated by $^{40}Ar/^{39}Ar$ on impact melts. Such melts quench soon after their formation and thus, inhibit the diffusional loss of newly-formed stable nuclei. Therefore, these melts can be used to date an impact event. Further, individual minerals can yield impact-related ages, too, such as zircon. The U-Pb decay in zircon is the most widely used dating method. Due to the recrystallisation or new growth of zircon within impact melts, Pb is lost, indicating an impact relation. However, even though impact events have a devastating effect, in some cases minerals preserved in the target rock show no sign of shock, but instead, be affected by post-impact processes, such as by hydrothermal activity. Thus, impact crater ages are not always straight forward and should be interpreted with great care.

The U-Pb analyses of zircon grains from the target rock of the Siljan impact structure in Sweden can be explained by different residency time of zircon at shallow, cool crustal levels rather than by the impact event. Prior to the uplift by the impact event about 380 Ma ago, zircon grains near the crater centre resided at greater depth, where radiation-damaged lattice is able to anneal due to higher temperatures, leading to much less Pb loss. Whilst zircon grains distal to the crater centre was preserved near the erosional surface at temperatures that inhibit any annealing of radiation damage since >1260 Ma and thus, prone to lose more Pb.

The $^{40}Ar/^{39}Ar$ age data of biotite and amphibole from the Siljan target rock exclude an impact age, as well, and instead, indicate an imprint by hydrothermal fluids driven by the impact. Whilst the $^{40}Ar/^{39}Ar$ dating of whole rock impactites from the Hummeln and Mien impact structures in Sweden and the Puchezh-Katunki impact structure in Russia suggests a correlation with an impact event, even though Hummeln shows only a partial reset of the $^{40}Ar/^{39}Ar$ system and Puchezh-Katunki yield an age range between 192 and 196 Ma.

Further challenges combine dating with element mapping and microtextural analyses. Highly shocked zircon, extracted from impact melts of the Mien crater, with certain textural features can yield U-Pb ages that are impact-related. It shows that the formation of shock textures in zircon is promoted when the lattice is metamict, i.e., damaged by radiation due to the U-Pb decay.

Key words: U-Pb dating, $^{40}Ar/^{39}Ar$ dating, impact structures, impact event, hydrothermal activity, metamictization, Siljan, Mien, Hummeln, Puchezh-Katunki

Classification system and/or index terms (if any): -

Supplementary bibliographical information: -

Language: English

ISSN and key title: 1651-6648 LITHOLUND THESES

ISBN: 978-91-87847-49-3

Recipient's notes: -

Number of pages: 154

Price: -

Security classification:-

Signature: Maria Herrmann

Date: 10 August 2020

To the Earth, its the only planet with chocolate.

Contents

List of papers

This thesis is based on the five papers listed below, which have been appended to the thesis. Paper I and II have been submitted in Scientific Reports and GSA Special Papers – Proceedings in LMI VI, respectively. Paper III and IV are manuscripts to be submitted. Paper V is reprinted under permission of John Wiley and Sons, Inc.

Paper I

Herrmann, M., Söderlund, U., Scherstén, A., Næraa, T., Holm-Alwmark, S., and Alwmark, C., The effect of low-temperature annealing on discordance of U-Pb zircon ages. Submitted in Scientific Reports.

Paper II

Herrmann, M., Alwmark, C., and Storey, M., New $^{40}Ar/^{39}Ar$ data on biotite and amphibole from the Siljan impact structure, Sweden - Impact-related or post-impact hydrothermal alteration? Submitted in GSA Special Papers – Proceedings in LMI VI.

Paper III

Herrmann, M. and Storey, M., New $^{40}Ar/^{39}Ar$ dating of the Mien and Hummeln impact structures, Sweden. Manuscript.

Paper IV

Herrmann, M., Martell, J., Alwmark, C., Kenny, G., and Whitehouse, M., U-Pb systematics of shocked zircon from the Mien impact structure, Sweden: Implications for a new impact age and for metamict-induced zircon texture formation during impact event. Manuscript.

Paper V

Holm-Alwmark, S., Alwmark, C., Ferrière, L., Lindström, S., Meier, M. M. M., Scherstén, A., Herrmann, M., Masaitis, V. L., Mashchak, M. S., Naumov, M. V., and Jourdan, F., 2019, An Early Jurassic age for the Puchezh-Katunki impact structure (Russia) based on $^{40}Ar/^{39}Ar$ data and palynology. Meteoritics and Planetary Science 54, 8:1764-1780. DOI: 10.1111/maps.13309.

Acknowledgments

First of all, I want to thanks that I was given the chance to do my PhD at the Department of Geology at Lund University. A chance to do new experiences, manage new challenges (otherwise life would be boring), and meet new friends, as well as a chance to meet a new country, its culture and learn a new language. Yes Swedish, so far the funniest and most melodic language (no surprise that Sweds like the Eurovision Song Contest) that I have learned. Even though the beginning was not easy, I enjoyed the last years and I am thankful to be in Sweden, which gave me calm in my life after a turbulent time and a second home. Next, I am thankful for my PhD project about the dating of impact structures. It opened my eyes to a new research field and gave me the chance to travel to different places in the world, join in conferences and meet a small research community giving me the opportunity to learn more about this topic. I enjoyed to work on this project the last years and hopefully still keep my interest in this topic in the future.

Science is never done alone and analyses and interpretation of data only works in team. Therefore, I want to thank for the huge support of all my supervisors. First of all, I want to say thank you to Carl, my main supervisor, for all his time, comments and reading of my emails, manuscripts and in particular my Kappa during the vacation (sorry for still keeping you busy during your last vacation), and that you let me work freely without any pressure. I know you could not help so much with dating, but you were a huge help for the shocking part of my PhD. Furthermore, I want to thank you to cheer me up when the first manuscript was rejected two times, for your moral support, e.g., coming to non-essential talks like the literature seminar and for your continuous pushing of Ulf and Anders to read my first manuscript. Just great thanks that you have been a great supervisor the last years.

Anders and Ulf, I cannot stress enough how grateful I am for your help, time, comments and patience to write the first manuscript, even though every time when I came to you because I did not understand your comments. Thanks you that you did not lose your interest in that manuscript after the two rejections. Let's hope it getting through this time. Also a special thanks to Ulf that you find some time in your vacation to comment the U-Pb chapter of my Kappa. I wish to thank Michael, my co-supervisor from Copenhagen, for all your time and help in the $^{40}Ar/^{39}Ar$ lab to analyses my samples for the second and third manuscript and explaining me things about

the instrumentation. I know many things changed at the museum which kept you busy all the time, but thanks that you still took the time to read and comment my manuscripts and in particular to spend time during your vacation to read the $^{40}Ar/^{39}Ar$ chapter of my Kappa. A special thanks also goes to Sanna. Even though you were not one of my supervisors, you still gave me advices that were helpful for my PhD.
I also want to thank other people for their help in different labs to realize the numerous analyses of my PhD project, Daniel Wielandt for the sample preparation for the $^{40}Ar/^{39}Ar$ analyse in Copenhagen, Tomas Næraa for his assistance in the LA-ICP-MS lab in Lund and comments to the first manuscript as well as Martin Whitehouse, Heejin Jeon and Gavin Kenny from the NordSIMS facility in Stockholm for the SIMS analyses of zircon samples for my fourth manuscript.
From the Department of Geology in Lund I have to thank all the staff that still keep the business running, first of all the Kansli, in particular Mikaela and Ylva for their help and patience to answer everytime the same questions and help with the bureaucracy, such as fill the form for travel expenses (until today I still do not know what the difference between breakfast with and without benefits is). Without a computer a PhD thesis cannot be written and therefore I wish to thank Gert to solve all my computer problems, I thank Per-Erik for each 'God morgon' when I made my tea, Britta for all issues related to the library, and Git and Åsa for lab-related issues at the beginning of my PhD. Also thanks to all other people of the Department of Geology, in particular Lotta, Leif, Mats, Sylvian, Paula, Johan, and Mikael, that gave me a good time the last years and facilitated a friendly working at the department.
Even though the department enabled a relaxing working environment for me, but still a PhD can be stressful. Therefore, a special thanks goes to all the trainers of Gerdahallen. Everytime when I joined your courses, in particular, Bodypump, Bodycombat, HIT and Core, it got me down (perfect stress relieve) and kept me mentally up, especially at the end of my PhD when I had to finish my thesis. You are doing a great job.
What is life without friends, yes sad and boring. I wish to thank all PhD students and Post-docs of the department for all the beers on the Friday evenings. You gave me a great time the last years. A special mention has to go to all my office mates that I had the last years. At the beginning Johan, Anders and Ashley that gave me a funny and crazy time (you are awesome guys) and at the end Ingrid, Josefin and Cindy, tolerating my stinky clothes after my work out in the gym, and all the discussions with Josefin about impact-related and non-impact-related things that I liked. You all are great. A special thanks of course goes to Carla, thanks for being an awesome flatmate, to Petra, thanks for all the delicious cakes and kite surfing, and to Dr. Franzi and Datt Tjördis, thanks for all the German trash evenings (I just say: "Heute habe ich leider keine Rose fuer dich"). Thanks for all the evenings in Tugg, Rosegården and Mui Gong. Thanks to Mui Gong for the best noodle soup in the whole world.
Ich danke meinen vier Eltern, dass ihr einfach immer fuer mich da seid und mich immer unterstuetzt habt und ich weiss dass ihr es auch weiterhin tun werdet. Ich weiss Mama, dass du mich oft sehr vermisst und es am liebsten hättest, dass ich in deiner Nähe wohne und ich weiss, dass ihr alle wuenscht, dass ich öfter zu Besuch vorbeikomme. Danke, dass ihr die Entfernung mit macht und natuerlich seid ihr jederzeit Willkommen mich in Schweden oder wo auch immer ich dann landen werde zu besuchen.
The last person that I want to address is Håse(li). I cannot stress out how grateful I am that you support my decision to move to Sweden that I can do my PhD and still keeping up the long distance relationship with me. You change your life and move/moved to Berlin just to have a better connection to visit me wherever it will be in the future. I thank you for each trip that you do just to see me and for all your understanding, in particular in the last time. I am so thankful that you are just being there and for all your love. Yes, you are the best boyfriend of the whole universe and of all parallel universes, too.

Basic definitions and abbreviations

Here are the definitions and abbreviations of terms used in this thesis.

Hypervelocity impact body: A cosmic projectile with a minimum diameter of 50 m for stony and 20 m for iron meteorites (Osinski and Pierazzo, 2013) to be capable of passing the Earth's atmosphere with no energy loss and thus, strike the surface at its original cosmic velocity of >11 km/s (French, 1998), generating high-pressure shock waves in the target. Due to the high energy loss when passing the atmosphere, a smaller projectile is only able to produce a so-called 'penetration crater' where no shock waves are generated (Osinski and Pierazzo, 2013).

Asteroid: A small object consisting of rocky material and probably be a fragment of planetesimals. The size in diameter range from a few kilometres to a few tens of kilometres. The largest known asteroid is Ceres with a diameter of 1000 km. The majority of asteroids, in particular the larger objects, stem from the Main Asteroid Belt located between Mars and Jupiter (French, 1998).

Comet: A small object consisting of rocky material and volatile ice, with a diameter of tens of kilometres. When approaching the sun, the volatile ice starts to evaporate which produces the shining tail of comets. The size in diameter reaches about tens of kilometres. There are two types of comets 1) short-period comets orbiting the sun within a few years on small, near-circular orbits. An example of a short-period comet is Comet Halley with a complete orbiting around the sun in less than 200 years. 2) long-period comets need thousands of years for a complete orbit around the sun, e.g., Comet Hale-Bopp. Their orbit is highly elongated and reaches far beyond Pluto (French, 1998). There are two sources for comets 1) The Oort Cloud, a cloud of comets surrounding the Solar system at 50000 AU. 2) The Kuiper Belt, which exist beyond Neptune. Presumably, short-period comets come from there (French, 1998).

Tektite: An impact glass, consisting of impact melt and gaseous material, which was ejected ballistically during the crater formation and deposited far away from the crater in so-called strewn fields (Osinski and Pierazzo, 2013). Due to its travel through the air it often has an aerodynamic shape. The colour range from black to green. So-called microtektites, mm to dm-sized glassy particles, are brown or grey and occur in deep-sea sediments (Osinski and Pierazzo, 2013). Tektites have a high chemical resistivity and to devitrification. Their chemistry is characterized by a high Fe^{2+}/Fe^{3+} ratio, low volatile content and less than 0.02 wt% (200 ppm) H_2O (Osinski and Pierazzo, 2013). Based on their appearance they are divided into three types 1) Splash forms; the most common forms are teardrops, spheres, dumbbells, and bars. 2) Aerodynamic forms; they are similar to splash-shaped tektites but with signs of atmospheric ablation like pits, grooves, notches and flanged button shapes. And 3) Muong Nong; tektites that are only found in Asia with a blocky shape and layered vesicular texture (Osinski and Pierazzo, 2013).

Spherules: Glassy to microcrystalline, mm-sized spherical particles occurring in thin, discrete layers. Globally deposited spherules are probably the product of condensed rocks that vaporized during a large impact event (Osinski and Pierazzo, 2013). Whilst spherules less widely deposited from a crater are probably impact melts ejected ballistically during the crater formation. They are called melt droplets (Osinski and Pierazzo, 2013).

P: Pressure
T: Temperature
PDF: Planar deformation features
FRIGN zircon: Former reidite in granular neoblastic zircon

Isotope: A series of atomic species of an element that have the same nuclear charge, i.e, the same number of protons in the nucleus, but due to a different number in neutrons, they differ in their nuclear masses. Isotopes were discovered by Soddy and Fajans in 1913 (Davis et al., 2003; Schoene, 2014).

Decay rate, also defined as activity, is the number of radioactive isotopes that are counted per time unit. It can be expressed by *half-life* ($T_{1/2}$), *mean-life* (τ) and the *decay constant* (λ). The *half-life* represents the time that has passed after one-half of radioactive parent isotopes is decayed to radiogenic daughter isotopes. The *mean-life* of a radioactive isotope represents its life expectancy. Both half-life and mean-life are related to the *decay constant*, where the mean-life is equal to the reciprocal of the decay constant (Faure and Mensing, 2005),

Half-life:

$$T_{1/2} = (\ln 2)\lambda^{-} = 0.693\lambda^{-}$$

Mean-life:

$$\tau = \lambda \int_0^{\infty} te^{-\lambda t} dt = -[(\lambda t + 1)\lambda^{-} e^{-\lambda t}]_0^{\infty} = 1\lambda^{-}$$

The unit of the decay constant is the inverse of time: 1/s.

T_C: Closure temperature
FE-SEM: Field Emission-Scanning Electron Microscope
EBSD: Electron Backscatter Diffraction
SE: Secondary Electron
BSE: Backscatter Electron
CL: Cathodeluminescence
ID-TIMS: Isotope Dilution-Thermal Ionisation Mass Spectrometry
LA-ICP-MS: Laser Ablation-Inductively Coupled Plasma-Mass Spectrometry
SIMS: Secondary Ion Mass Spectrometry
$^{40}Ar^{*}$: Radiogenic argon
$^{39}Ar_K$: Neutron-generated ^{39}Ar through decay of ^{39}K
n: Neutron
p: Proton
β^{-}: Electron
d: Deuteron
α: Alpha particle
β^{+}: Positron
γ: Gamma particle
σ: Sigma error

Argon sources: : According to McDougall and Harrison (1999) it can be distinguished between different types of argon.

1) Atmospheric argon representing the isotopic composition in today's atmosphere.
2) Trapped argon is initial incorporated argon at that time when the mineral/rock is formed or due to following events. In terrestrial samples it has an atmospheric composition of $^{40}Ar/^{36}Ar$ = 298.56 ± 0.31 (Lee et al., 2006). Whilst in extraterrestrial samples the $^{40}Ar/^{36}Ar$ composition is different, often about 1.
3) Radiogenic argon comes from the in-situ ^{40}K decay in a sample.
4) Cosmogenic argon is formed due to cosmic rays which interact with an atomic nucleus, e.g., calcium, titanium, or iron. Reactions are spallation or neutron capture. It is significant for extraterrestrial material.
5) Neutron-induced argon is formed, due to the interaction between neutrons and potassium, calcium, and chlorine, during the irradiation in a nuclear facility.
6) Extraneous argon, including excess and inherited argon, is a kind of trapped argon, but yielding $^{40}Ar/^{36}Ar$ ratios significant above the atmospheric composition (298.56 ± 0.31, Lee et al., 2006). Excess argon is introduced in to the system from outside, e.g., fluid inclusions (Kelley, 2002b). Inherited argon as physical contamination, e.g., dis-equilibrated clast in impact melt (Jourdan et al., 2012), is an argon reservoir already present in the system (Kelley, 2002b)

1. Introduction

Impact structures are formed by an unusual geological process where the sudden release of immense amounts of kinetic energy concentrated in a point lead to physical conditions far beyond normal processes on Earth, which have an instantaneously devastating effect on the environment and change it within seconds. As we humans are incapable of imaging that such an enormous destructiveness can ever happen, impact events are more seen as science fiction and a good theme for disaster movies. However, the Chelyabinsk event in 2013 (e.g., Popova et al., 2013) or the Tunguska event in 1908 (e.g., Longo, 2007) remind us that such impact events are real and can even happen in modern times. Both events were caused by smaller objects, i.e., 10-100 m in diameter (Artemieva and Shuvalov, 2016), that exploded as airbursts in the Earth's atmosphere. Even though they did not strike the surface directly, however, their energy release, between 0.5 (Chelyabinsk) and 20.0 (Tunguska) megatons TNT (Artemieva and Shuvalov, 2016), was still sufficient enough to produce shock waves which caused tremendous destruction in over large areas. In the case of Tunguska, an area of over 2000 km^2 was destroyed (Gasperini et al., 2007).

The impact crater record, according to Schmieder and Kring (2020), currently counting 200 confirmed impact structures, shows that the Earth has always been a target and in particular large objects, i.e., several kilometres in their diameter, have destroyed, altered and shaped the surface of the Earth continuously. On other planets, with no atmosphere or tectonic activity, impact cratering is often the only surface-modifying process. Fortunately for us, bigger events on Earth are rare. However, we know of at least one big event that triggered a biological crisis on Earth. It was about 66 Ma ago (Alvarez et al., 1980), when a ~10 km-sized asteroid collided with the Earth just outside of Yucatan, Mexico, and produced the 150 km-wide Chicxulub crater (Schulte et al., 2010). Climate-sensitive gases, such as CO_2 and SO_2, and dust were introduced into the atmosphere causing darkness, global cooling, and acid rains (Schulte et al., 2010, and references therein). The majority of the terrestrial and marine life forms were eradicated, including the dinosaurs (Schulte et al., 2010). This event led the biological evolution on Earth in to a new direction towards the rise of the mammals (Meredith et al., 2011), including humankind. Today, this Cretaceous-Paleogene mass extinction is visible in the stratigraphic records around the world, e.g., Stevns Klint, Denmark (Sepúlveda et al., 2009). Beside the geological and biological significance, impact craters are also of economic importance. The formation of huge volumes of igneous rocks during a large impact event can lead to the formation of ore deposits (French, 1998). Fractured rocks can serve as traps for hydrocarbons and locally impact-generated rocks are often used as building stone, e.g., the Suevite from the Nördlinger Ries impact structure, Germany (French, 1998). For instance, at the Sudbury impact structure, Canada, about $1.65x10^9$ tons of ores are mined with 1.2% Ni and 1.1% Cu with an average value of about two billion US-dollars per year (Grieve and Masaitis, 1994; Grieve, 2005).

Since the 1960's, when the research community realized that impacts have played a major role in shaping Earth's surface and in altering its geological history, much knowledge regarding Earth's impact structures and the cratering process has been gained. However, the majority of the craters on Earth are still not well-dated or their age is even unknown. As impact events are part of the Earth's history and will be involved in shaping the future, it is crucial to determine accurate and precise ages of impact structures in order to constrain an impact crater rate through time and thus, develop a database for an impact periodicity, in particular, to infer to potential bigger events in the future. Further, for the understanding how such events affect the Earth's geosphere and biosphere, especially with regard to biological crisis such as the Cretaceous-Paleogene mass extinction, a well-established dating of impact structures is needed.

This thesis is focused on the dating of three Swedish impact structures (Siljan, Mien, and Hummeln), and one Russian impact structure (Puchezh-Katunki). Besides mineralogical investigations by optical microscopy and scanning electron microscopy, the main research was performed on radiometric age determination using the U-Pb and $^{40}Ar/^{39}Ar$ method. Both individual mineral grains, such as zircon, amphibole, and biotite, separated either from the target rock or impact melts, and the impact melts themselves as whole rock material were used for the dating. The aim of this thesis is to investigate to what extent isotopic systems, such as the U-Pb and the K-Ar system, can be affected by syn and post-impact impact processes and in the best case show a complete reset, i.e., fully loss of daughter isotopes and re-start of the isotopic clock, which can be correlated with an impact event. In particular, the isotopic systems of different mineral phases from the Siljan impact structure are studied, to see whether they behave in a contrasting way in their resetting between inside and outside the crater and to clarify potential reasons for the differences. Uranium-lead and $^{40}Ar/^{39}Ar$ studies on zircon and impact melts, taken from Mien, Hummeln and Puchezh-Katunki impact structures, are conducted to clarify the ages of the respective impact events. Four manuscripts and one co-author paper build the basis for this thesis, which are summarized in chapter 8. Abstracts that are produced during my PhD-studies can be found

in Supplementary A. The research presented in this thesis was partly funded by contributions from the Kungliga Fysiografiska Sällskapet i Lund, Bokelunds Resestipendie fond (Research and travel grants of the Faculty of Science), and travel award from the Barringer Crater Company, the IRD-French National Research Institute for Sustainable Development, and the Meteoritical Society.

2. Impact structures

Impact structures are orbicular geological depressions at the surface of terrestrial planets (Fig. 2.1) generated by the collision between a hypervelocity impact body (projectile), e.g., asteroid or comet, and a planetary object (target), e.g., Earth (Osinski and Pierazzo, 2013).
On Earth, it is distinguished between simple and complex impact structures (Fig. 2.1), where the simple structures form small (diameter <2-4 km), bowl-shaped depressions with an uplifted rim (Fig. 2.1A, C, E) and crater filling consisting of impact breccias mixed with melt material (see chapter 3.3; French, 1998; Osinski and Pierazzo, 2013). Complex impact structures are large craters (diameter >2-4 km) with a flat profile, an uplifted central part surrounded by an annular trough and a structural complex, terraced rim (Fig. 2.1B, D, F; French, 1998; Osinski and Pierazzo, 2013). The central uplift consists of deep-seated material which moved upward near the surface during the crater formation process. Thus, such structural uplifts provide a seldom insight into deeper crustal levels (French, 1998; Osinski and Pierazzo, 2013). Further crater types are peak-ring and multi-ring basins. Both are made up by one or several uplifted rings, respectively, that are concentric concentrated around the crater centre. The rings are separated by down-faulted valleys (ring-graben) (French, 1998; Osinski and Pierazzo, 2013). The most prominent peak-ring structure on Earth is the Chicxulub impact structure, Mexico. Whilst multi-ring basins so far are observed only for other planetary bodies such as Moon, Mercury or Mars (French, 1998; Osinski and Pierazzo, 2013). Most of them were formed during the early stage of the Solar system (>3.9 Ga), when large projectiles with a diameter of several hundreds of kilometre and their collision with other planetary objects were more likely (French, 1998).

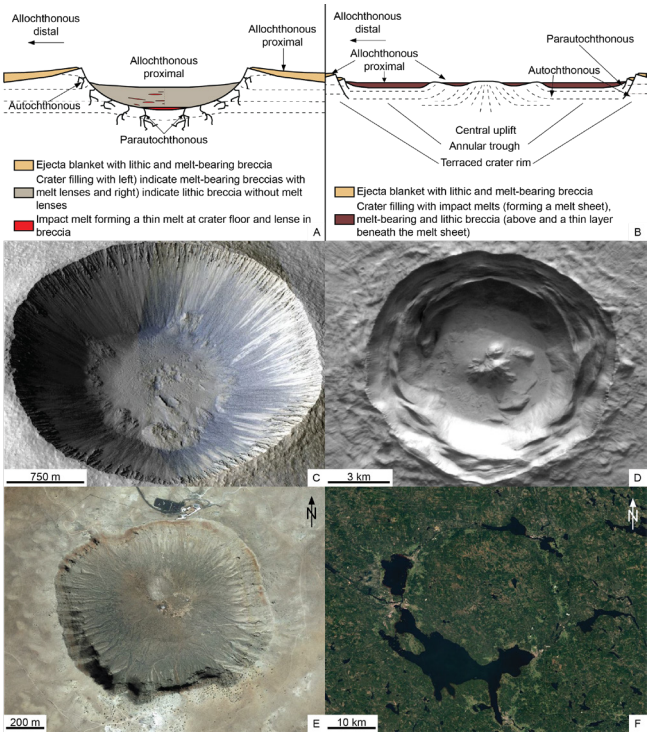

Figure 2.1 Schematic cross sections through A) simple impact structure showing a bowl-shaped crater with an uplifted crater rim and, B) complex impact structure with a shallow profile, an uplift in the central part surrounded by an annular trough and a terraced crater rim. Both figures show the positions of the different impactites where they deposited during the crater formation. C) The simple bowl-shaped crater Zumba on Mars. Colorized 3D Model by NASA/JPL/UA (11/03/2020: https://scitechdaily.com/a-connection-between-volatiles-in-the-subsurface-of-mars-and-the-impact-process/). D) Complex crater on Mars showing central uplift in the middle of the crater and a structural complex crater rim. Taken by NASA/JPL-Caltech/Arizona State University (11/03/2020: https://marsed.asu.edu/mep/craters/complex-craters). E) Meteor crater, USA, a young terrestrial simple bowl-shaped crater where the circular crater form is still preserved (11/03/2020: Google Earth, 35°01'39.69"N and 111°01'19.20"W, elevation 1565 m). F) Remnants of the complex Siljan impact structure, Sweden. The image shows the central part of the crater which was uplift during the event about 380 Ma ago (Reimold et al., 2005; Jourdan et al., 2012) surrounded by an annular trough, recently partly filled with lakes (11/03/2020: Google Earth – Lantmäteriet/Metria, Maxar Technologies, CNES/Airbus, 60°57'23.56"N and 14°55'43.99"E, elevation 214 m).

2.1 Crater formation

In contrast to endogenic processes on Earth, e.g., tectonic deformation or metamorphism, the crater formation is instantaneously. It takes between a few seconds to minutes for a large crater to form (French, 1998; Osinski and Pierazzo, 2013). Upon impact, the sudden energy release (between 11.0 and 8.7×10^7 megatons, about 5.5×10^{-4} to 4.4×10^3 megatons times the atomic bomb explosion in Hiroshima; French, 1998), concentrated in a relatively small point, lead to the formation of a shock wave accompanied by pressure and stress conditions exceeding that of

normal geological processes (French, 1998). For instance, the lithostatic pressure, compressing rocks due to superimposed load, reach a maximum pressure of 1 GPa, however, the pressure of an impact event rises up to several hundred gigapascal (French, 1998). Further, the strain rate of normal deformation is about 10^{-3} to 10^{-6}/s, whilst the strain rate during the crater formation lie between 10^{4} and 10^{6}/s (French, 1998). The expanding shock wave, moving with supersonic velocity through the target material, not only causes a permanent and unique change in the rocks and minerals (see chapter 3), but also induces the movement and excavation of the target and in consequences the crater formation (French, 1998). The crater formation process can be divided in three stages:

2.1.1 Contact and compression stage

When the projectile impacts the planetary object, it penetrates about one to two times its diameter beneath the target surface (Fig. 2.2A; Osinski and Pierazzo, 2013). Thus, the projectile is stopped abruptly and all its kinetic energy is transferred into the target, leading to the formation of a shock wave at the contact between the projectile and target (French, 1998; Osinski and Pierazzo, 2013). The shock waves expand in both projectile and target where they induce extreme compression of the material with pressures of several hundred gigapascal and temperatures of up to 10000 K (Osinski and Pierazzo, 2013). These pressures and temperatures lie far above the conditions reached in the Earth's core with P = 350 GPa and T = 5000 K (Osinski and Pierazzo, 2013). In the target, due to the overall decrease in the energy density, heating, deformation and acceleration of the material, the energy of the shock waves decrease outwards from the impact point. Correspondingly, the shock pressures decrease exponentially with greater distance to about 1-2 GPa (French, 1998). At this point, the shock wave change to seismic waves and rather cause fracturing of the target material than permanent physical changes and shock effects as near the impact point (French, 1998). In the projectile, the shock wave is reflected at the free surface and move back as a rarefaction wave into the interior, inducing a decompression from the strong compressed state and thus, an unloading of the projectile from the high shock pressures. This results in melting, and vaporization and finally complete destruction of the projectile, marking the end of the contact and compression stage (French, 1998; Osinski and Pierazzo, 2013). The entire process of contact and compression occurs within seconds. For instance, when a 10 km-wide projectile strikes the Earth's surface with a cosmic velocity of 20 km/s, the contact and compression will be done within 0.5 sec, e.g., similar for the Cretaceous-Paleogene event about 66 Ma ago leading to the formation of the Chicxulub impact structure, Mexico (Osinski and Pierazzo, 2013).

2.1.2 Excavation stage

The contact and compression stage continues gradually into the excavation stage, where the crater is opened up due to the expanding shock waves (Fig. 2.2B; French, 1998; Osinski and Pierazzo, 2013). At this stage, the disrupted projectile is part of the vapour plume formed above the potential crater und thus, is not further included in the formation processes (French, 1998). The shock wave propagates radially from the impact point and form a hemisphere in the target. Its centre is located beneath the target surface from which the shock waves induce that the target material moves outwards in a radial manner, as well. When the shock wave reaches the free surface, it is reflected as a rarefaction wave backward into the target, causing fracturing and shattering of the near-surface target rocks (French, 1998; Osinski and Pierazzo, 2013). The inward-directed rarefaction wave act against the outward and upward movement of the shock waves. This complex interplay transfers kinetic energy to the target rocks finally resulting in their excavation and thus, to the formation of a bowl-shaped depression in the target, called transient cavity (transient crater) (Fig. 2.2B; French, 1998; Osinski and Pierazzo, 2013). Within the upper part of the transient cavity, the velocities are high enough to eject target material ballistically beyond the crater rim (Fig. 2.2B; French, 1998; Osinski and Pierazzo, 2013). In the proximity of an impact structure, it forms ejecta blankets (see chapter 3.3), whereas distal ejecta, e.g., tektites and spherules, can be deposited several hundreds to thousands of kilometres from the crater (see chapter 3.3; Osinski and Pierazzo, 2013). In contrast, within the lower part of the transient cavity, the displaced zone, the excavation flow is too low to displace any material outside the potential crater rim (Fig. 2.2B). The target rocks remain within the structure with some coherent upward and outward moving and thus, build part of the later crater filling (French, 1998; Osinski and Pierazzo, 2013). During the propagation of the transient cavity, target material is excavated continuously until its maximum expansion, where the energy of the shock and rarefaction wave is no longer high enough to displaces target rocks, but the gravity does not affect them yet (French, 1998; Osinski and Pierazzo, 2013). It represents the end of the excavation stage (French, 1998; Osinski and Pierazzo, 2013). The excavation and opening of the crater lasts several minutes, e.g., a transient cavity with a diameter of 200 km and an average excavation flow of 1 km/s is excavated within 2 min (French, 1998).

2.1.3 Modification stage

The transition from excavation to modification is continuous, as the modification starts when the transient cavity still expands (Fig. 2.2C; French, 1998; Osinski and Pierazzo, 2013). Modification means the change of the shape of the transient cavity to its final crater form (Fig. 2.2D; French, 1998; Osinski and Pierazzo, 2013). The energy of the shock and rarefaction wave has dropped so far that both are now seismic waves and thus, do not play any further role. Instead, gravity, other rock mechanics, and endogenic processes, e.g., isostatic uplift, erosion, mass flow, and sedimentation, shape the final crater (French, 1998; Osinski and Pierazzo, 2013). Small impact structures (diameter <2-4 km) are less modified and build the simple, bowl-shaped craters, where the transient cavity forms more or less the final rim. The upper crater walls of the transient cavity collapse gravitationally and the material slumps inward, where it forms, together with impact breccia mixed with melt material (see chapter 3.3), the crater filling (Fig. 2.2D; French, 1998; Osinski and Pierazzo, 2013). In contrast, larger, complex transient cavities are more unstable, where the shock wave effects, gravity and strength of the target material induce that the central part moves in and upward (Fig. 2.2D). Consequently, rocks deeply preserved beneath the surface are uplifted within minutes and form a central uplift (Fig. 2.2C and D; French, 1998; Osinski and Pierazzo, 2013). For instance, the deep-seated rocks of the central part of 100-200 km-diameter impact structures can be uplifted about 10-20 km relative to their original position (French, 1998). Simultaneously to the central uplift formation, the gravitational collapse of the transient cavity leads to the inward and down-faulting of target material, forming the annular trough around the uplifted crater centre (Fig. 2.2D; French, 1998; Osinski and Pierazzo, 2013). At the outer margin, the gravity causes the terrace-like formation of the crater rim (Fig. 2.2C and D; French, 1998).

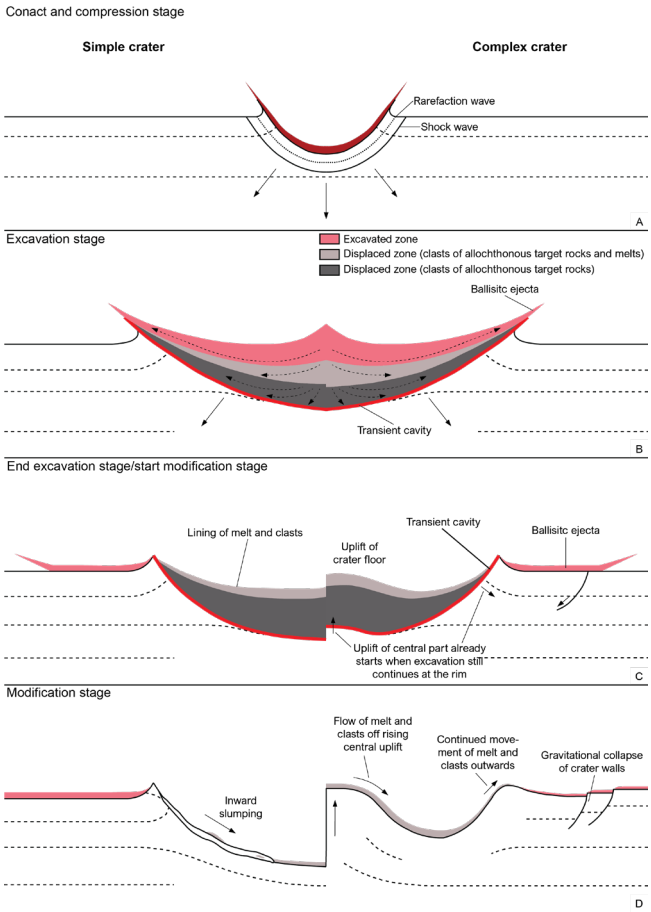

Figure 2.2 Schematic cross sections showing the three main stages, A) contact and compression stage, B) and C) excavation stage, and C) and D) modification stage, of the crater formation process. The left side depicts the formation of a simple crater and the right side of a complex crater (modified after Osinski and Pierazzo, 2013).

2.2 Identification of impact structures

Post-impact processes like hydrothermal activity, erosion, deformation, volcanic activity, metamorphism and burial processes often obliterate impact structures (French, 1998; Osinski and Pierazzo, 2013). Younger craters might still have their circular appearance where the ejecta material and other shocked rocks still occur at their original position, e.g., Meteor crater, USA (French, 1998). However, most of the older impact structures on Earth are deeply eroded with no distinctive circular crater form left. Impact breccia and melt rocks are often only preserved as remnants or are even completely removed. The central uplift surrounded by a circular fracturing pattern is often the only remaining rest of a larger, complex impact structure (e.g., Fig. 2.3A). Some impact structures are buried due to post-impact sedimentation and therefore, are not even exposed at the surface, e.g., Chicxulub impact structure, Mexico (French, 1998). Thus, the identification of impact structures is quite challenging and should follow certain criteria that are diagnostic for impact events.

Circular structures with strong fracturing, faulting, brecciation and 'unusual' igneous rocks, identified by remote sensing, e.g., air imagery, or field studies, can be a lead to an impact structure. However, numerous endogenic processes, e.g., volcanic calderas or craters, diatremes, igneous intrusions, salt domes, tectonic deformation, and erosion produce circular topographies, as well (Fig. 2.3A-J; French, 1998; French and Koeberl, 2010; Osinski and Pierazzo, 2013).

The intense brecciation and fracturing of the rocks beneath the crater floor and the crater fillings, consisting of impact breccias, melts, and also post-impact sediments, can change the geophysical properties of the rocks within and near a crater, seen as gravitational and magnetic anomalies (Fig. 2.4A-D; French, 1998; Osinski and Pierazzo, 2013). Due to the strong fractured and there-

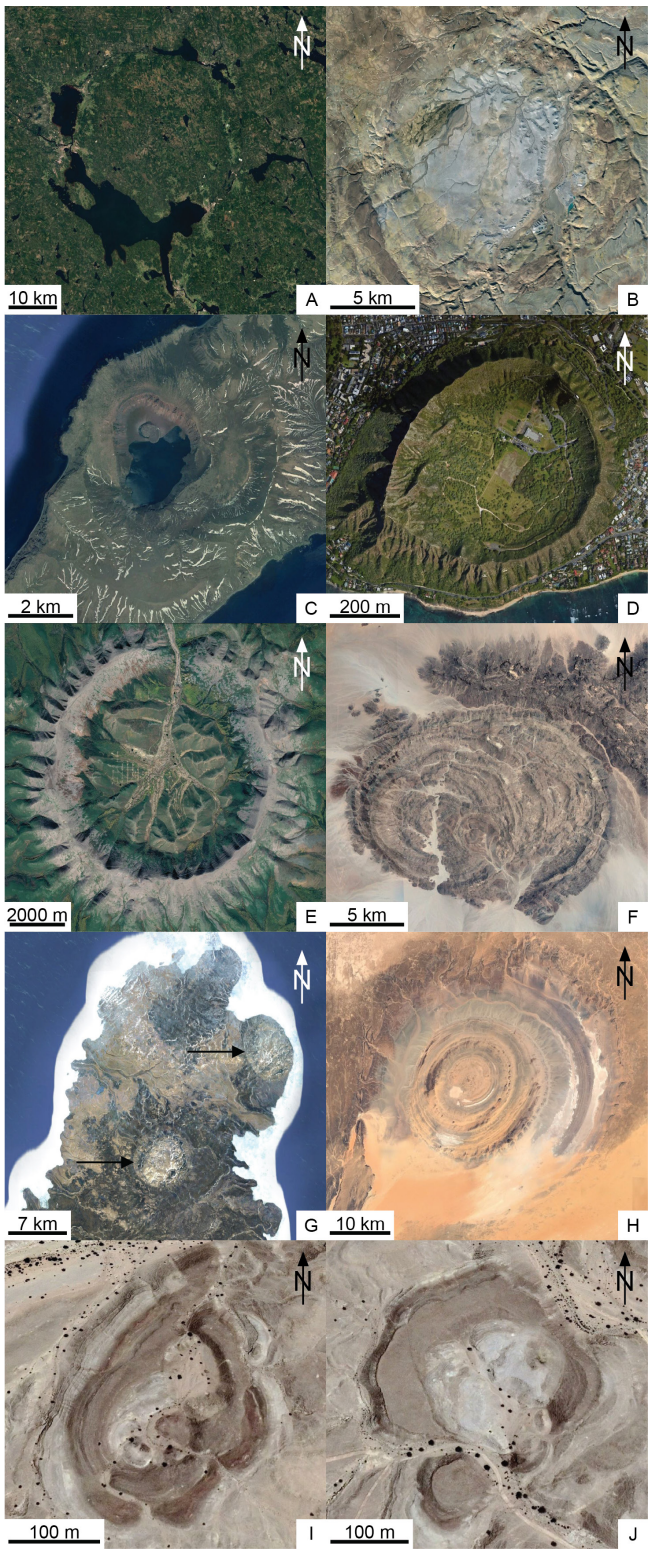

Figure 2.3 Different circular morphological structures in comparison to the A) Siljan impact structure, Sweden, (11/03/2020: Google Earth – Lantmäteriet/Metria, Maxar Technologies, CNES/Airbus, 60°57'23.56"N and 14°55'43.99"E, elevation 214 m) and B) Haughton impact structure, Canada (11/03/2020: Google Earth - Maxar Technologies, Landsat/Copernicus, 75 °22'22.32"N and 89°39"00.16"W, elevation 149 m). C) Zavaritski caldera, located in the central part of Simushir Island, Kuril Islands, Russia (11/03/2020: Google Earth – TerraMetrics, Maxar Technologies, 46°54'43.21"N, 151°58'15.19"E, elevation 258 m). D) Diamond Head, a volcanic crater on the Hawaiian island O'ahu (11/03/2020: Google Earth, 21°15'40.62"N and 157°48'19.64"W, elevation 66 m). E) Kondyor Massif, a circular igneous intrusion, located in Khabarovsk Krai, Russia (11/03/2020: Google Earth - Landsat/Copernicus, Maxar Technologies 57°36'23.19"N and 134°33'41.62"E, elevation 1037 m). F) Jabal Arkanu, a circular-like igneous intrusion in the Libyan desert 50 km West to the Egypt border (11/03/2020: Google Earth – CNES/Airbus, Maxar Technologies, 22°20'13.37"N and 24°34'33.69"E, elevation 562 m). G) Two salt dome structures (black arrows), Melville Island, Canada (15/04/2020: Google Earth – Landsat/Copernicus, 76°41'07.35"N and 108°52'51.89"W, elevation 39 m). H) Richat Structure, also called Eye of the Sahara, is a deeply eroded structural dome (11/03/2020: Google Earth – CNES/Airbus, Maxar Technologies, 21°05'10.60"N and 11°21'12.68"W, elevation 425 m). I and J) Circular collapse structures in a near-surface karst system, both located in the East of the Saudi Arabia peninsula (I: 11/03/2020: Google Earth – CNES/Airbus, 22°19'11.70"N and 46°14'19.23"E, elevation 831 m; J: 11/03/2020: Google Earth – CNES/Airbus, 22°19'56.69"N and 46°14'16.31", elevation 838 m).

fore, less dense rocks below the crater floor, small impact structures commonly show a negative gravity anomaly, which often matches the limits of the crater boundary. Whilst central uplifts, consisting of deep-seated and thus, denser rocks, yield a positive gravitational anomaly in the centres of large impact structures (French, 1998; French and Koeberl, 2010; Osinski and Pierazzo, 2013). Magnetic anomalies are less specific, but some larger impact structures show a strong negative anomaly (e.g., Fig. 2.4D), due to the chaotic lithology in and around the crater, which lowers the magnetic susceptibility (French, 1998; Osinski and Pierazzo, 2013). However, geophysical investigations can only give a clue to a potential impact structure and in particular to locate buried or submarine structures, e.g., Chicxulub impact structure, Mexico (Fig. 2.4A and B).

In order to verify a structure as impact-related the proof relies on the finding of distinctive geochemical signatures or shock metamorphic features. Therefore, the sampling of an impact structure is crucial. Distinctive geochemical signatures can be produced either by fragments of the projectile that survived the impact event or by the destroyed and vaporized projectile which has been incorporated in impact breccias, impact melts and ejecta material (French and Koeberl, 2010; Osinski and Pierazzo, 2013). Projectile fragments are rarely preserved and are mostly destroyed due to melting and vaporization during the crater formation or by post-impact weathering. Remnants of projectiles can be found in small and younger craters, e.g., Meteor crater, USA or Kaali crater, Saaremaa, Estonia (Fig. 2.5A and B), and in the dry climate of deserts or in the polar regions (French and Koeberl, 2010). However, even in those extreme environments, a projectile fragment commonly does not survive more than ~50 ka (French and Koeberl, 2010). Older meteorite fragments are known from the Cretaceous-Paleogene boundary or Ordovician sediments in Sweden, where however they are strongly altered (French and Koeberl, 2010).

Up to 1 wt% of the projectile material is usually incorporated in impact breccias, impact melts, and ejecta material (French and Koeberl, 2010). This leads to an elevated concentration of siderophile elements like PGEs (Ru, Rh, Pd, Os, Ir, Pt, Ni), Cr and Co and to anomalous isotopic

ratios in Os and Cr in the impact-related rocks (French, 1998; French and Koeberl, 2010; Osinski and Pierazzo, 2013). Iridium is the mostly used of these to identify an extraterrestrial source and thus, establish an impact relation, where a concentration of "≥" 1-2 ppb is already enough (French, 1998). $^{187}Os/^{188}Os$ ratios are used to determine minute projectile material in terrestrial rocks, whereas $^{53}Cr/^{52}Cr$ and $^{54}Cr/^{52}Cr$ can distinguish between different types of projectiles or meteorites (Osinski and Pierazzo, 2013).

Shock metamorphic features can be identified both macroscopically in form of shatter cones and microscopically, e.g., PDFs in quartz, the most accepted criteria to verity a structure as impact-related (French, 1998; French and Koeberl, 2010; Osinski and Pierazzo, 2013). Further details about shock metamorphism, see chapter 3.

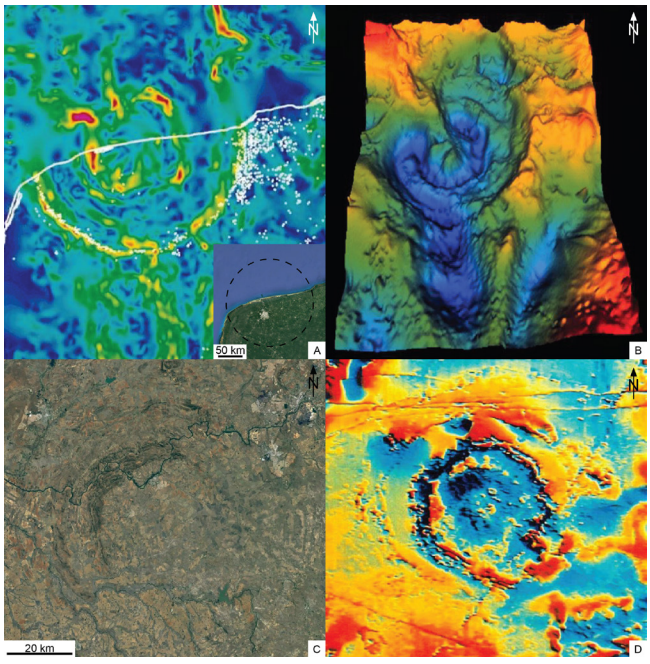

Figure 2.4 A) and B) Map of the Bouguer gravity field of the Chicxulub impact structure, Mexico. The white line in A) represents the current coastal line and the white dots water-filled sinkholes, so-called cenotes (11/03/2020: https://en.wikipedia.org/wiki/Chicxulub_crater#/ MediaFile:Chicxulub-Anomaly.jpg). The small inset shows the location of the supposed crater mark by the dotted line (11/03/2020: Google Earth – Landsat/Copernicus, 21°46'00.81"N and 90°12'03.48"W, elevation 33 m). B) shows a 3D image of the gravity field of Chicxulub (11/03/2020: https://sk.m.wikipedia.org/wiki/S%C3%BAbor:Chicxulub2.jpg). C) Vredefort impact structure, South Africa (11/03/2020: Google Earth – Landsat/Copernicus, 27°01'04.18"S and 27°29'46.64"E, elevation 1439 m). D) Map of the magnetic field of the Vredefort impact structure showing a clear circular shape with a low in the central part of the structure (11/03/2020: http://www.passc.net/EarthImpactDatabase/New%20website_05-2018/Vredefort.html).

Figure 2.5 A) and B) Fragments of meteorites from the Kaali impact structure, Saaremaa, Estonia. A) Fragment called 'Maria' with a weight of 172.2 g (found and named by the author of this thesis, 31/07/2017). B) Fragment called 'Mateusz' with a weight of 396.1 g. The size of the 2 Euro coin is about 2 cm in diameter (found 31/07/2017). Both fragments are stored at the University of Tartu, Estonia.

3. Shock metamorphism

French and Koeberl (2010) define shock metamorphism as all irreversible changes in rocks and minerals that stem from a shock wave passage, solely generated by an impact of a hypervelocity body. The extreme conditions with P = 10-60 GPa and T>1000°C, which initially can rise up to P = 100 GPa and T>2000°C at the point of impact, lie far beyond the P-T range of endogenic processes, e.g., metamorphism (P<3 GPa, T<1000 °C) or igneous activity (Fig. 3.1; Stöffler, 1971; French, 1998; French and Koeberl, 2010). The instantaneously produced shock waves travel with supersonic velocity (~10 km/s; French, 1998) through the target rock. This generates extreme P-T and stress conditions and high strain rates, that affect rocks and minerals in a tremendous way that their physical state can change permanently, resulting in textural shock features that are unique for an impact event (French, 1998; French and Koeberl, 2010).

The P-T conditions and thus, the shock metamorphic effects decrease outwards from the point of impact (progressive stage of shock metamorphism), which defines a hemispherical volume in the target rock with distinct shock pressure zones characterized by distinctive shock features (Stöffler, 1971; French, 1998; French and Koeberl, 2010). At shock pressures below 10 GPa, shatter cones (Fig. 3.2A), fracturing, twinning and deformation bands (e.g., deformation lamellae or kink bands; Fig. 3.2B and C), are generated. At pressures above ~10 GPa other features, diagnostic for a shock wave are formed. These include PDFs in quartz (10-25 GPa) (Fig. 3.2D), high-pressure phases like coesite (Fig. 3.2E) and stishovite (12-30 GPa), diaplectic glasses (30-45 GPa) (Fig. 3.2F), complete melting and even vaporization of the target rock at P>60 GPa (Stöffler, 1971; French and Koeberl, 2010). Many shock features refer to framework silicates with quartz as the most-described shocked mineral. Due to its open crystal structure, quartz responds with a high compressibility during the shock wave passage and thus, can yield a great variety of shock features from fracturing to melting (Stöffler, 1971). Mineral phases investigated in this thesis, such as zircon, biotite and amphibole, reveal

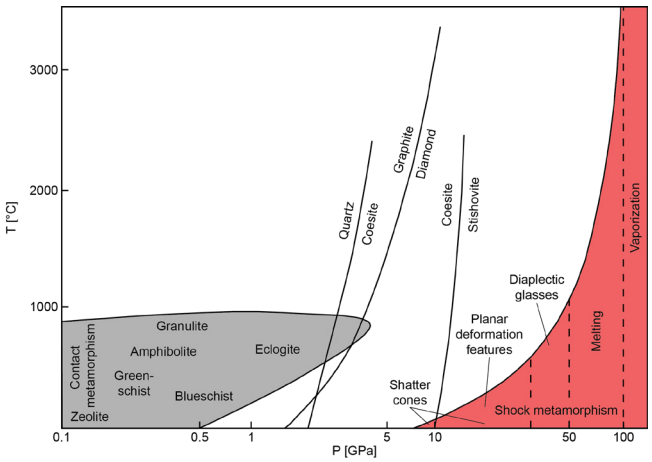

Figure 3.1 Pressure-temperature diagram showing the P-T conditions of shock metamorphism (light red field) in comparison to 'normal' metamorphism on Earth (light grey field). The pressure of the eclogite facies metamorphism reach up to maximum of 3 GPa and the temperature of the granulite facies to maximum of 1000°C. Whilst the pressure of the shock metamorphism lies between 5 GPa and exceed far above 100 GPa. The temperature can rise up to more than 3000°C. The x-axis is on logarithmic scale (modified according to Osinski and Pierazzo, 2013, and references therein).

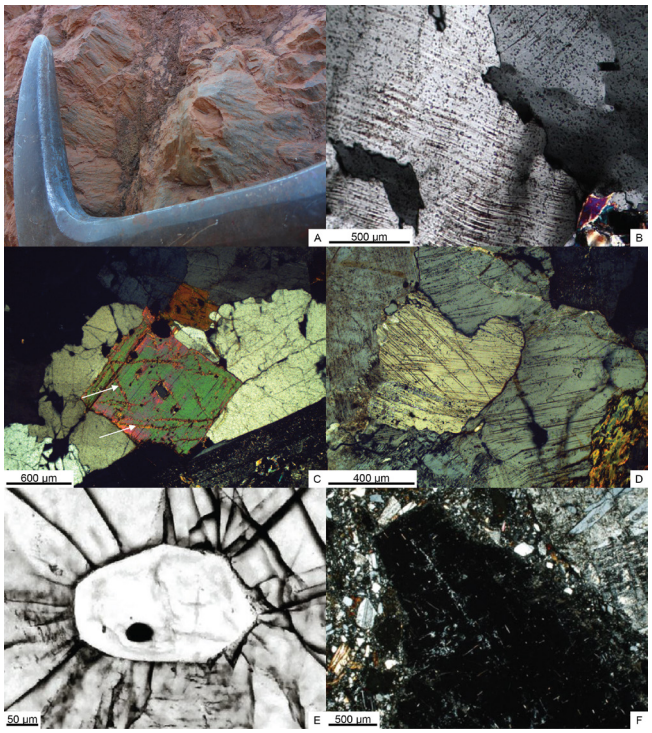

Figure 3.2 Shatter cones in metasandstone of the Cuiabá Group, Araguainha impact structure, Mato Grosss and Goiás, Brazil. The size of this part of the hammer is ~15 cm (photo: author of this thesis, 06/10/2019). B) Deformation lamellae in quartz which, however, are not impact indicators (12/03/2020: http://www.alexstrekeisen.it/immaging/meta/lamelle(salarioli) (13).jpg). C) Kink bands (white arrows) in a biotite grain from the Siljan impact structure, Sweden (photo: author of this thesis, 12/06/2017). D) Several sets of parallel, closely-spaced PDFs in quartz from the Siljan impact structure, Sweden (photo: author of this thesis, 29/05/2017). E) Coesite in garnet (12/03/2020: http://webmineral.com/specimens/picshow.php?id=2925&target=Coesite#.XmtC_Up7lPY). F) Cross-polarized light image of a diaplectic plagioclase glass clast (modified according to Pickersgill et al., 2015).

shock features, as well.

3.1 Shock features in zircon

Its variety of shock features with increasing shock metamorphism and high resistivity even under granulite facies conditions (Reimold et al., 2002), makes zircon a robust shock indicator. Depending on the P-T conditions, specific shock features are formed that are used as thermobarometer to develop P-T diagrams for zircon at extreme conditions (e.g., Wittmann et al., 2006; Timms et al., 2017). Experimentally shocked zircon grains (20-60 GPa) are described by Kusaba et al. (1985) and Leroux et al. (1999). Krogh et al. (1984) discovered the first natural shocked zircon from the Sudbury impact structure, Canada, and since then it has been reported from other structures, as well, e.g., Vredefort impact structures, South Africa (e.g., Moser et al., 2011), or Chicxulub impact structures, Mexico (e.g., Kamo and Krogh, 1995).

At shock pressures below 20 GPa common shock features in zircon are curviplanar (Fig. 3.3A) and irregular fractures (Fig. 3.3B), crystal-plastic deformation with subgrain formation and planar deformation bands (Leroux et al., 1999; Timms et al., 2017). Between 20 and 40 GPa planar features (see Paper I) and microtwins are formed (Erickson et al., 2013a; Morozavo, 2015). Planar features are multiple intersecting sets of closely-spaced, parallel, lamella with different orientations (see Paper I; Fig. 3.3C and D; Erickson et al., 2013a). Microtwins are parallel to the {112} orientation, often 65° about <110> misorientated to the host grain (Morozova, 2015). Microtwins are often associated with reidite (e.g., Moser et al., 2011; Cox et al., 2018), the scheelite-structured high-pressure polymorph of zircon, formed at shock pressures above 30 GPa (Kusaba et al., 1985; Leroux et al., 1999). Reidite was first described experimentally by Reid and Ringwood (1969) and later found naturally at the Chesapeake Bay impact structure, USA, by Glass and Lui (2001). Reidite forms lamellar, granular, partly lense-shaped domains and even completely replace zircon at very high pressures between 50 and 60 GPa (Kusaba et al., 1985; Leroux et al., 1999; Wittmann et al., 2006; Erickson et al., 2017; Timms et al., 2017; Cox et al., 2018). Above 53 GPa, and up to 94 GPa, reidite decomposes to ZrO_2 and SiO_2, which, according to Kusaba et al. (1985), is more likely temperature-driven. Kaiser et al. (2008) showed experimentally that zircon decomposition occurs at T = 1673°C. Natural decomposed reidite, to ZrO_2 and SiO_2, is first described from the Stac Fada impactites, Scotland (Reddy et al., 2015).

At the highest shock stage with temperatures above 1200°C, reidite reverts back to granular or neoblastic-textured zircon (Fig. 3.3E; Kusaba et al., 1985; Timms et al., 2017), so-called FRIGN zircon (see Paper IV; Fig. 3.3F;

Cavosie et al., 2018), where the neoblasts (small crystallites that nucleate from the host grain) preserve the crystallography of reidite (phase heritage; Timms et al., 2017) with a $<110>_{reidite}$ alignment with $[001]_{zircon}$ revealing a high misorientation angle of about 90° between adjacent neoblasts (Cavosie et al., 2018). FRIGN zircon is diagnostic for the high P-T conditions of an impact event (Cavosie et al., 2018). Other granular textures are formed either due to the recrystallization of amorphous zircon or due to ZrO_2 reaction with a Si-enriched impact melt, both initiated at temperatures above 1100°C, respectively (Wittmann et al., 2006). However, the latter can also be a product of pro-grade metamorphism where baddeleyite (ZrO_2) breaks down under the presence of Si-rich fluids to form polycrystalline zircon grains (Söderlund et al., 2008; Beckman et al., 2017).

Microporous or vesicular textures (see Paper V; Fig. 3.3G and H) are reported from different impact structures, e.g., Popigai impact structures, Russia (Wittmann et al., 2006); Haugthon impact structures, Canada (Singleton et al., 2015), Mien impact structures, Sweden (Martell, 2018), Lac La Moinerie impact structures, Canada (McGregor et al., 2019), and from lunar material (Zhang et al., 2011), but also from greenschist facies rocks (Hay and Dempster, 2009; Dempster and Chung, 2013). Previous studies (e.g., Bohor et al., 1993; Wittmann et al., 2006; Zhang et al., 2011; Singleton et al., 2015) interpreted it as a melting and degassing texture where the temperature increased near the melting point of zircon and thus, stated at the stage prior to the decomposition of zircon into ZrO_2 and SiO_2. Other studies (e.g., Hay and Dempster, 2009; Dempster and Chung, 2013; McGregor et al., 2019) observed a spaced relation between the appearance of micropores and radiation-damaged domains (Paper IV; e.g., Fig. 3.3H), where Hay and Dempster (2009) suggested that radiation damage promotes the alteration of the zircon to microporous texture (and to granular texture, as well; e.g., Schmieder et al., 2015).

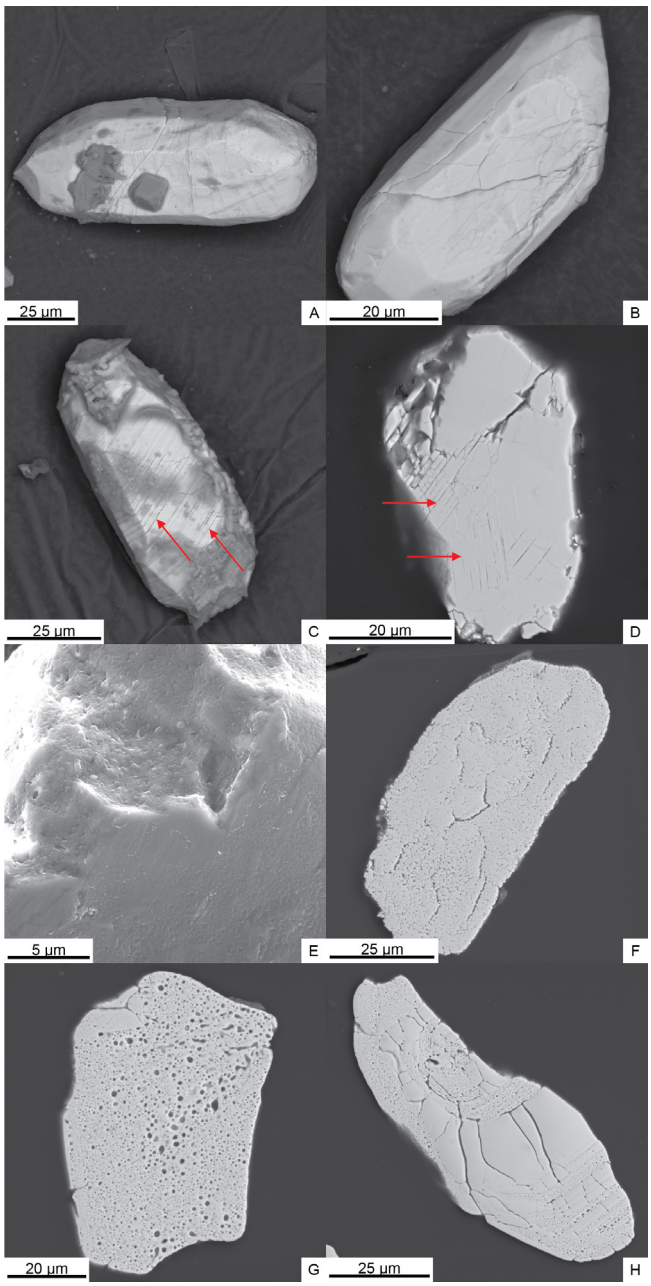

Figure 3.3 Curvi-planar fractures in a zircon grain from the Siljan impact structure, Sweden (photo: author of this thesis, 04/05/2017). B) Irregular fractures in a zircon grain from the Siljan impact structure, Sweden (photo: author of this thesis, 04/05/2017). C) Planar features (red arrows) in a zircon grain from the Siljan impact structure, Sweden (photo: author of this thesis, 04/05/2017). D) Two intersecting sets of planar features (red arrows) in a polished zircon grain from the Siljan impact structure, Sweden (photo: author of this thesis, 19/07/2017). E) Close-up of a granular zircon from the Siljan impact structure, Sweden (photo: author of this thesis, 10/05/2017). F) Polished granular zircon from an impact melt of the Mien impact structure, Sweden (photo: author of this thesis, 07/07/2019). G) Polished zircon grain from an impact melt of the Mien impact structure, Sweden, showing a complete porous texture (photo: author of this thesis, 07/07/2019). H) Polished zircon from an impact melt of the Mien impact structure, Sweden, which is partly porous-textured. Pores occur along oscillating zones along the rim and within the core of the grain that might represent metamict domains (photo: author of this thesis, 07/07/2019). (All images are BSE images with one In-Beam BSE for grain E).

3.2 Shock features in biotite and amphibole

In contrast to framework silicates with an open crystal structure and, thus high compressibility, the closely packed crystal structure of sheet and chain silicates, as for biotite and amphibole, respectively, is less compressible during the shock wave passage (Chao, 1968; Stöffler, 1971, 1972). In consequence, biotite and amphibole are highly resistant to shock pressure and distinctive shock features occur over a wide pressure range (Chao, 1968; Stöffler, 1972). The major physical changes are generated at shock pressures above 40 GPa, where, in comparison, quartz is already highly shocked as observed in phase transitions, e.g., into the high-pressure phase coesite or diaplectic glass (Chao, 1968; Stöffler, 1972). The most

characteristic shock feature in biotite are kink bands (Paper II; Fig. 3.2C) accompanied with a reduced birefringence and pleochroism (Chao, 1967, 1968; Stöffler, 1972). They are generated over a shock pressure range between 1 and 45 GPa, due to a crystal lattice gliding along the base (0001) accompanied with a rotation of the lattice (Chao, 1968; Stöffler, 1972). However, kink bands are also a product of tectonic deformation. Planar features are less common in biotite (Chao, 1968).
The major shock effect in chain silicates such as amphibole is polysynthetic mechanical twinning, a set of closely-spaced, parallel bands with a width of about 10 μm (Paper II; Stöffler, 1972). In amphibole, they are orientated parallel or subparallel to (001) and less to (100) (Stöffler, 1972). As with kink bands in biotite, twinning appears over a large range with pressures between 5 and 45 GPa (Stöffler, 1972). Planar features, sets of closely-spaced, parallel lamella, and mosaicism with a reduced birefringence are generated at shock pressures above 30-40 GPa (Chao, 1967, 1968; Stöffler, 1972).
Both biotite and amphibole are temperature-sensitive, which means they undergo a thermal decomposition rather than melting when exposed to high post-shock temperatures and shock pressures above 45-50 GPa (Chao, 1967, 1968; Stöffler, 1972; Sazonova et al., 2007). At temperatures of ~600°C and ~640°C, respectively, biotite and amphibole oxides, accompanied by a decrease of their birefringence and ploechroism until they become opaque (Chao, 1968; Stöffler, 1972). Their thermal decomposition into magnetite and an amorphous or glassy phase starts at about 1000°C (Chao, 1967, 1968; Stöffler, 1972; Sazonova et al., 2007). However, natural observations of shock metamorphosed rocks from the Jänisjärvi crater, Russia, by Fel'dman et al. (2006b) showed that the mineral chemistry of biotite is already modified at shock pressure between 13 and 16 GPa and above 20 GPa with increasing shock pressure K, Fe and Mg migrate out of biotite where in return significant amounts of Na, Ca and Si are incorporated. Finally, biotite breaks down to a mixture of ilmenite, orthopyroxene and sanidine (Fel'dman et al., 2006a and b). Shock experiments, between 20 and 200 GPa, on the same sample material reveal a biotite decomposition to ringwoodite and spinel at 25 GPa (Fel'dman et al., 2006a).
Amphibole shows a migration of elements, as well, but at higher shock pressures than biotite (26-52 GPa), where an increase of certain element concentrations, e.g., in K, Ti and F, promotes a greater thermal stability of amphibole whereas a higher Fe content has the opposite effect (Sazonova et al., 2007).

3.3 Impactites

Rocks affected by shock metamorphism are called impactites, ranging from completely molten (impact melts, such in Paper III and V; Fig. 3.4A and B) to fractured target material (Fig. 3.4C and D; Osinski and Pierazzo, 2013). Depending on how far the material has been transported from its original pre-impact position during the event, impactites are grouped into autochthonous (at place), parautochthonous (short transportation) and allochthonous (long transportation) (Osinski and Pierazzo, 2013).
Autochthonous and parautochthonous impactites occur immediate to an impact structure as in the rim, beyond the crater and in the crater floor (Osinski and Pierazzo, 2013) (Fig. 2.1A and B). The autochthonous might have been experienced some uplift during the crater formation process, but still kept its original position and stratigraphic relation. Even though the autochthonous shows impact-related fracturing, it reveals rarely shock features (Osinski and Pierazzo, 2013). In large, complex impact structures, the parautochthonous form the uplifted central part of a crater (Fig. 2.1B), where originally deep-seated rocks were moved upwards and are now exposed at the surface. The uplifted material exhibits shock effects that record shock pressures up to 25 GPa (Osinski and Pierazzo, 2013, and references therein). Parautochthonous material is also deposited in the annular trough which surrounds the uplifted central part of a complex impact structure (Fig. 2.1B; Osinski and Pierazzo, 2013).
Allochthonous impactites occur both proximal and distal to an impact structure (Fig. 2.1A and B). Proximal material is comprised of impact breccias and impact melt rocks forming the crater filling (Fig. 2.1A and B; Osinski and Pierazzo, 2013, and references therein). Impact breccias are subdivided into lithic and melt-bearing breccia, both consisting of lithic clasts of the target rock, clasts of non-shocked and shocked minerals embedded in a fine-grained matrix, where the melt-bearing breccia hosts melt clasts (Fig. 3.5A-C), as well. Distal build impact breccias the majority of the ejecta blanket, deposited outside of a crater (Fig. 2.1A and B) often with inverted stratigraphy (Osinski and Pierazzo, 2013). The lower part of the ejecta blanket is made of lithic breccias which only preserve a low level of shock. The material stems from the near-surface levels of the target. The lithic breccias are overlain by melt-bearing breccias, hosting high shocked material which comes from deeper sources in the target (Osinski and Pierazzo, 2013). Due to strong erosion, ejecta blankets are described only for a few impact structures, e.g., Nördlinger Ries impact structure, Germany, where the Bunte breccia (lithic breccia) is sharply overlain by the Suevite (melt-bearing breccia) (Fig.3.5D and F; Osinski and Pierazzo, 2013, and references therein).
Impact melts, as used in Paper III and V (Fig. 3.4A and

B), are a characteristic product of a hypervelocity impact event. They are whole-rock melts consisting of a melted matrix mixed with target material including shocked and non-shocked minerals and lithic clasts (Osinski and Pierazzo, 2013, and references therein). Depending on the amount of clasts, it can be distinguished between clast-rich (e.g., Fig. 3.4A), clast-poor and clast-free impact melts, where the clasts show thermal reactions with the melt matrix. Regarding the appearance of the melt matrix, it can be described as glassy (e.g., Fig. 3.4B), devitrified or fine, medium or coarse-crystalline (Osinski and Pierazzo, 2013). Impact melts are formed due to the immediate impact-generated melting of the target rock by decompression from high shock pressures and temperatures between 1500 and 2500°C, that subsequently cools down relative rapidly (Osinski and Pierazzo, 2013, and references therein). In large, complex impact structures, the bulk of impact melts form a meter-thick melt sheet at the crater floor above the parautochthonous, which can extent laterally several kilometres (Osinski and Pierazzo, 2013, and references therein). Impact breccias can flank the melt sheet from above and below, forming a thin layer between the parautochthonous and the melt material (Osinski and Pierazzo, 2013). Impact melts also occur as centimeter to meter-sized dikes intruding the parautochthonous of the crater floor or form melt lenses and/or glassy particles in impact breccias, too (Osinski and Pierazzo, 2013).

Melted material in kind of millimeter to centimeter-sized spherules and tektites/microtektites (Fig. 3.6A and B) is formed in the very early stage of the crater formation process (Osinski and Pierazzo, 2013). In the proximity of a crater, they are a part of the ejecta blanket and distally deposited in strewn fields several hundred to thousand kilometres away from the crater, e.g., the North American strewn field of the Chicxulub impact structure, Mexico (Koeberl, 1993; Osinski and Pierazzo, 2013, and references therein). Another type of impact-generated melt is pseudotachylite, which was first described by Shand (1916) from the Vredefort impact structure, South Africa (Fig. 3.6C; Osinski and Pierazzo, 2013). The matrix of pseudotachylite is generally dark and aphanitic, surrounding lithic clasts, minerals and fragments of the target rock (Fig. 3.6C). As irregular injections, pseudotachylites are pervasively in the parautochthonous, especially in the uplifted central part of a crater, where they form dikes, veins and anastomosing bodies. But they occur in impact-generated faults and contacts between different lithologies, as well (Osinski and Pierazzo, 2013, and references therein). Pseudotachylites can also be a product of endogenic tectonic processes (Fig. 3.6D), thus they are not unique for impact events. However, whether impact or endogenic-related, both include frictional melting and cataclasis as the presumable main formation processes for pseudotachylite (Osinski and Pierazzo, 2013, and references therein).

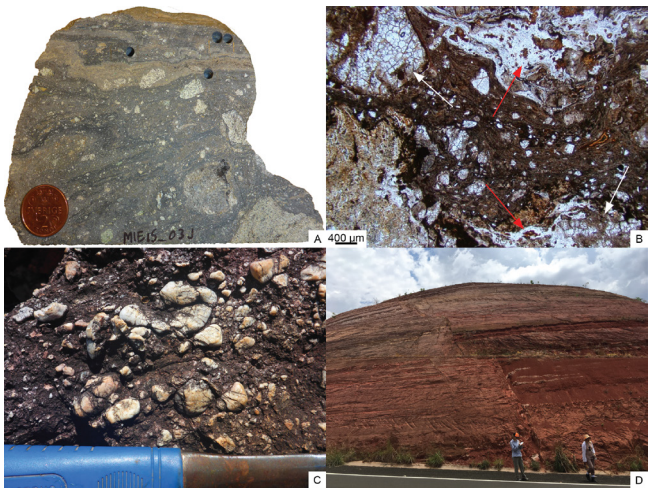

Figure 3.4 A) Clast-rich impact melt from the Mien impact structure, Sweden, showing a brownish to dark grey melt matrix floating around lithic clasts (used in Paper III). The size of the coin is 2 cm (photo: author of this thesis). B) Plane-polarized image of a Mien impact melt sample. The dark brown melt matrix floats around strong altered clasts (lower left corner) and clasts of minerals. The white arrows show ballen quartz, indicative for shock metamorphism. The red arrows show so-called schlieren quartz. C) Shocked and fractured pebbles of a deformed conglomerate of the Alto Garças Formation (Rio Ivaí Group), Araguainha impact structure, Mato Grosss and Goiás, Brazil. The size of this part of the hammer is ~10 cm (photo: author of this thesis, 06/10/2019). D) Brittle deformed sandstone showing normal faulting caused by impact event. Aquidauana Formation at the southwestern boundary of the Araguainha impact structure, Mato Grosss and Goiás, Brazil (photo: unknown, 05/10/2019).

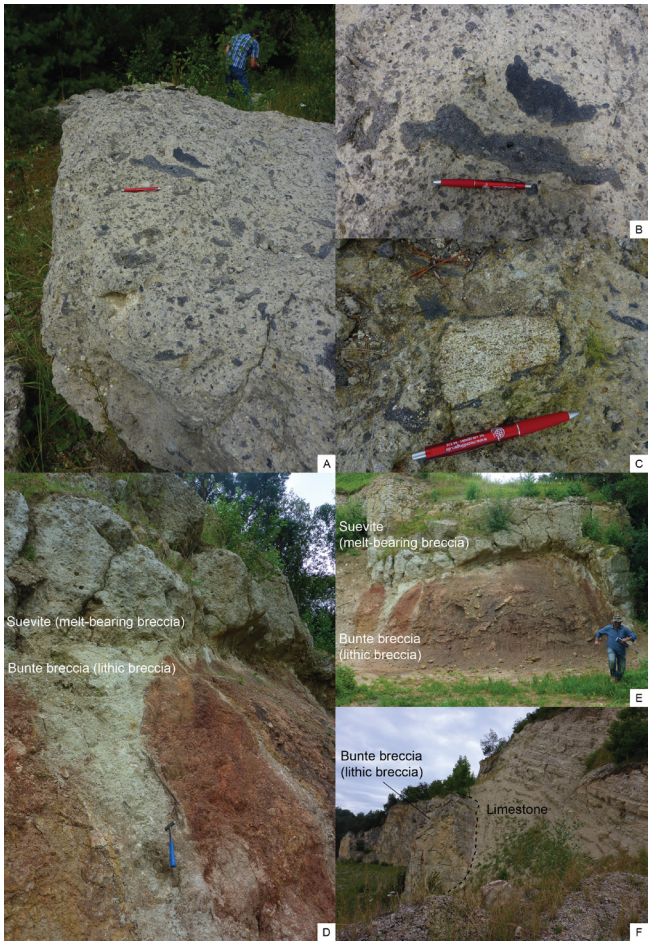

Figure 3.5 A) A boulder of suevite, a specific term solely used for the melt-bearing impact breccia from the Nördlinger Ries impact structure, Germany (photo: author of this thesis, 03/08/2016). B) Close-up of A showing irregular-shaped, dark grey melt clasts (Flädle) surrounded by a light grey, fine-grained matrix (photo: author of this thesis, 03/08/2016). C) Suevite showing a lithic clast of the target rock surrounded by irregular-shaped, dark grey melt clasts and a light grey, fine-grained matrix (photo: author of this thesis, 03/08/2016). The size of the pen in A-C is 14 cm. D and E) Sharp contact between lower Bunte breccia (lithic breccia) and overlying suevite (melt-bearing breccia) in the suevite quarry Aumühle, Nördlinger Ries impact structure, Germany. Size of the hammer is 31 cm (photo: author of this thesis, 04/08/2016). F) Bunte breccia in contact with limestone, marked by the black, dotted line. The limestone shows tilted bedding. In general, the limestone of a quarry in Wemding, eastern rim of the Nördlinger Ries impact structure, Germany, is deformed and inclined to variable degrees due to the impact event (photo: author of this thesis, 04/08/2016).

Figure 3.6 A) Altered spherules from the Cretaceous-Paleogene boundary in Haiti (12/03/2020: https://www.e-education.psu.edu/earth501/content/p3_p5.html). B) Tektites in variable shapes (12/03/2020: http://www.tektites.co.uk/). C) Pseudotachylite from the Vredefort impact structure, South Africa (13/03/2020: https://skyfallmeteorites.com/glossary/pseudotachylite#sf-2/0/impact-breccia-pseudotachylite-Vredefort.jpg). D) Pseudotachylite formed by tectonic processes from the Outer Hebrides, Scotland (13/03/2020: http://tectonicstudiesgroup.org/outer-hebrides-fieldtrip-2015/).

4. Geochronology

In order to get a better understanding on how the Earth has evolved since its formation, the temporal control of geological processes is crucial. Thus, the geochronology, dealing with the age determination of terrestrial and extraterrestrial material, have grown to an important scientific field over the last decades. Since the discovery of the radioactivity by Henri Becquerel in 1896 (Press and Siever, 2003; Faure and Mensing, 2005) and the decay of highly radioactive elements by Ernest Rutherford and Frederick Soddy in 1902 (Press and Siever, 2003; Faure and Mensing, 2005), absolute ages have been possible to established through various radiometric dating methods. First attempts to determine radiometric dates were done by Ernest Rutherford and Bertram Borden Boltwood in 1905 and 1907, respectively, and subsequently by Arthur Holmes in 1911 (Badash, 1968). In 1927, Arthur Holmes published his '*The Age of the Earth, an Introduction to Geological Ideas*', where he estimated the age of the Earth between 3.0 and 1.6 Ga based on the uranium and lead content of the Earth's crust.

Radiometric dating uses the decay of unstable, radioactive parent isotopes to stable, radiogenic daughter isotopes, which is assumed to proceed under a constant rate. Today exists a great variety of radio-isotope chronometers based on different radioactive decay systems. This thesis is focused on the U-Pb (Paper I and IV) and K-Ar decay systems (Paper II, III and V). Due to their long half-lifes (10^9 yr), both decay systems enable the dating of terrestrial and extraterrestrial material with ages of up to billions of years. For instance, Patterson (1956) used the U-Pb decay system of meteorites to determine the age of the Earth to about 4.55 Ga. The K-Ar decay system can yield accurate and precise ages to date quaternary volcanic eruptions (e.g., Hearty et al., 2005).

In order to the radiometric age is geologically significant it is assumed that rocks or minerals became a closed isotopic system nearly at the same time and remained closed until today, i.e., both parent and daughter isotopes are neither gained nor lost except from the radioactive decay (Fig. 4A and B). Further, the decay constant is stable over geological times (Faure and Mensing, 2005). In a closed isotopic system, radiogenic daughter isotopes are accumulated and increase over time, whereas the number of parent isotopes decreases (Fig. 4B and C). Presuming the decay rate of a certain parent isotope is known, the age can be calculated from the ratio between daughter and the parent isotopes of the system. Following the law of radioactivity by Rutherford and Soddy from1903:

$$- (dNdt^{-}) = \lambda N$$

stating that the decay rate (λN) of the parent isotopes (N) are proportional to the number of isotopes that remain in the system at any time (t) (Faure and Mensing, 2005). Due to conversion, the basic age equation is:

$$D = D_0 + N (e^{\lambda t} - 1)$$

with D equals the number of radiogenic daughter isotopes, D_0 is the number of initial daughter isotopes, N is the number of radioactive parent isotopes, λ is the decay constant and t depicts the time (Faure and Mensing, 2005). Important to consider is that the resulting radiometric date is actually addressed as an age of the rock or mineral, which reflects the time that elapsed since the system became closed and started to accumulate daughter isotopes (Fig. 4D). In this thesis age determination of impact structures is used to clarify the timing of impact

events. Such events can decompose minerals and even melt entire rocks in such a way that a portion of daughter isotopes are lost from an isotopic system which restart the isotopic clock (Paper III). The recrystallisation of molten rocks with newly grown mineral phases even generates new isotopic clocks corresponding to an impact event (Paper IV and V). However, even though impact events have a devastating effect, in some cases isotopic systems are not affected. Thus, a further focus of the thesis lies on syn and post-impact processes that influenced isotopic systems unrelated to an impact event (Paper I and II).

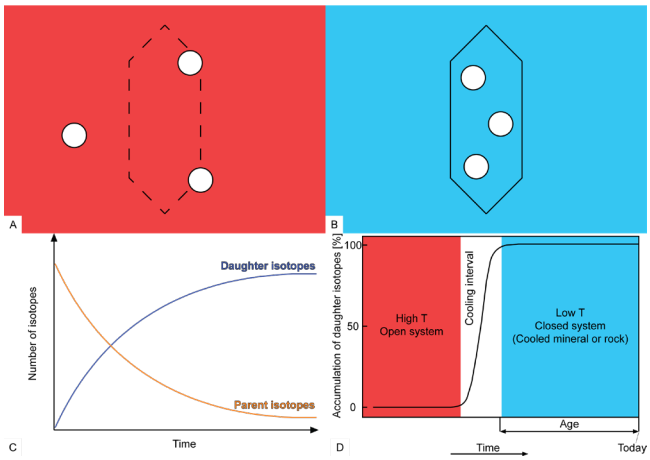

Figure 4 A) Open system (mineral/rock = dashed line) at high temperature. Radiogenic daughter isotopes (white) are highly diffusive and is lost from the system as soon as they are formed due to the radioactive decay of an unstable parent isotope. B) Closed system (cooled mineral/rock = solid line) at low temperatures. The diffusivity of the daughter isotope is ceased and they are trapped within the system. As consequence they will be accumulated as illustrated in C) Plot increase of number of daughter isotopes and decrease of number of parent isotopes vs time, in a closed isotopic system. D) Plot accumulation of daughter isotopes vs time (modified according to McDougall and Harrison, 1999). When the system cools down, it eventually passes through the closure temperature (see chapter 5.2), from which the daughter isotopes become immobile and start to accumulate in the system. The time since the system was closed represents the age of the sample. In a closed system, due to the radioactive decay, the number of daughter isotopes increase, while the number of parent isotopes decreases, as shown in C.

5. U-Pb chronometer

5.1 Overview

The radioactive decay of U to Pb (Fig. 5.1) builds the basis for the most widely used dating method which is capable to date events from the time the solar system was formed about 4.57 Ga ago, until more recent times (Schoene, 2014). The first published U-Pb age by Bertram Boltwood in 1907 was determined on thorinite, a U-rich mineral taken from rocks along the southern coast of Sri Lanka (Badash, 1968; Hölzl et al., 1994). Uranium occurs in significant amounts in accessory minerals, such as zircon, titanite, monazite, apatite, baddeleyite, xenotime and rutile. In this thesis, zircon (Paper I and IV) is investigated. Among all U-bearing accessories, zircon is the most widespread mineral. Its relative resistivity to alteration and incorporation of U, while excluding Pb, making it suitable for U-Pb dating. Uranium, belonging to the high field strength elements, has a high ionic charge and thus, is incompatible during the magma differentiation. It becomes enriched in the liquid phase as the crystallisation proceeds and finally incorporated in higher concentrations in accessory phases such as zircon (U = 100-6000 ppm and Pb = 10-10000 ppm; Stosch, 1999). Under non-oxidizing conditions, both U and Pb have a tetravalent oxidation state and similar ionic radii (U^{4+} = 1.05 Å; Faure and Mensing, 2005, and Pb^{4+} = 0.94 Å; Lee et al., 1997), which makes both elements immobile. However, once Pb is reduced to its divalent oxidation state, which coincides with an increase of the ionic radius (Pb^{2+} = 1.29 Å; Lee et al., 1997), Pb becomes incompatible and thus, is discriminated from zircon. Therefore, all Pb in a zircon is typically radiogenic in origin with no or very low concentrations of initial Pb.

Uranium consists of essentially two natural isotopes ^{235}U and ^{238}U, both of them being radioactive. The long half-lifes of ^{238}U ($T_{1/2}$ = 4.468x10^9 yr) and ^{235}U ($T_{1/2}$ = 0.704x10^9 yr) enable the dating of very old material (Faure and Mensing, 2005; Schoene, 2014). Both ^{238}U and ^{235}U decay through two independent chains to ^{206}Pb and ^{207}Pb, respectively (Fig. 5.1; Faure and Mensing, 2005). It allows for an internal test whether the system remained closed over geological times, where the dates of the $^{238}U/^{206}Pb$ and $^{235}U/^{207}Pb$ ratios should agree. A third isotopic ratio, namely the $^{207}Pb/^{206}Pb$, can be used to calculate an age providing the $^{238}U/^{235}U$ is known. The main isotopes of Pb are ^{204}Pb, ^{206}Pb, ^{207}Pb and ^{208}Pb. Except for ^{204}Pb, all isotopes are radiogenic. ^{208}Pb is formed through the decay of ^{232}Th.

5.2 Closure temperature concept

From fully open to fully closed-system behaviour, an isotopic system passes a cooling interval, which Dodson (1973) defined as closure temperature (Fig. 4D). Within this temperature range radiogenic daughter isotopes, highly diffusive and leaving the system (mineral/rock) as soon as they are formed at high temperatures, become continuously immobile until their diffusion is negligible and they are trapped in the mineral or rock when the system becoming closed. The additional incorporation of parent isotopes into the system is stopped, as well. Accor-

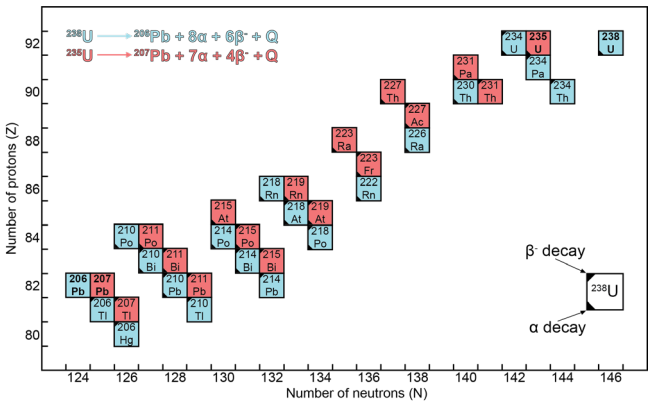

Figure 5.1 The two decay chains of U with their shorthand-written description in the upper left corner. Legend in the lower right corner indicates the β^- and α decays.

ding to Dodson (1973), the temperature of a system at a certain time corresponds to its apparent age. Cessation of daughter isotope diffusion does not necessarily occur with the crystallisation of a mineral or rock and they can still be mobile far below the crystallisation temperature. Thus, the T_C differs between the chronometers and in comparison, the U-Pb system in zircon has one of the highest T_C >900°C (Lee et al., 1997; Cherniak and Watson, 2000), which allows for the determination of crystallisation ages.

5.3 Methdology

In general, the ratios between remaining parent isotopes and new-formed daughter isotopes of a closed system are determined by mass spectrometry. The first instruments, mass spectrographs, were built in the early 20th century by J. J. Thomson, F. W. Aston, and A. J. Dempster, who discovered the natural isotopes for the majority of the elements of the periodic table (Faure and Mensing, 2005). The mass spectrometry separates isotopes based on their masse-to-charge ratio. A mass spectrometer is build up by three main components: 1) ion source, 2) mass analyzer (e.g., quadrupole or magnetic sector), and 3) detector system. After the ionization in the ion source, the isotopes are separated through a magnetic or electric field according to their mass-to-charge ratios following the equation (McDougall and Harrison, 1999; Faure and Mensing, 2005):

$$r^2 = (m2V)(eB2)^-$$

with r equals the radius of ion beam trajectory, m is the ion mass, V is the kinetic energy of the ion, e is the ion charge, and B is the strength of the magnetic or electric field. In summary, it means low-mass ions are more deflected than high-mass ions.
Since several masses have to be measured, due to variations in the magnetic or electric field or in the acceleration voltage, the ion beam can be steered into the detectors in a way that it switches between different masses (mono-collection mode by peak-hopping) without moving the detector (Faure and Mensing, 2005). Multiple collector arrangements enable the simultaneous acquisition of the masses without a beam switch (static mode). When an ion strikes a detector, a difference in the voltage is recorded whose signal appears as a peak. A series of peaks build a mass spectrum of an element where each peak is characterized by a certain mass-to-charge ratio which is assigned to a certain isotope (Faure and Mensing, 2005).

5.3.1 Sample preparation

All zircon preparation was carried out at the Department of Geology at Lund University. In a first step, a rock sample was hand-crushed using a hammer until a powder was formed (Fig. 5.2A). Subsequently, the rock powder was separated in to different size fractions by a sieve stack. In this thesis, the final size fraction is 80-250 µm from which the zircon grains are separated (Fig. 5.2B). The zircon separation is done by a water-based density separation (Wifley Table) (Fig. 5.2C), followed by hand-picking under the optical microscope with 100-200 grains per sample (Fig. 5.2D). The separated grains are fixed on a tape and mounted in epoxy resin (Fig. 5.2E). A cylindrical-shaped ring is used to get the disc-like shape of the epoxy mount. Finally, the hardened epoxy mount is polished using diamond pastes with different grinding sizes from 9 µm to 0.25 µm. The polishing is finished when the interior of each zircon grain is exposed at the epoxy surface (Fig. 5.2F). Zircon grains analysed by EBSD are eventually polished with a silica colloidal suspension.

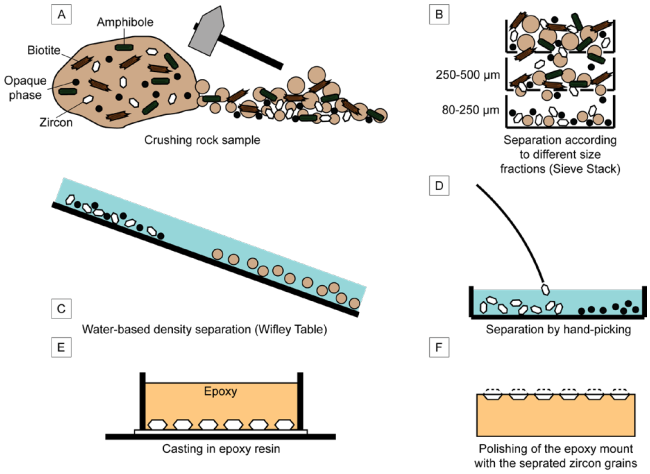

Figure 5.2 Schematic illustration of the sample preparation.

5.3.2 FE-SEM analyses

The complex crystallisation history of many zircon grains, often with different growth textures associated with variable U-Pb chemistry, makes it necessary to conduct analyses by SEM prior to the U-Pb analyses in order to have control on the internal grain texture and thus, being able

to target suitable sites for the U-Pb dating. In particular, in this thesis analyses of shock features such as planar features and neoblasts (Fig. 3.3C-F; see chapter 3.1) are of great interest for the interpretation of recorded dates. All FE-SEM analyses is carried out at the Department of Geology at Lund University using a Tescan Mira3 High Resolution Schottky FE-SEM (*Fig. Box 5.1.1A*). The SEM technique uses an electron beam to enlarge features on µm to nm-scale. It provides near-surface information by scanning the sample with an electron beam where a variety of signals are generated that either produce an image or yield compositional data (Ul-Hamid, 2018). Analyses by EBSD give information about the crystallography of a mineral phase. It enables the determination of crystal structures, orientations, grain sizes and boundaries as well as identifying phases (Ul-Hamid, 2018). As the entire instrumentation is under vacuum, the sample material has to be coated, e.g., with carbon, to make it conductive. The FE-SEM instrumentation at the at the Department of Geology at Lund University, however can also work in low vacuum mode (7-500 Pa), where no coating is needed.

5.3.2.1 Imaging

Signals that are used in this thesis (see Paper I and IV) are SE, BSE, and CL. SE and BSE are inelastic and elastic deflected electrons (*Fig. Box 5.1.2A*), respectively, with different kinetic energies (Ul-Hamid, 2018). They come from different depth within a specimen (*Fig. Box 5.1.2B*), carrying different information. The low kinetic energy SE are from a shallower depth (~100 nm) and thus, image the topography of a specimen (Ul-Hamid, 2018). Therefore, surface features such as planar features in zircon are clearly visible in SE images (*Fig. Box 5.1.2C*). Whilst BSE, coming from about 1 µm below the specimen surface, give information about compositional contrasts (Ul-Hamid, 2018), e.g., ZrO_2 inclusions occur as bright spots within a zircon grain (*Fig. Box 5.1.2D*). In contrast, CL signals are emitted light of specimen atoms when they return from their excited (caused by high-energy beam electrons) to the ground state. They stem from about 1-5 µm depth and yield information about the internal texture and element distribution (Ul-Hamid, 2018). For instance, different growth zones in a zircon with variable U and Pb incorporation become visible in different grey scales (*Fig. Box 5.1.2E*). Further signals such as characteristic X-rays for chemical composition, continuum X-ray (Bremsstrahlung) or Auger electrons are not recorded in this thesis. For more details, see *Box 5.1*.

5.3.2.2 EBSD analyses

The primary electron beam strikes the surface of the sample, which is tilted about 70° from horizontal (*Fig. Box 5.1.3A and B*). As the primary beam penetrates only few tens of nanometers, EBSD is a surface-sensitive method (Ul-Hamid, 2018). Thus, the surface of the sample has to be well polished. Resulting backscattered electron diffractions at atomic planes, that are arranged periodically and form the crystal lattice, are visualized as straight lines (*Fig. Box 5.1.3B*). As these atomic planes are orientated in different directions, various straight lines are produced, intersecting each other and form a network, the so-called Kikuchi pattern (*Fig. Box 5.1.3B*; Ul-Hamid, 2018). An EBSD detector equipped with a phosphor screen and a CCD camera image the Kikuchi pattern (Fig. Box 5.1.3B and C). It is indexed by a computer software and provides information about crystal structure and orientation. For more details, see *Box 5.1*.
In Paper IV, EBSD analyses are performed in order to identify the former presence of reidite by the scanning of granular or neoblastic zircon, which still preserves its crystallography. This specific textural zircon, called FRIGN zircon, are highly promising to yield reliable impact-related ages.

5.3.3 U-Pb analyses

There are three standard ways for the U-Pb dating of a sample. The first is called ID-TIMS analyses and implies chemical dissolution of a number of zircon grains (or parts of a single grain) by dissolving them in hydrofluoric and nitric acid. In order to calculate the amounts of U and Pb isotopes, a prerequisite for obtaining accurate $^{206}Pb/^{238}U$ and $^{207}Pb/^{235}U$ ages, a small amount of an isotopic tracer (e.g., $^{205}Pb/^{235}U$) is added to the sample before dissolution. After some chemical steps in the clean lab the sample is eventually loaded onto a Re-filament and put into the ion source of the mass spectrometer. Due to gradual heating of the filament under vacuum, the U and Pb isotopes are ionized at different filament temperatures and measured in dynamic (peak-hopping) or static mode.
SIMS and LA-ICP-MS, both are in-situ techniques, enable spatial analyses of a zircon grain (Schaltegger et al., 2015). Both techniques use a beam to ablate a small amount of material which is subsequently analysed by a mass spectrometer. SIMS typically operates with a spot size of 2-30 µm (Schaltegger et al, 2015) and a penetration depth of less than 4 µm (Schoene, 2014). It applies a higher spatial resolution, which requires less sample volume and is thus less destructive than LA-ICP-MS, which typically invokes a spots size of 25-35 µm and a penetration depth of 15-40 µm (Schaltegger et al., 2015).
Both LA-ICP-MS (see Paper I) and SIMS (see Paper IV) were performed during the course of this PhD project. The LA-ICP-MS analyses are carried out at the Department of Geology at Lund University, equipped with a Bruker Aurora Elite ICP-MS (*Fig. Box 5.2.1A*). LA-ICP-MS uses a laser beam to ablate material from a zircon grain which is transported as aerosol by a constant flow of a carrier gas to the ICP-MS system. A plasma, formed

Box 5.1 Field Emission-Scanning Electron Microscope

A SEM instrument consists of an electron column and a sample chamber, which is controlled by a computer system (*Fig. Box 5.1.1A* and *B*; Ul-Hamid, 2018).

5.1.1 Electron column

A field emission electron gun, equipped with a high brightness Schottky emitter at the top of the electron column, generates the electron beam (A, *Fig. Box 5.1.1B*). It consists of a tungsten cathode with a sharpened tip (Ul-Hamid, 2018). The electron gun is supplied by a high voltage of 30-40 kV (B, *Fig. Box 5.1.1B*; Ul-Hamid, 2018). A negative potential (3-5 kV) at the tip of the cathode generates a highly concentrated electric field (10^3 V/μm). It reduces the potential barrier so that the electrons can be emitted from the cathode tip without increasing their kinetic energy (tunneling effect) (Ul-Hamid, 2018). Subsequently, due to a potential difference, the electrons, forming a beam, are accelerated (acceleration voltage = 50 V to 30 kV) towards the sample chamber at the lower end of the electron column (C, *Fig. Box 5.1.1B*). Electronic optics such as electromagnetic lenses (condenser and objective lenses), apertures, stigmators and scanning coils, shapes and corrects the electron beam for lens aberrations, such as astigmatism, during its passage through the electron column and finally focus a fine beam on the sample (D, *Fig. Box 5.1.1B*; Ul-Hamid, 2018). A vacuum pump system, evacuating the entire FE-SEM instrumentation (E, *Fig. Box 5.1.1B*), enables a free pathway for the electrons to the sample chamber without colliding with air molecules and thus, getting eventually scattered. At the Department of Geology at Lund University, depending on the demands of the analysis, it can be worked in high (<$9x10^3$ Pa) and low vacuum (7-500 Pa) mode. Working in the high vacuum mode, samples have to be coated with carbon to make them conductive.

5.1.2 Sample chamber

The sample chamber (F, *Fig. Box 5.1.1B*) is equipped with a motorized sample stage, an infra-red camera and several detectors, including BSE, SE and CL. For the sample loading, the entire chamber can be opened, where the sample, fixed on a sample holder, is placed on the motorized stage. It can move laterally in x and y as well as towards the column optic axis in z direction, which changes the working distance between the sample and the electronic optics. The entire stage can rotate 360°. The movement can be controlled manually or automatically by default in the x, y, and z.

The infra-red camera provides a live image from inside the sample chamber which enables a monitoring of the sample stage and holder in real time. When some detectors are used such as for BSE and CL imaging, the camera has to be switched off due to their sensitivity to IR rays. The different detectors collect the signals, coming from the sample, and convert them into electrical pulses, which are shown either as an image or as an elemental spectrum.
The signals, leaving the samples, are elastic and inelastic deflected electrons from the incoming beam, which interacts with the near-surface atoms of the specimen (Ul-Hamid, 2018). Elastically scattered beam electrons, deflected in an angle larger than 90° and without loss of their kinetic energy, are backscattered out of the specimen and thus, detected as BSE signal (*Fig. Box 5.1.2A*; Ul-Hamid, 2018). Due to their high deflection angle, the BSE detector should be located right above the specimen (G, *Fig. Box 5.1.1B*). The Department of Geology at Lund University uses a retractable BSE and an In-beam BSE detector. In contrast, inelastic scattered beam electrons with a low deflection angle kick out weakly bonded electrons from the outer shells of the specimen atomic nucleus and transfer their kinetic energy to these ejected electrons, known as SE (*Fig. Box 5.1.2A*; Ul-Hamid, 2018). The Department of Geology at Lund University uses an Everhart-Thornley detector (H, *Fig. Box 5.1.1B*), consisting of a scintillator-photomultiplier system, and an In-beam SE detector to record the SE signal. The CL signals are detected by a panchromatic motorized retractable CL detector (I, Fig. *Box 5.1.1B*) collecting the emitted light with a wave length between 185 and 850 nm. The FE-SEM instrument at the Department of Geology at Lund University can achieve a maximal imaging resolution of 1.0 nm under 30kV and in high vacuum mode.

5.1.3 EBSD analyses

When the electrons of the primary beam interact with the near-surface atoms of a 70°-tilted sample (Fig. Box 5.1.3A), backscattered electrons are formed that scatter in all directions and become diffracted at atomic planes, which build up the crystal lattice (Ul-Hamid, 2018). A small part of the backscattered electrons is diffracted in such an angle in order to fulfil Bragg's law (Ul-Hamid, 2018):

$$n\lambda = 2d\sin\theta$$

with n is the order of diffraction, λ is the electron wavelength, d is the atomic or lattice plane spacing, and θ is the Bragg angle of diffraction.

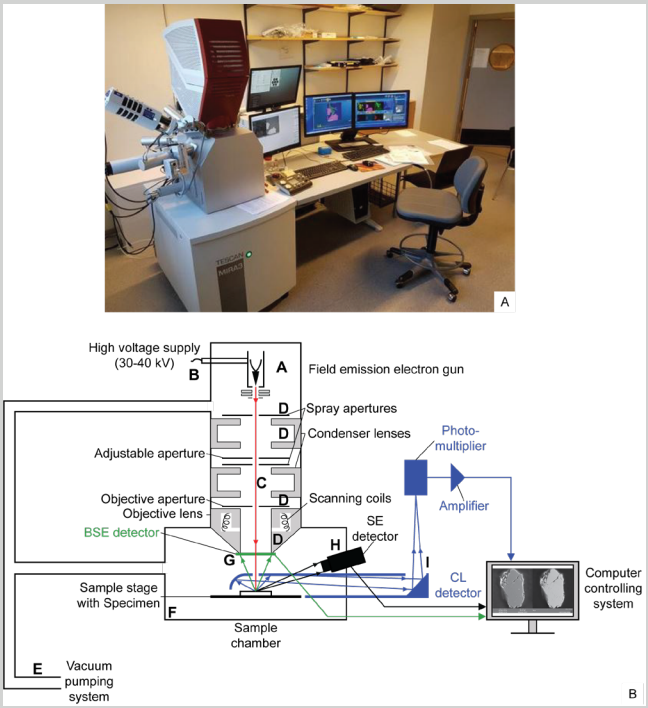

Figure Box 5.1.1 A) Tescan Mira3 High Resolution Schottky FE-SEM at the Department of Geology at Lund University (17/07/2020: https://www.geology.lu.se/research/laboratories-equipment/field-emission-scanning-electron-microscopy-and-edsebsd-analysis-laboratory) B) Schematic illustration of a scanning electron microscope as it is used at the Department of Geology at Lund University (modified according to Ul-Hamid, 2018). The bold letter indicate the steps as described in the text.

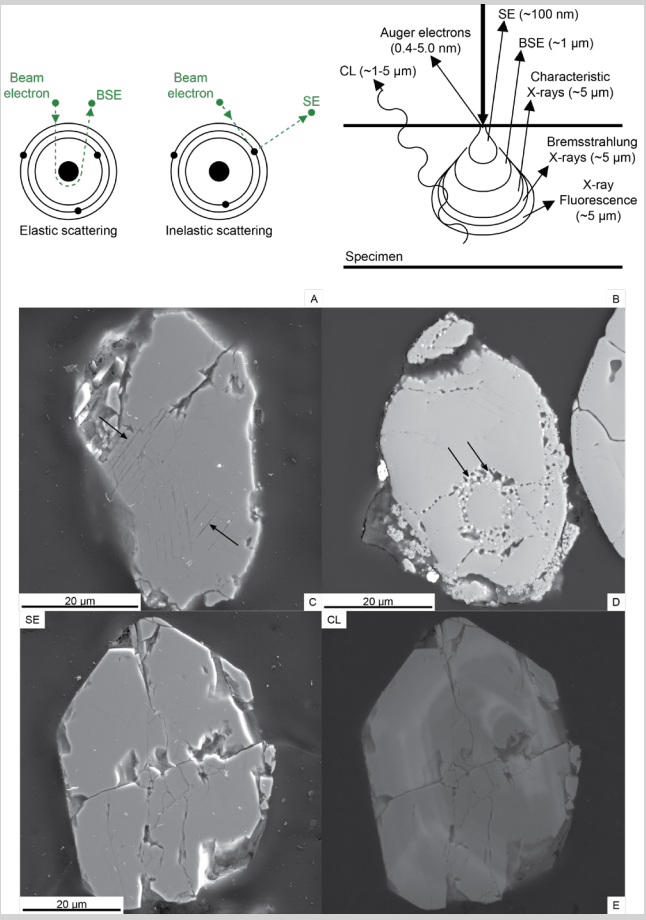

Figure Box 5.1.2 A) High-angle elastic and low-angle inelastic deflection of electrons producing BSE and SE signals, respectively (modified according to Ul-Hamid, 2018). B) Activation volume of the different signals which are generated by the interacting of an incoming electron beam with a specimen. The signals come from different depths of the specimen where SE stem from near the surface and BSE from deeper parts. CL signals come from the deepest levels. The other signals such as characteristic X-rays, Bremsstrahlung X-rays, X-ray fluorescence and auger electrons are not recorded in this thesis (modified according to Ul-Hamid, 2018). C) SE image of a zircon showing planar features (black arrows) as topographic information. Zircon from the Siljan impact structure, Sweden (photo: author of this thesis, 19/07/2017). D) BSE image of a porous zircon from the Mien impact structure, Sweden. Bright inclusions of ZrO_2 (black arrows) are shown as compositional contrast (photo: author of this thesis, 07/07/2019). E) A SE image (left) in comparison to a CL image (right) of a zircon from the Siljan impact structure, Sweden. The CL image reveals an oscillating zoning visible in different grey scale, indicating inhomogenities in the chemical composition, which cannot be observed in the SE image (photo: author of this thesis, 19/07/2017).

These backscattered electrons form a diffracted beam, which leaves the sample cone-like in all directions (*Fig. Box 5.1.3B*; Ul-Hamid, 2018). Each atomic plane produces two conical-shaped diffraction beams, where the first one is coming from the front and the second from the rear of the plane (*Fig. Box 5.1.3B*; Ul-Hamid, 2018). Both, so-called diffraction cones, occur as parallel-paired dark lines with a bright band between them in the Kikuchi pattern, which itself is made up by several of these paired dark lines with different orientations and intersecting each other to form the network of the pattern (*Fig. Box 5.1.3B*; Ul-Hamid, 2018). Each paired dark lines represent one atomic plane in the sample and thus, the Kikuchi pattern reflects the symmetry of the crystal structure of a mineral phase.

The Kikuchi pattern is formed on the phosphor screen of the EBSD detector (*Fig. Box 5.1.3C*), e.g., a NordlysNano from Oxford Instruments as used at the Department of Geology at Lund University. When the diffraction cones cross the phosphor screen, the backscattered electrons are converted into a light signal. It passes a lead glass, sitting after the screen, and reaches the CCD camera of the detector (*Fig. Box 5.1.3C*), where the light is converted into an image, occurring onto the computer monitor (Ul-Hamid, 2018). As only a small part of the backscattered electrons is diffracted in a Bragg angle, the majority of them form the background which masks the signal of the Kikuchi pattern. Therefore, the background has to be collected during an analysis in order to subtract or divide it from the pattern (Ul-Hamid, 2018). Computer software, such as Aztec from Oxford instrumentations as used at the Department of Geology at Lund University, enable the identification of mineral phases using the Kikuchi pattern. The software indexes several points from the pattern and compare them to crystallographic values, e.g., crystallographic indices, stored in the database. The result is a best fit of the investigated mineral, giving the phase and its orientation (Ul-Hamid, 2018). In Paper IV, the

Kikuchi patterns of the sample grains are compared with the reflector list for zircon (Hazen and Finger, 1979; 1 atm), reidite (Farnan et al., 2003) and monoclinic ZrO_2 (baddeleyite; Gualtieri et al., 1996).

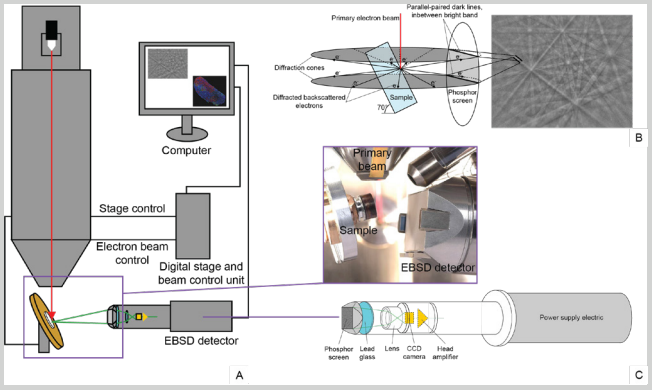

Figure Box 5.1.3 A) Schematic illustration for an EBSD system set up. B) Two diffraction cones build up by backscattered electron diffracted in Bragg angle from an atomic plane. When crossing the phosphor screen of the EBSD detector, both cones are imaged as two parallel-paired dark lines with a bright band between them. Several of these paired dark lines orientated differently and intersecting each other form the Kikuchi pattern, as shown in a small image to the right. It shows the Kikuchi pattern of a zircon (10/07/2020: http://www.ebsd.com/ebsd-applications/ebsd-gallery/diffraction-patterns-from-various-materials). C) The image above shows the arrangement between sample and EBSD detector in the SEM sample chamber (10/07/2020: https://www.birmingham.ac.uk/Documents/college-eps/metallurgy/cem/Intro EBSD63slidesv2.pdf), as it is used at the Department of Geology at Lund University. Image below shows a schematic illustration of an EBSD Nordlys detector as used at the Department of Geology at Lund University.

through inductive coupling of electrons and ions in a magnetic field, ionizes the isotopes of the aerosol, which are subsequently separated and analysed by a quadrupole mass spectrometer (see chapter 5.3) and recorded by respective detectors. For the U-Pb analysis in this thesis, a complete scan over the entire mass range includes ^{202}Hg, ^{204}Pb, ^{206}Pb, ^{207}Pb, ^{208}Pb, ^{232}Th, ^{238}U. ^{202}Hg is analysed in order to correct for the interfering ^{204}Hg which is sitting on the mass like ^{204}Pb which is needed for the correction of common Pb. For more details, see *Box 5.2*.

The SIMS analyses are carried out by a CAMECA IMS 1280 ion microprobe at the Swedish Museum of Natural History in Stockholm (NordSIMS facility) (*Fig. Box 5.3A*). The zircon grains are bombarded with a primary ion beam. Due to sputtering, near-surface material is removed and emits as secondary ions, consisting of atomic ions and molecular ionic compounds (Schoene, 2014), which are subsequently analysed by a magnetic sector mass spectrometer (*Fig. Box 5.3B*). Commonly, Zr, e.g., as Zr_2O, ^{204}Pb, ^{206}Pb, ^{207}Pb, ^{208}Pb, ^{238}U, U oxides (UO, UO_2) and ^{232}Th are detected by SIMS (Ireland and Williams, 2003). Additionally, the CAMECA IMS 1280 ion microprobe is capable of performing ion imaging analyses, which provide element distribution maps (Joo and Liang, 2013). In Paper IV it is used to mapped the distribution of U and Pb within shocked zircon grains. For more details, see *Box 5.3*.

5.3.4 Calibration

All U-Pb analyses are calibrated against a first reference material and additionally a second reference material is used. For the LA-ICP-MS, GJ-1 (608.53 ± 0.37 Ma; Jackson et al., 2004) and 91500 (1062.4 ± 0.8 Ma; Wiedenbeck et al., 1995) are the first and secondary reference material, respectively. Whilst for SIMS, 91500 is the first and Tremora-2 (416.78 ± 0.33 Ma; Black et al., 2004) the second reference material. All are natural zircon. The primary standard provides control on the accuracy, precision and plausibility of the results (Košler, 2008), i.e., whether the measured dates are correct and finally record an age. The secondary reference material, calibrated against the primary, tests for systematic uncertainties in the analyses to see if the method is correct (Schaltegger et al., 2015). The reference material is measured together with the sample under the same analytical conditions. Common are standard-sample bracketing procedures where several unknowns are enclosed by reference material, e.g., for LA-ICP-MS, an analytical sequence starts with 5-6 GJ-1 and subsequently one 91500, followed by a series of unknowns.

5.3.5 Age calculation

Three different ages can be calculated: $^{238}U/^{206}Pb$, $^{235}U/^{207}Pb$ and $^{207}Pb/^{206}Pb$ age. Starting with the basic age equation:

$$D = D_0 + N(e^{\lambda t} - 1)$$

which is converted according to t:

$$t = 1\lambda^{-}[((D-D_0)N^{-}) + 1]$$

Transferred to the U-Pb system, it can be written for the calculation of the $^{238}U/^{206}Pb$ and $^{235}U/^{207}Pb$ ages, under the assumption the initial Pb concentration ($D_0 = 0$ at t = 0) in zircon is negligible (Schoene, 2014):

$$t_{238/206} = 1\lambda_{238}^{-}[(^{206}Pb/^{238}U) + 1]$$
$$t_{235/207} = 1\lambda_{235}^{-}[(^{207}Pb/^{235}U) + 1]$$

By dividing of the two above-mentioned equations for both isotopic system, the equation for the calculation of the $^{207}Pb/^{206}Pb$ ages is yielded, which is solved iteratively (Schoene, 2014):

$$(^{207}Pb/^{206}Pb) = (^{235}U/^{238}U)[(e^{\lambda 235t} -1)/(e^{\lambda 238t} -1)] = (1/137.88)[(e^{\lambda 235t} -1)/(e^{\lambda 238t} -1)]$$

The $^{238}U/^{235}U$ ratio is seen as constant with a value of

Box 5.2 Laser Ablation-Inductively Coupled Plasma-Mass Spectrometry

A LA-ICP-MS system is build up by two main components 1) a laser ablation system with a sample cell, and 2) a mass analyzer with an ICP system (*Fig. Box 5.2.1A*).

5.2.1 Ablation system

The sample material is ablated by a Cetac Analyte G2 excimer laser with a wave length of 193 nm and <4 ns pulse width (A, *Fig. Box 5.2.2*; *Fig. Box 5.2.1B*). The laser conditions are set to 7-8 Hz repetition rate, 5-6 J/cm^2 fluence, 30 sec ablation duration, and 18x18 µm to 20x20 µm spot size. A 9-hole sample holder (each hole = 2.54 cm in diameter; *Fig. Box 5.2.1C*) is used to place the epoxy mount, carrying the zircon grains, along with the reference materials, where each one is set on a separate hole. The sample holder is placed into a two-volume HelEx2 sample cell (*Fig. Box 5.2.1D*), where the ablation procedure takes place (B, *Fig. Box 5.2.2*). A permanent flow of a carrier gas of He (0.8 l/min) mixed with N_2 (6.5 l/min) evacuates the ablated sample material as aerosol and transport it through a 2 mm PFTE tubing (a 'squid' is used to smooth the signal when low ablation rates are necessary) to the plasma torch (C, *Fig. Box 5.2.2*).

5.2.2 Plasma torch (ICP system)

The plasma (T = 6000-10000 K and energy = 0.6-1.6 kW; Bruker Aurora Training Manual, version 5.0, 2011) used to ionize the isotopes of the aerosol is an atmospheric-pressure plasma, formed by a constantly argon gas flow (0.95 l/min) through a torch (D, *Fig. Box 5.2.2*; *Fig. Box 5.2.3A*). The torch, formed of fused silica, consists of three concentric tubes, where the majority of the argon plasma gas is supplied between the intermediate and outer tube (*Fig. Box 5.2.3A*; Bruker Aurora Training Manual, version 5.0, 2011). Induction coils at the outer tube (*Fig. Box 5.2.3A*), fed with a radio-frequency current of 27 MHz and a power of 1300 W, build up a magnetic field where, due to inductive coupling of electrons and ions of the argon gas, the energy is constantly transferred to the plasma and thus, keep it on running. Its ignition is finally triggered by a discharge spark of the argon gas while a radio-frequency current supplies the induction coils (Bruker Aurora Training Manual, version 5.0, 2011).
The aerosol is routed through the centre tube of the torch to the plasma (*Fig. Box 5.2.3A*) where its isotopes become ionized due to the removal of an electron from their outer shells. It leads to a constant positive ion beam consisting of univalent charged ions (D, *Fig. Box 5.2.2*; Bruker Aurora Training Manual, version 5.0, 2011).

5.2.3 Interface

The interface represents the passage to guide the ion beam from the plasma torch with atmospheric pressure (~100000 Pa) to the low pressure and thus, high vacuum of the mass spectrometer (<0.001 Pa) (E, *Fig. Box 5.2.2*; *Fig. Box 5.2.3B* and *C*; Bruker Aurora Training Manual, version 5.0, 2011).
It consists of a sample cone, skimmer cone and small aperture where due to differential pumping the pressure is step-wise decreased in three stages (E, *Fig. Box 5.2.2*; *Fig. Box 5.2.3B*). A rotary pump reduces the pressure of the first stage to about 667 Pa between the sample and the skimmer cone (*Fig. Box 5.2.3B*; Bruker Aurora Training Manual, version 5.0, 2011). The sample cone (Cu/Cr alloy; Bruker Aurora Training Manual, version 5.0, 2011), exposed to the plasma, is water-cooled and thus, dissipates most of the heat. The remaining plasma, entering the evacuated space of the first stage (*Fig. Box 5.2.3B*), expands rapidly leading to quick temperature decrease. The skimmer cone finally separates the atmospheric pressure from the vacuum area. A turbomolecular pump keep the second stage between the skimmer cone and a small aperture under 0.04 Pa (*Fig. Box 5.2.3B*; Bruker Aurora Training Manual, version 5.0, 2011). A small aperture, transmitted by the ion beam, is the passage to the third stage of the differential pumping system, where the mass analyzer is situated (*Fig. Box 5.2.3B* and *C*). The high vacuum is 0.0007 Pa formed by a second turbomolecular pump (*Fig. Box 5.2.3B*; Bruker Aurora Training Manual, version 5.0, 2011).
Extraction lenses behind the skimmer cone capture the ions and focus them to the ion mirror. The ion mirror, consisting of four electrodes (*Fig. Box 5.2.3C*), build an electrostatic field and deflect and focus the ions as beam towards the small aperture, the entrance of the mass analyzer (F, *Fig. Box 5.2.2*; Bruker Aurora Training Manual, version 5.0, 2011).

5.2.4 Quadrupole mass analyzer

Fringe rods at the entrance of the mass analyzer smooth the pathway of the incoming ions and bring them into a curved trajectory (G, *Fig. Box 5.2.2*; *Fig. Box 5.2.3C*; Bruker Aurora Training Manual, version 5.0, 2011).
The mass analyzer has a quadrupole design, consisting of four conductive rods arranged around a central axis (H, *Fig. Box 5.2.2*; *Fig. Box 5.2.3C*). The opposite pairs of rods are supplied with a radio frequency and DC potentials, respectively, finally leading to opposite polarities between the paired rods. The resulting electric field affects

all incoming ions that are vibrated oscillatory where ions with an appropriate mass-to-charge ratio are not deflected and pass the electric field on a stable path (H, *Fig. Box 5.2.2*; Bruker Aurora Training Manual, version 5.0, 2011). Ions with other mass-to-charge ratios either collide with the rods or get a slow drift in such a way that its trajectory cannot corrected anymore to a straight path through the electric field (H, *Fig. Box 5.2.2*). For an effective mass filtering, the quadrupole has to be long enough in order to guarantee a separation according to the mass-to-charge ratios, including the colliding with the rods for ions with an unstable path, in sufficient time. Further, the velocities of the ions have to be sufficient that they can be transmitted and move not too quickly through the electric field (Bruker Aurora Training Manual, version 5.0, 2011).
Due to changes of the electric field, the ions pass the quadrupole in a certain succession with increasing mass-to-charge ratios and finally are scanned as mass spectrum.

5.2.5 Detector system

The detector a discrete dynode electron multiplier (DDEM; *Fig. Box 5.2.3D*), consisting of a series of electrodes (dynodes) (I, *Fig. Box 5.2.2*). When an incoming ion strikes the first electrode, which is at a high negative potential (-2 kV), electrons are emitted (Bruker Aurora Training Manual, version 5.0, 2011). Towards the last electrode the potential decreases to ground potential (Bruker Aurora Training Manual, version 5.0, 2011). Therefore, electrons are accelerated cascade-like from electrode to electrode. During each impact at an electrode more electrons are emitted and thus, the pulse is amplified (I, *Fig. Box 5.2.2*). The procedure is repeated several times till the last electrode (I, *Fig. Box 5.2.2*). In the end a current is measured, which passes a pre-amplifier/discriminator module, where pulses with a certain threshold are amplified and therefore, the noise is reduced (J, *Fig. Box 5.2.2*). Counting electronics record the incoming pulses that are re-calculated in to counts per second by a ICP-MS Quantum software (K, *Fig. Box 5.2.2*; Bruker Aurora Training Manual, version 5.0, 2011).
The U-Pb analyses at the Department of Geology at Lund University are run in a mono-collector system in a dynamic mode (peak-hopping), i.e., the ion beam jumps between the masses for several times and each mass is counted between 10 and 40 milliseconds (dwell time) by the detector system. A complete scan over the entire mass range (^{202}Hg, ^{204}Pb, ^{206}Pb, ^{207}Pb, ^{208}Pb, ^{232}Th, ^{238}U) lies between 120 and 150 milliseconds. Each sequence includes 100-120 analyses, all set on automatic mode including laser firing, timing and data acquisition.

5.2.6 Data processing

The raw data reduction and age calculations, including data plotting, are done by Iolite (version 3.63; Paton et al., 2011) and Excel Add-In Isoplot (Ludwig, 2012), respectively. The processing of the raw data in Iolite, including baseline subtraction, correction for interferences, downhole fractionation, and mass bias, as well as calibrations, are carried out by the data reduction scheme VizualAge (Petrus and Kamber, 2012).
Once the laser file with all the information of the baseline, reference materials and unknowns is uploaded in Iolite, all signals of the reference materials and unknowns (values along the y-axis) are graphically shown in a plot vs the acquisition time along the x-axis, which enables a data processing timeslice-by-timeslice (Paton et al., 2011). At first the baseline is subtracted from the signals of the reference materials and unknowns. Afterwards, integration periods for each signal are defined. The integration periods are shown as small boxes carrying the time formation, shown along the x-axis, and with a 95% confidence interval of the average value from the y-axis (Paton et al., 2011). The integration periods can be defined for different channels (e.g., ^{238}U, ^{206}Pb, etc.; channel = Iolite term; Paton et al., 2011), which are included in each signal of the reference materials and unknowns. As the integration periods are set manually, their extent are chosen in a way that only signal areas, which are sufficient flat or with the least noise, are included.
Signals or analyses (data points) with integration periods that contain a signal duration of less than 5 seconds are excluded from age calculations. Further, analyses that partly missed the target area (zircon) during laser firing, consisting of more than one age component (rim-core), are reverse discordant, and with high common Pb contamination are excluded, too. In order to choose the analyses with the least common Pb, the $^{206}Pb/^{204}Pb$ ratio was plotted against the $^{207}Pb/^{206}Pb$ for each sample. A lower limit for the $^{206}Pb/^{204}Pb$ ratio was placed where a significant change in the $^{207}Pb/^{206}Pb$ ratio was observed. The limit of the $^{206}Pb/^{204}Pb$ ratio varies between the samples but mostly lie between 10^3 and 10^4. Based on this procedure, no common Pb corrections were performed.

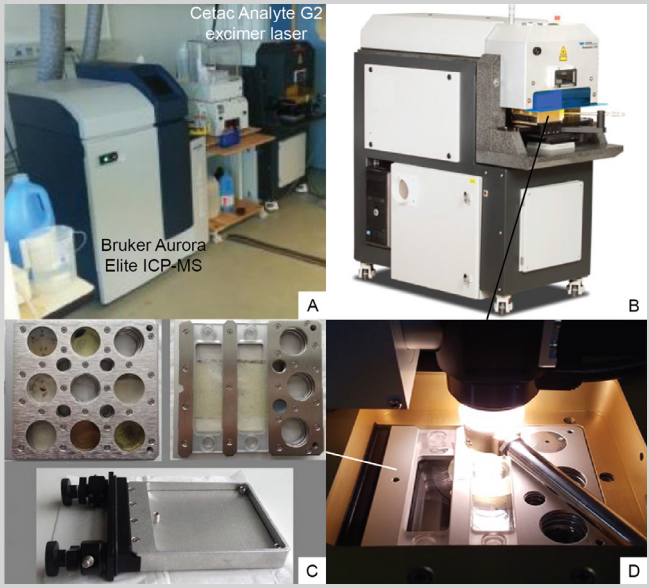

Figure Box 5.2.1 A) The LA-ICP-MS instrumentation (Bruker Aurora Elite ICP-MS) as it is used at the Department of Geology at Lund University. B) A Cetac Analyte G2 excimer laser as used in this thesis to ablate the sample material (25/03/2020: https://www.selectscience.net/products/analyte-g2-excimer-laser-ablation-system/?prodID=204411).C) Different sample holders that are used at the Department of Geology at Lund University. The sample material along with the primary and secondary reference material are placed onto the 9-hole sample holder of the upper left corner (20/03/2020: https://www.geology.lu.se/research/laboratories-equipment/laser-ablation-inductively-coupled-plasma-mass-spectrometry-la-icp-ms). D) Twovolume HelEx2 sample cell as used at the Department of Geology at Lund University. The image shows how the sample holder is incorporated into the sample cell while the laser is firing. The small black line indicates where the sample cell is situated in the laser of image B (25/03/2020: http://www.teledynecetac.com/products/laser-ablation/eqc).

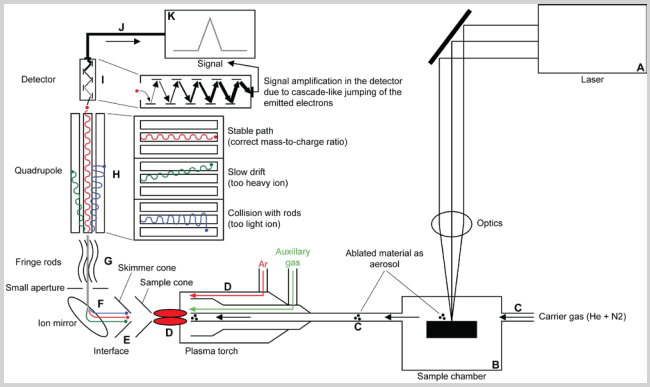

Figure Box 5.2.2 Schematic illustration of a quadrupole mass spectrometer equipped with a laser-ablation system as used at the Department of Geology at Lund University. The bold letter indicate the steps as described in the text.

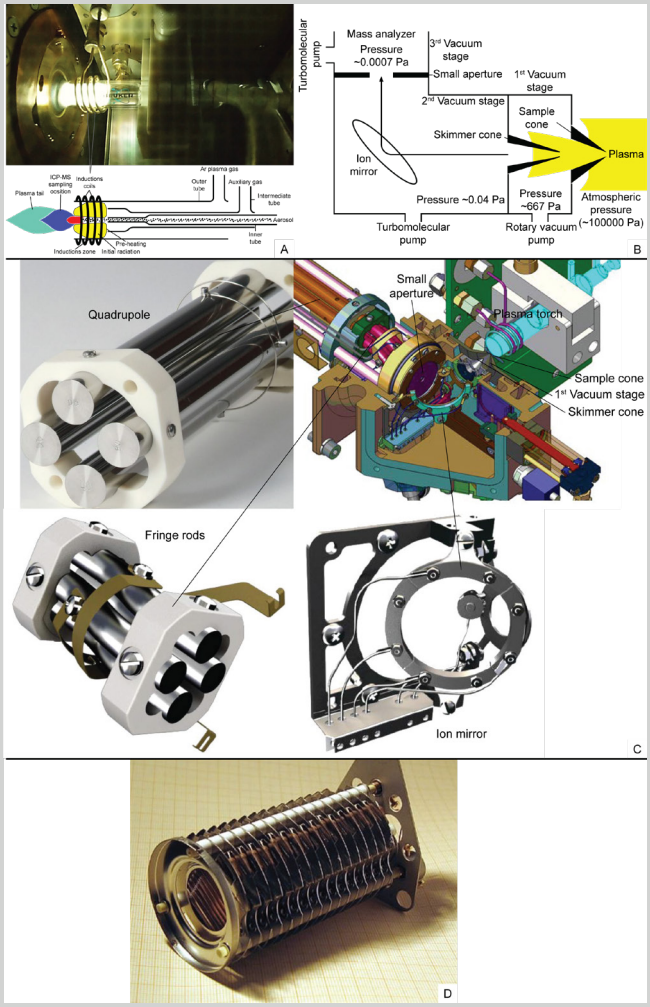

Figure Box 5.2.3 A) A plasma torch of a Bruker Aurora Elite ICP-MS showing ignited plasma (photo: Bruker Aurora Training Manual, version 5.0, 2011). The cartoon illustrates the construction of a plasma torch (modified according to Bruker Aurora Training Manual, version 5.0, 2011). B) Schematic illustration of the differential pumping system with its three vacuum stages including the interface between the sample and skimmer cone. The arrow illustrates the pathway of the ion beam generated by the plasma (modified according to Bruker Aurora Training Manual, version 5.0, 2011). C) Cross-section of a ICP-MS (image: Bruker Aurora Training Manual, version 5.0, 2011) showing the plasma torch to the right, the interface/1st vacuum stage between sample and skimmer cone, second vacuum stage with the ion mirror (central part of the image) and the small aperture which separates the second from the third vacuum stage of the mass analyzer. At the entrance of the mass analyzer are the fringe rods (image: Bruker Aurora Training Manual, version 5.0, 2011) followed by the quadrupole (25/03/2020: https://www.youtube.com/channel/ UCzKvxa5WHArynT-ImwRbd_Q) to the left. D) A discrete dynode electron multiplier (DDEM) (25/03/2020: https://www.wikiwand.com/en/Electron_multiplier).

Box 5.3 Secondary Ion Mass Spectrometry

A SIMS instrumentation consists of two main components with 1) secondary ion generation, including the primary ion source, primary ion column and secondary ion extraction, and 2) a mass analyzer with the detector system (*Fig. Box 5.3A and B*). The entire system, including sample chamber, is hold under high vacuum in order to prevent deflection of secondary ions by gas molecules or formation of unwanted secondary ions (Wiedenbeck, 2017). A high vacuum of 10^{-9} mbar is achieved by a combination of ion, turbo, scroll, Ti-sublimation pumps and a cold trap on the sample chamber (Wiedenbeck, 2017).

5.3.1 Secondary ion generation

The analysis of positive charged species, such as U and Pb, requires a negative primary ion beam, most commonly a $^{16}O^-$ primary beam (Ireland and Williams, 2003; Wiedenbeck, 2017). The $^{16}O^-$ primary beam in CAMECA ion microprobe is formed by a duoplasmatron ion source (A, *Fig. Box 5.3B* and *A*; Ireland and Williams, 2003; Joo and Liang, 2013; Wiedenbeck, 2017). Within the source, oxygen atoms interact with electrons that are emitted from a cathode filament and become negatively charged (Joo and Liang, 2013). The negative oxygen atoms are accelerated to an anode and leave the ion source as a high-speed ion beam with energies between 1 and 30 keV (Joo and Liang, 2013; EAG labs, SIMS tutorial, 2020). A positive $^{133}Cs^+$ primary beam is formed by a surface ionization source (Joo and Liang, 2013; Wiedenbeck, 2017). The primary beam column (B; *Fig. Box 5.3B*) transfers the primary ion beam into the sample chamber (C, *Fig. Box 5.3B* and *A*). Mass filters, electrostatic lenses, apertures and deflectors within the primary beam column focus and deflect the primary beam on the sample (Ireland and Williams, 2003; Joo and Liang, 2013). For the zircon U-Pb analyses, the primary beam operates in the Köhler mode (Aperture Illumination mode) (Wiedenbeck, 2017).
When the primary beam bombards the sample, its negative ions interact with the near-surface atoms (2-10 nm; Joo and Liang, 2013; EAG labs, SIMS tutorial, 2020; Schaepe et al., 2020), leading to a cascade-like displacement between them (D, *Fig. Box 5.3B*). In consequence, the bonds between the atoms are broken and they are emitted as secondary particles, leaving the samples with a kinetic energy between 0 and 100 eV (Ireland and Williams, 2003; Joo and Liang; Schaepe et al., 2020). During this so-called sputtering process, the secondary atoms become charged positively, negatively, or stay neutrally. A Au-coating on the sample avoids charging effects (Ireland and Williams, 2003). Common sputter rates lie between between 0.5 and 5.0 nm/s (EAG labs, SIMS tutorial, 2020). Due to an applied accelerating voltage between sample and an extraction plate, the positively charged secondary ions are extracted from the sample and transferred through a transfer lens to the entrance slit of the mass analyzer (E, *Fig. Box 5.3B*; Joo and Liang, 2013; Wiedenbeck, 2017).

5.3.2 Magentic sector mass analyzer

The sputtering process leads to a large energy spread between the secondary ions, which is corrected by the electrostatic analyzer (ESA), sitting behind the entrance slit (F, *Fig. Box 5.3B* and *A*). Only secondary ions with a given specific energy pass the ESA and are focused onto the energy slit (Wiedenbeck, 2017), where high-energy ions are blocked and low-energy ions pass through it (G, *Fig. Box 5.3B*; Joo and Liang, 2013). Apertures adjust the secondary beam in such way that only ions from the central part of the analysed sample area reach the mass analyzer (Ireland and Williams, 2003). In the magnetic sector mass analyzer (H; *Fig. Box 5.3B*) a magnetic field, operating perpendicular to the travel direction of the secondary ions, separate them in a manner that the heavy ions are less deflected and move along an outer trajectory. Whilst light ions, more deflected, are bent on an inner trajectory (I, *Fig. Box 5.3B*; Faure and Mensing, 2005). Thus, the heavy ions are recorded at the outer and light ions at the inner detector positions of the SIMS instrumentation (I, *Fig. Box 5.3B*).

5.3.3 Detector system

The secondary ions of U and Pb isotopes are detected in mono-collection mode (J, *Fig. Box 5.3B*) through peak-hopping by a secondary electron photomultiplier, which is operating like the electron multiplier described for the LA-ICP-MS (see *Box 5.2*, chapter 5.2.5). The SIMS electron multiplier counts the incoming secondary ions and re-calculate it into counts per second. Best operation of the electron multiplier is achieved between 0.1 and 500 kHz (Wiedenbeck, 2017). Its maximum ion counting rates is reached at 1 MHz (1 million counts/sec; Wiedenbeck, 2017). Above that the electron multiplier is saturated and shut off automatically. The secondary ion beam is then bent to the Faraday cups (Wiedenbeck, 2017). They consist of both a 10^{10} and a 10^{11} Ω resistor (Wiedenbeck, 2017), which convert the incoming ions in to a voltage signal which is finally recorded. The Faraday cups yield the best counts between 3 and 6 MHz and thus, they are suitable to analyse major elements or high

trace element concentrations with SIMS (Wiedenbeck, 2017).

Commonly, for the U-Pb analyses Zr molecular species as Zr_2O, ^{204}Pb, ^{206}Pb, ^{207}Pb, ^{208}Pb, ^{238}U, U oxides (UO and/or UO_2) and ^{230}Th are recorded in a single analysis (Ireland and Williams, 2003; Wiedenbeck, 2017). The Zr species is used both to calculate the U, Pb and Th concentrations and as mass reference for the peak position of ^{204}Pb (Ireland and Williams, 2003; Wiedenbeck, 2017). All Pb isotopes enable the determination of the amount of common and radiogenic Pb. The U oxides are important for the calculation of the Pb/U ratio of the sample and Th allow Pb/Th age calculations, which serve as basis for the Th/U ratio (Ireland and Williams, 2003). The Pb yield, i.e., counts per second, can be increased by flooding the sample chamber with oxygen. In combination with the primary beam in Köhler mode the counting rate of Pb is increased by about 4 times (Wiedenbeck, 2017).

5.3.4 Isobaric interferences

During the sputtering process, besides ions of interest, secondary molecular ions are released, as well, which form isobaric interference in particular with Pb, i.e., they have similar mass-to-charge ratios like Pb and thus, sitting on the same mass, e.g., $HfSi^+$ (M = 205.92) and $^{206}Pb^+$ (M = 205.97) (Ireland and Williams, 2003; Schoene, 2014). In order to guarantee that only the wanted secondary ions pass the mass analyzer and not interfering molecular ions, the isobaric interference has to be reduced either by energy filtering, commonly performed in small geometry SIMS instruments, or mathematically by mass resolution (Wiedenbeck, 2017). Even though both wanted secondary ions and interfering molecular ions have the same nominal masses, they still differ in their exact masses (EAG labs, SIMS tutorial, 2020), which is used for the determination of the mass resolution. It is the ratio between the mass of the ion of interest and the difference to mass of the interfering molecular ion (Wiedenbeck, 2017). A high mass resolution is able to distinguish between ionic and molecular species with similar masses (EAG labs, SIMS tutorial, 2020). Mass resolution are commonly determined for large geometry SIMS instruments like CAMECA IMS 1280. Typical high mass resolutions lie between 2000 and 4000, but can be increased to 10000 and 15000 (Schoene, 2014; Wiedenbeck, 2017). For the SIMS analyses in Paper IV, the mass resolution is set to 4860, suitable to analyse Pb.

5.3.5 Data reduction

The raw data reduction of the U-Pb analyses in Paper IV is carried out by an in-house developed excel-based spreadsheet (NordAge) written by M. J. Whitehouse (NordSIMS facility, Stockholm). The raw data are uploaded into "CIPS" where the isotopic ratios can be seen with the estimations of their uncertainties. The raw data are divided into standard spread sheet, including the primary reference material (91500), and unknowns spread sheet, including samples and secondary reference material (Tremora-2). The 91500 analyses define the Pb/U calibration curve which is used to calibrate the samples against it to obtain their true U/Pb ratios (Wiedenbeck, 2017). The calibration curve is determined by inter-element ratios under the assumption that the ionization efficiency of the reference material and sample is affected in the same way by the sputtering process (Wiedenbeck, 2017). It has been shown that the Pb^+/U^+ ratio change with respect to the UO^+/U ratio (Ireland and Williams, 2003; Wiedenbeck, 2017). It allows the determination of a correlation equation, representing the UO^+/U^+ ratio, which is used for the Pb/U ratio calculation from the Pb^+/U^+ ratio (Wiedenbeck, 2017). The final construction of the Tera-Wasserburg plots and age calculations are done by Isoplot Excel Add-in (Ludwig, 2012).

5.3.6 Ion imaging analyses

The CAMECA IMS 1280 instrument can operate in an ion microscope mode, too, and yield element distribution maps (Wiedenbeck, 2017). The primary ion beam raster over an area of the sample, which can provide elemental map images with a diameter up to 250 µm and a spatial resolution of 2 µm (Wiedenbeck, 2017). There are three approaches to achieve such maps: 1) digital maps obtained by a Resistive Anode Encoder, 2) analog maps generated by mirco-channel plates connected to a CCD camera, and 3) digital maps compiled in the scanning ion imaging mode of the microprobe (Wiedenbeck, 2017). The ion imaging analyse of Paper IV is performed by the third option, where the intensity of the secondary ion beam is recorded as a function of the primary beam position during it rasters over the analysed sample area (Wiedenbeck, 2017; EAG labs, SIMS tutorial, 2020). The primary beam of the ion imaging analyses in Paper IV has a spot size of 2 µm and raster over an area of 40x40 µm. Uranium is detected as $^{238}U\ 16O_2$ in the mono-collection mode through peak-hopping, whereas the subsequent recording of the Pb isotopes (^{204}Pb, ^{206}Pb, ^{207}Pb, ^{208}Pb) is done simultaneously in multi-collection mode (K, *Fig. Box 5.3B*). It consists of several electron photomultipliers and Faraday cups, where the latter ones sit on the highest and lowest mass (Wiedenbeck, 2017). Five isotopic species can be measured simultaneously (Wiedenbeck, 2017). The data reduction of the ion imaging analyses is carried out by the CAMECA WinImage software to construct $^{206}Pb/^{238}U$, ^{238}U and ^{206}Pb maps. An area definition tool is used to select regions of interests (ROIs) within the mapped grains, where $^{238}U/^{206}Pb$ and

$^{207}Pb/^{206}Pb$ ratios are calculated. The ratios are corrected for detector gains using the $^{206}Pb/^{238}U$ ratio = 0.17964 and for common Pb using the $^{206}Pb/^{204}Pb$ = 18.7033023 and $^{207}Pb/^{206}Pb$ = 0.835619596. Finally, the ratios are used to calculate $^{238}U/^{206}Pb$ and $^{207}Pb/^{206}Pb$ ages using equations derived from Isoplot Excel add-in (Ludwig, 2012).

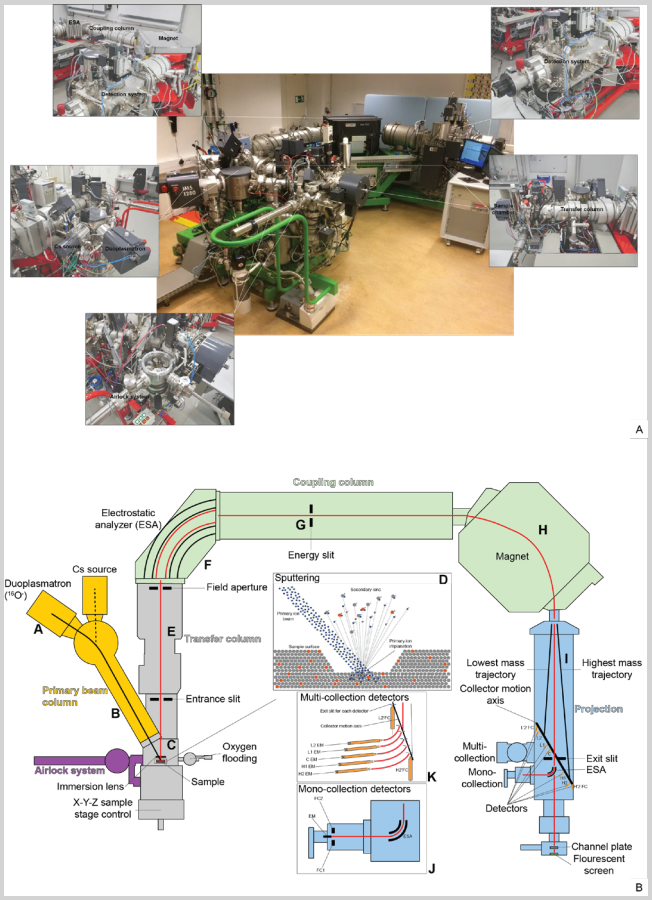

Figure Box 5.3 A) Large image in the middle shows the CAMECA IMS 1280 ion microprobe at the Swedish Museum of Natural History in Stockholm (02/07/2020: https://www.nrm.se/en/forskningochsamlingar/geovetenskap/nordsim.904.html). The small images are close-ups that show different parts of the instrumentation. Note, these close-ups were taken from the CAMECA IMS 1280-HR at the Heidelberg University, Germany (02/07/2020: https://www.geow.uni-heidelberg.de/HIP/cameca_en.html). B) Schematic illustration of a CAMECA IMS 1280 ion microprobe at the Swedish Museum of Natural History in Stockholm (NordSIMS facility). The bold letter indicate the steps as described in the text. The three insets in the middle illustrates the sputtering process, multi-collection and mono-collection detector system.

137.88. The decay constants of Steiger and Jäger (1977) are used, as well, with λ_{238} = 1.55125x10^{-10}/yr and λ_{235} = 9.8485x10^{-10}/yr.

5.4 Data presentation

There are three possibilities to present U-Pb data: Wetherill Concordia plot, Tera-Wasserburg plot and isochron plot. In Paper I the U-Pb data are presented in Wetherill Concordia plots and in Paper IV in Tera-Wasserburg plots. In general, statistical tools, such as the MSWD, facilitates the evaluation of data sets. The MSWD assesses the random scatter of the data, where an MSWD ~ 1 indicate that the scatter lies within the analytical uncertainties of the mass spectrometer analyses (Schaen et al., 2020). Whilst MSWD<1 suggests an overestimation or incorrect propagation of the analytical uncertainties (Schaen et al., 2020) and MSWD>1 indicate a scatter not caused by analytical uncertainties alone, but reflect a geological perturbation such as partial loss of radiogenic daughter isotopes (Schaen et al., 2020).

5.4.1 Wetherill Concordia plot

The concordia diagram was introduced by Wetherill (1956) where $^{206}Pb/^{238}U$ is plotted against $^{207}Pb/^{235}U$ (Fig. 5.3A). The concordia curve is derived by a set of solutions calculated by the following equations where t = constant (Schoene, 2014):

$$(^{206}Pb/^{238}U) = (e^{\lambda 238t} - 1)$$
$$(^{207}Pb/^{235}U) = (e^{\lambda 235t} - 1)$$

Three different data types are distinguished, concordant, discordant and reverse discordant, which enable an internal check whether the U-Pb system remained closed over time. $^{206}Pb/^{238}U$ and $^{207}Pb/^{235}U$ ratios that are consistent in their dates fall onto the concordia curve, i.e., are concordant and indicate closed-system behaviour (Fig. 5.3A; Faure and Mensing, 2005; Schoene, 2014). Whilst in an open U-Pb system, the $^{206}Pb/^{238}U$ and $^{207}Pb/^{235}U$ ratios yield unequal dates, providing discordant data that plot below or above the concordia curve (Fig. 5.3A; Faure and Mensing, 2005; Schoene, 2014). Commonly a regression line, so-called discordia, can be drawn through the discordant points which intersects the concordia curve in an upper and lower intercept (Fig. 5.3A). For igneous rocks, the upper intercept is often interpreted to represent the crystallisation age. The lower intercept is typically interpreted to represent the time of isotopic disturbance, e.g., Pb loss (see chapter 5.5; Fig. 5.3A; Schoene, 2014). Further cause for data discordance could be that different-aged domains are mixed and the gain or loss of intermediate daughter isotopes (Schoene, 2014). Data points above the concordia curve are reversely discordant (Fig. 5.3A). They seldom originate from natural processes and can be rather explained by problems in the calibration or analytical procedure (Schoene, 2014).

5.4.2 Tera-Wasserburg plot

Tera-Wasserburg plots the $^{238}U/^{206}Pb$ ratio along the x-axis against the $^{207}Pb/^{206}Pb$ ratio along the y-axis, with a concordia curve derived in a similar manner as for the Wetherill Concordia plot (Fig. 5.3B; Schoene, 2014).

The interpretation of the different data types, i.e., concordant, discordant and reversely discordant, are identically to the Wetherill Concordia plot (Fig. 5.3B). Thus, the Tera-Wasserburg diagram facilitates to test for open or closed-system behaviour, where the upper and lower intercepts are derived by a discordia regressed through discordant data points (Fig. 5.3B; Schoene, 2014). Additionally, the upper intercept yields the value for the initial Pb composition, due to the intersection of the discordia with the y-axis (Fig. 5.3B; Schoene, 2014).

5.4.3 Isochron plot

In a isochron plot the isotopes of both U-Pb decay systems are standardized against the non-radiogenic ^{204}Pb (Fig. 5.3C), where the following equations are used to construct an isochron diagram:

$$(^{206}Pb/^{204}Pb) = (^{206}Pb/^{204}Pb)_0 + (^{238}U/^{204}Pb)\ (e^{\lambda 238t} - 1)$$
$$(^{207}Pb/^{204}Pb) = (^{207}Pb/^{204}Pb)_0 + (^{235}U/^{204}Pb)\ (e^{\lambda 235t} - 1)$$

It is assumed that for a set of minerals, coming from the same sample, the initial ($^{206}Pb/^{204}Pb$) and ($^{207}Pb/^{204}Pb$) ratios are identical (Fig. 5.3C). However, the $^{238}U/^{204}Pb$ and $^{235}U/^{204}Pb$ ratios are variable. As with increasing time the U decays, the $^{238}U/^{204}Pb$ and $^{235}U/^{204}Pb$ ratios decrease while the $^{206}Pb/^{204}Pb$ and $^{207}Pb/^{204}Pb$ increase. But due to different start U concentrations, the increase varies resulting in different $^{206}Pb/^{204}Pb$ and $^{207}Pb/^{204}Pb$ ratios which should fit on a regression line (Fig. 5.3C). Its intersection with the y-axis yields the value for the initial isotopic Pb composition (Fig. 5.3C).
According to the equation of a straight line, the slope m of the regression line yields the age (Fig. 5.3C), e.g.:

$$y = n + xm$$
$$(^{206}Pb/^{204}Pb) = (^{206}Pb/^{204}Pb)_0 + (^{238}U/^{204}Pb)\ (e^{\lambda 238t} - 1)$$
$$[((^{206}Pb/^{204}Pb)-(^{206}Pb/^{204}Pb)_0)/(^{238}U/^{204}Pb)] = (e^{\lambda 238t} - 1)$$

5.5 Pb loss

Under dry conditions at high temperatures above the T_C of Pb (>900°C; Cherniak and Watson, 2000), Pb loss in crystalline zircon is controlled by volume diffusion through the crystal lattice (Tilton, 1960; Lee et al., 1997; Cherniak and Watson, 2000). Whilst under common crustal conditions, far below 900°C, Pb loss in reasonable geological times is only possible in metamict zircon (Mezger and Krogstad, 1997), which is discussed in Paper I. Metamictization is interpreted as radiation damage of the zircon lattice, due to the radioactive U decay, where 7-8 alpha particles are emitted within each U isotope decay scheme (Fig. 5.1; Ewing et al. 2003, Schoene 2014).

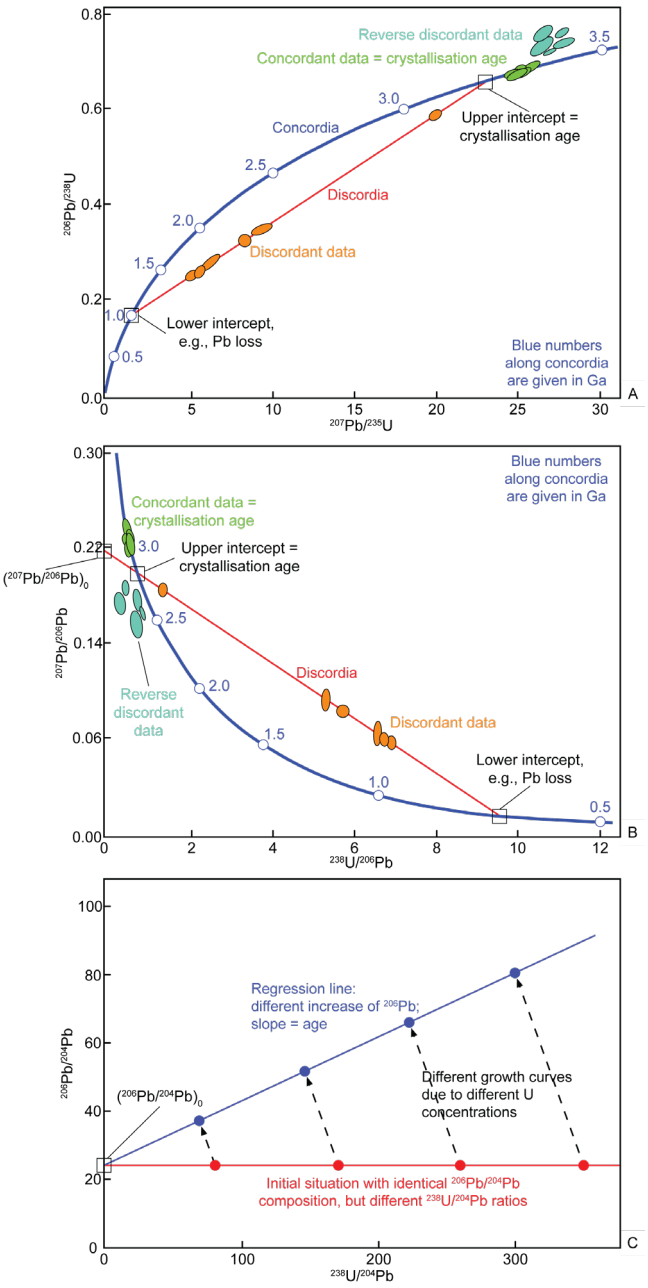

Figure 5.3 A) An example of a Wetherill Concordia plot as used in this thesis. The curvature of the concordia is controlled by different T1/2 of ^{238}U and ^{235}U, where ^{235}U with a shorter $T_{1/2} = 0.704x10^9$ yr decays faster than ^{238}U with T1/2 = $4.468x10^9$ yr. B) Tera-Wasserburg plot. The different types of data points are interpreted in the same fashion as for the Wetherill Concordia plot. C) Isochron plot with fictional data points. The red line illustrates the initial situation and the blue regression line after the growth of ^{206}Pb due to the decay of ^{238}U.

Their simultaneous recoil with radiogenic daughter nuclei cause a cascade-like permanent displacement of several atoms, producing alpha recoil and fission tracks that leads to a metamict state (Ewing et al., 1987, 2003; Meldrum et al., 1998; Nasdala et al., 2001). In radiation-damaged lattice, the Pb diffusion is enhanced and thus, metamict zircon is more prone to lose Pb, resulting in discordance (Cherniak et al., 1991; Nasdala et al., 1998; Geisler et al., 2007). Zircon accumulates radiation damage over time at temperatures below 650°C, where Pb loss is controlled either by diffusion through the damaged lattice, by leach-

ing or by recrystallisation of the metamict domains under the presence of hydrothermal fluids (Pidgeon et al., 1966; Sinha et al., 1992; Mezger and Krogstad, 1997; Rizvanova et al., 2000; Cherniak et al., 1991; Cherniak and Watson, 2003; Geisler et al., 2001, 2002, 2003, 2007). The recrystallisation or annealing of radiation damage tracks such as alpha recoil and fission tracks can still continue at significant lower temperatures between 200 and 250°C (discussed in Paper I; Yamada et al., 1995; Tagami and Shimada, 1996; Tagami et al., 1996; Nasdala et al., 2001; Hasebe et al., 2003).

Lead loss from zircon during an impact event is either induced by the recrystallisation into a neoblastic texture or by new growth of a zircon grain, both excluding Pb due to its incompatibility in the zircon lattice. Radiation-damaged domains are considered as nucleation sites for neoblasts (Schmieder et al., 2015), indicating that the metamict state of a zircon may promote the recrystallisation of neoblastic as well as porous texture during an impact event (discussed in Paper IV).

5.6 Common Pb

Common Pb is the non-radiogenic Pb component, composed of ^{204}Pb, ^{206}Pb, ^{207}Pb, and ^{208}Pb. It can be incorporated into the U-Pb system initially during the crystallization, during subsequent processes such as hydrothermal activity (Watson et al., 1997), or through contamination during the sample preparation and/or analysis (Andersen, 2002).

Common Pb causes, like Pb loss, discordant data, but in such a way that the slope of the discordia can show a very high steepness resulting in upper intercepts with ages older than the Earth (Schoene, 2014). Therefore, the U-Pb analyses have to be corrected for common Pb. There are several approaches. Conventional corrections based on the analysis of the non-radiogenic ^{204}Pb to monitor the common Pb component. It is either measured on a Pb-rich mineral with low U and Th concentrations, such as feldspar, or stem from estimations based on Pb growth curves (Andersen, 2002; Ireland and Williams, 2003; Petrus and Kramer, 2012). The common Pb correction of the SIMS analyses in Paper IV are done using the ^{204}Pb counts to estimate the common ^{206}Pb-percentage of the total amount of ^{206}Pb. It is based on the assumption of a modern-day Pb isotope composition by Stacey and Kramer (1975). However, when the ^{204}Pb is difficult to estimate as for LA-ICP-MS, the Andersen procedure is used to correct for common Pb (Andersen, 2002). As the signal for ^{204}Pb is too low and thus, often disappears in the background, the LA-ICP-MS is not able to measure the ^{204}Pb signal sufficient precisely. The data reduction scheme VizualAge used in Paper I provide common Pb corrected data based on both the conventional correction method that measures ^{204}Pb and the Andersen procedure (Petrus and Kamber, 2012). During the LA-ICP-MS analyses it was partly possible to record ^{204}Pb, but still the corrected U-Pb data seem to suffer from overcorrection. Therefore, in Paper I only data points with the least common Pb contamination are included in further calculations (no common Pb corrections).

6. $^{40}Ar/^{39}Ar$ chronometer

6.1 Overview

The K-Ar and $^{40}Ar/^{39}Ar$ dating methods are based on the radioactive decay of ^{40}K to ^{40}Ar. The alkali metal potassium and noble gas argon were discovered in the early and late nineteenth century, respectively (Davy, 1808; Rayleigh and Ramsay, 1895; McDougall and Harrison, 1999). Potassium consists of three natural isotopes (^{41}K = 93.2581 ± 0.0029%; ^{40}K = 0.01167 ± 0.00004%; ^{39}K = 6.7302 ± 0.0029%; McDougall and Harrison, 1999), where at first the non-radioactive ^{41}K and ^{39}K were discovered by Aston (1921; see McDougall and Harrison, 1999). Klempere (1935) and Newman and Walke (1935) suggested that ^{40}K was probably radioactive, which was confirmed by several studies (e.g., Nier, 1935; Smythe and Hemmendinger; see McDougall and Harrison, 1999). Further, Newman and Walke (1935) and later von Weizsäcker (1937) argued that ^{40}K has a branched decay to ^{40}Ca and ^{40}Ar (McDougall and Harrison, 1999). About 90% of the ^{40}K decays to ^{40}Ca through a β^--decay (Fig. 6.1; McDougall and Harrison, 1999; Kelley, 2002a). The remaining 10% of ^{40}K decays with $T_{1/2}$ = 1250 Ma to ^{40}Ar, occurring in two different modes either by electron capture or emission of a positron (β^+) (Fig. 6.1; McDougall and Harrison, 1999). The ^{40}K-^{40}Ar branch builds the basis for the K-Ar and $^{40}Ar/^{39}Ar$ dating. Whilst the ^{40}K-^{40}Ca branch is only suitable for the dating of low Ca-minerals. ^{40}Ca is one of the most common natural isotopes in rock-forming minerals and therefore, difficult to discriminate it from low amounts of radiogenic ^{40}Ca. Von Weizsäcker (1937) observed a three orders of magnitude higher concentration of argon in the atmosphere relative to other noble gases and concluded that the excess was generated from the ^{40}K-decay in K-bearing rocks and minerals (McDougall and Harrison, 1999). This was confirmed by Aldrich and Nier (1948), who analysed several

K-bearing mineral phases in which a higher amount of ^{40}Ar relative to ^{36}Ar was measured in comparison to the atmospheric $^{40}Ar/^{36}Ar$ ratio. In this study, they determined the first K-Ar ages, as well (McDougall and Harrison, 1999). Aldrich and Nier (1948) suggested that under the usage of an accurate decay constant the ^{40}K-^{40}Ar decay can be used to determine ages (McDougall and Harrison, 1999). Since Aldrich and Nier (1948), the K-Ar method experienced a rapid development and is widely applied to K-bearing minerals and rocks. In this thesis both individual mineral phases, such as biotite and amphibole (Paper II), and whole rock material, such as impact melts (Paper III and V), are investigated. Their incorporation of ^{40}K and discrimination of ^{40}Ar making these mineral phases suitable for K-Ar and $^{40}Ar/^{39}Ar$ dating. In traditional K-Ar dating, the parent (K) is analysed through flame photometry, X-ray fluorescence, or isotope dilution and the daughter (Ar) is measured by isotope-dilution noble-gas mass spectrometry (Schaen et al., 2020). Thus, the sample material has to be divided in to two aliquots in order to analyse both the parent and daughter isotopes, which is both time-consuming and can introduce additional analytical uncertainties due to sample inhomogeneity.

The $^{40}Ar/^{39}Ar$ dating method is based on the production of ^{39}Ar from ^{39}K during the irradiation of sample material with fast neutrons in a nuclear reactor. It was first described in a conference abstract by Merrihue (1965), who observed ^{39}Ar production during the neutron irradiation of a meteorite and concluded that it was due to the neutron-interaction with ^{39}K. This reaction forms the basis of the $^{40}Ar/^{39}Ar$ dating technique, which is described in detail by Merrihue and Turner (1966), where the artificial generated ^{39}Ar is used as a proxy for ^{40}K, assuming that the $^{40}K/^{39}K$ ratio of 0.01167 (Garner et al., 1975) is a constant. The great advantage of the $^{40}Ar/^{39}Ar$ dating, compared to the K-Ar method, is that is allows both parent and daughter isotopes to be analysed in a single experiment on a noble gas mass spectrometer. Thus, it is more time-efficient, avoiding inhomogeneities related to the K and Ar distribution when splitting the sample, and parent/daughter isotope ratios can be measured more precisely (McDougall and Harrison, 1999; Kelley, 2002a). Further, the $^{40}Ar/^{39}Ar$ method enables the determination of multiple ages on one sample through step-heating experiments using a laser or furnace. Due to a different retentivity, argon is extracted from different domains or mineral phases which gives information about the thermal history of a sample, e.g., disturbance by a thermal event such as an impact event (Paper III and V) or by low-temperature processes such as hydrothermal alteration (Paper II; McDougall and Harrison, 1999).

It is important to note that $^{40}Ar/^{39}Ar$ dating is a relative method which requires that the sample material is irradiated together with a fluence monitor, a mineral of known age (McDougall and Harrison, 1999). In order to have control over the fast-neutron dose and how much ^{39}Ar is generated from ^{39}K in the sample material, the $^{40}Ar^*/^{39}Ar_K$ ratio of the fluence monitor is used to calculate the dimensionless irradiation parameter J through the following equation (Mitchell, 1968; McDougall and Harrison, 1999; Faure and Mensing, 2005):

$$J = [(e^{\lambda \text{ total } t \text{ monitor}} - 1)/(^{40}Ar^*/^{39}Ar_K)]$$

with λ equals the decay constant and t is the age of the flux monitor.

In this thesis, FC-2 (28.201 ± 0.046 Ma; Kuiper et al., 2008; Paper II and III), a sanidine from the Fish Canyon Tuff, and TC (28.608 ± 0.033; Renne et al., 2011; Paper V), a sanidine from the Taylor Creek Rhyolite, are used as neutron flux monitors.

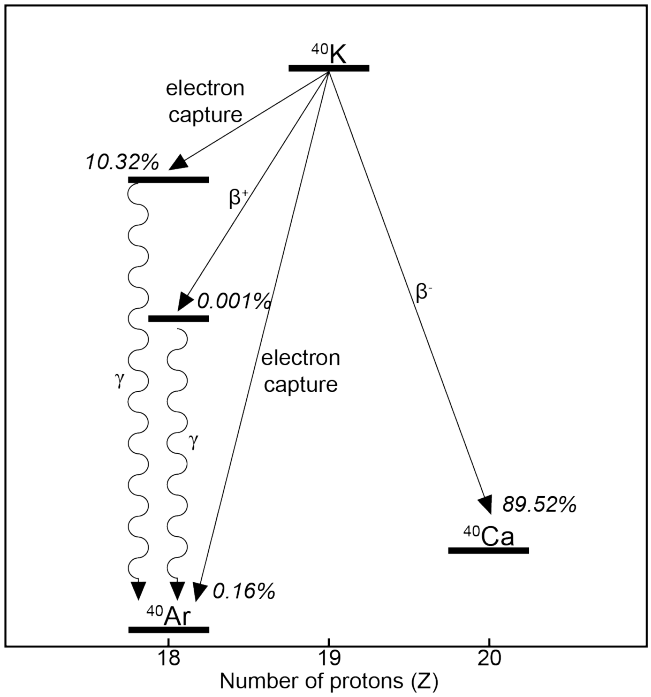

Figure 6.1 Branched decay of ^{40}K to ^{40}Ca (~90%) and ^{40}Ar (~10%), occurring in three modes 1) the majority (10.32%) of the electron captures generate ^{40}Ar, which is in an excited state, where due to subsequent γ-ray emission, it yields its ground state, 2) about 0.001% of the ^{40}K decays to ^{40}Ar in an excited state by emission of a positron (β^+), where again due to subsequent γ-ray emission, ^{40}Ar reach its ground state, and 3) about 0.016% of the electron captures produce ^{40}Ar directly in the ground state (modified according to McDougall and Harrison, 1999). During an electron capture reaction, a proton of the nucleus captures an external electron and transforms to a neutron.

6.2 Closure temperature in $^{40}Ar/^{39}Ar$ dating

Argon is a noble gas and due to its large ionic radius (1.9 Å; McDougall and Harrison, 1999), it is highly incompatible and thus, tends to diffuse out from a solid system/mineral through the lattice or along grain boundaries (Kelley, 2002a and b). The T_C with respect to argon for silicate minerals is relatively low (150-580°C; McDougall and Harrison, 1999; Reiners et al., 2005, and references

therein) in comparison to Pb diffusion in zircon (T_C>900°C; Cherniak and Watson, 2000). For example, amphibole has a T_C of between 480 and 580°C (Harrison, 1981; Dahl, 1996), whereas biotite yields a much lower T_C interval with 280-350°C (Harrison et al., 1985; Grove and Harrison, 1996). Thus, the $^{40}Ar/^{39}Ar$ method is useful for yielding cooling ages of crystalline basement rocks. It is also a viable technique for dating impact structures, where the target rock was exposed to extreme temperature conditions that would likely lead to a partial or total reset of the K-Ar system. In particular, $^{40}Ar/^{39}Ar$ dates of fully outgassed and rapidly quenched impact melts should closely reflect the age of an impact event (Paper III and V). Further, as the T_C is relatively low, post-impact processes, such as hydrothermal fluid activity, are sufficient to affect the K-Ar system of biotite and amphibole, giving $^{40}Ar/^{39}Ar$ dates that post-date an impact rather than being directly related to an event (Paper II).

6.3 Methodology

6.3.1 Sample preparation

The preparation of the mineral separates in Paper II and impact melts in Paper V are performed at the Department of Geology at Lund University. It starts in a similar manner to the zircon preparation for U-Pb (see chapter 5.3.1), where, however, the final step is the hand-picking from the 250-500 µm size fraction without subsequent density separation or casting in epoxy. Due to its general higher K content, about 10-20 mg of biotite (K = 7-8%; McDougall and Harrison, 1999) are separated, whereas amphibole generally with K = 0.1-1.0% (McDougall and Harrison, 1999) about 50-100 mg.

The preparation of the impact melt samples in Paper III is done at the Natural History Museum of Denmark in Copenhagen. Micro-X-ray fluorescence analysis (Flude et al., 2017) is carried out prior to the sample preparation using a Bruker M4 Tornado with a beam current of 200 µA and a beam voltage of 50 kV (Fig. 6.2A). This kind of analysis enables a quick (max. 1 hour in this thesis) and non-destructive elemental characterization of the sample material. Each impact melt sample is scanned on automatic run on several sites with an area of 8.59x12.70 mm in order to identify potential, K-rich sites for the sample preparation. Once, the sites are selected, mm-sized whole-rock cores are drill out by a Dremel mini-driller (Fig. 6.2B and C). From each impact melt sample one to four sub-samples were taken. (Fig. 6.2C)

In a final preparation step, all separated sample material are cleaned in deionized water and ethanol in an ultrasonic bath.

The following sections refer solely to Paper II and Paper III. For the irradiation, the separated grains and mini cores are placed along with the fluence monitors into individual mm-sized wells (different in diameter) on several aluminium discs (diameter = 18 mm) (Fig. 6.2D). The samples and fluence monitors are geometrical arranged in such a manner that each sample is surrounded by sufficient fluence monitors in order to achieve an accurate and precise determination of the J values (Fig. 6.2D). After the sample loading for the irradiation, the aluminium discs are stacked forming an irradiation batch, wrapped in aluminium foil and encapsulated in a heat-sealed quartz glass tube (Fig. 6.2E and F).

6.3.2 Neutron irradiation, ^{39}Ar recoil effect and interfering reactions

Based on the ages of the samples and fluence monitors, an optimal neutron flux has to be find with an irradiation duration set to be sufficient to meet the three main criteria by Turner (1971), i.e., 1) to produce enough ^{39}Ar from the in-situ decay of ^{39}K to enable accurate age determinations, 2) to minimize the production of interfering ^{40}Ar due to the ^{40}K decay ($^{40}K(n,p)^{40}Ar$; Tab. 6.1), and 3) to minimize the production of interfering ^{36}Ar due to the ^{40}Ca decay ($^{40}Ca(n,n\alpha)^{36}Ar$; Tab. 6.1) that the atmospheric ^{40}Ar correction can be carried out properly. Younger samples with a short time elapsed since the closing of the isotopic system, produced less amounts of ^{40}Ar from the ^{40}K decay. Thus, the irradiation is set adequately short even down to the range of minutes. However, the samples analysed in this thesis are basically older than 100 Ma, i.e., they could accumulate comparatively more ^{40}Ar. Therefore, the irradiation duration is set to about 40 hours to generate sufficient ^{39}Ar which is comparable to the amount of the natural produced ^{40}Ar.

Sample material in Paper II and III are irradiated at the TRIGA research nuclear facility of the Oregon State University, USA. It is a MW TRIGA Mark II pulsing research reactor cooled by water where uranium and zirconium-hydride fuel elements are used that are grouped in a circular grid. The reactor core, located in a water-filled tank, is surrounded by a graphite slab where the neutrons are reflected towards the core. For $^{40}Ar/^{39}Ar$ experiments, the sample material and fluence monitor are shielded from slow neutrons by a Cadmium-Lined In-Core Irradiation Tube (CLICIT) in order to minimize ^{36}Ar production from ^{40}Ca. Both sample material and fluence monitor are placed in an aluminium TRIGA tube during the irradiation procedure.

During the intended reaction interacts a ^{39}K nucleus with a neutron and is transformed to ^{39}Ar under the emission of a proton (McDougall and Harrison, 1999):

$$^{39}_{19}K + ^{1}_{0}n = ^{39}_{18}Ar + ^{1}_{1}H$$

Table 6.1 Neutron-induced reactions during the irradiation in the reactor.

	Target element			
Argon isotope	Ca	K	Ar	Cl
^{36}Ar	**^{40}Ca(n,nα)^{36}Ar**			^{35}Cl(n,γ)^{36}Cl-->β^{-}-->^{36}Ar
^{37}Ar	**^{40}Ca(n,α)^{37}Ar**	^{39}K(n,nd)^{37}Ar	^{36}Ar(n,γ)^{37}Ar	
^{38}Ar	^{42}Ca(n,nα)^{38}Ar	^{39}K(n,d)^{38}Ar ^{41}K(n,α)^{38}Cl-->β^{-}-->^{38}Ar	^{40}Ar(n,nd)^{38}Cl-->β^{-}-->^{38}Ar	^{37}Cl(n,γ)^{38}Cl-->β^{-}-->^{38}Ar
^{39}Ar	**^{42}Ca(n,α)^{39}Ar** ^{43}Ca(n,nα)^{39}Ar	**^{39}K(n,p)^{39}Ar** ^{40}K(n,d)^{39}Ar	^{38}Ar(n,γ)^{39}Ar ^{40}Ar(n,d)^{39}Ar-->β^{-}-->^{39}Ar	
^{40}Ar	^{43}Ca(n,α)^{40}Ar ^{44}Ca(n,nα)^{40}Ar	**^{40}K(n,p)^{40}Ar** ^{41}K(n,d)^{40}Ar		

In bold marks the important interfering nuclear reactions, which have to be corrected. Bold, red type marks the reaction crucial for the ^{40}Ar/^{39}Ar analysis.

The shorthand-written reaction is following:

$$^{39}\text{K(n,p)}^{39}\text{Ar}$$

where in brackets between the parent and daughter isotope are the bombarded (n) and the emitted (p) particles included in this reaction (Tab. 6.1; McDougall and Harrison, 1999).

Undesirable consequences of the neutron irradiation that have to be considered are the 1) ^{39}Ar recoil effect, and 2) reactions that produce interfering Ar isotopes (Tab. 6.1), which requires correcting for in order to calculate accurate ^{40}Ar/^{39}Ar ages.

The energy release of about 100 to 200 keV (McDougall and Harrison, 1999) during the neutron-induced ^{39}K decay provokes the displacement of ^{39}Ar over a distance between 820 and 3780 Å (0.082-0.378 µm; Turner and Cadogan, 1974, Huneke and Smith, 1976, Onstott et al., 1995). As dealing with fine-grained material such as impact melts in Paper III and V, or with textures on µm-scale, such as the strong intergrowth between biotite and chlorite in Paper II, the recoil of ^{39}Ar can be a serious problem. ^{39}Ar either escapes near the sample surface or it is displaced from a K-rich phase (e.g., biotite) to a neighbouring K-poor phase (e.g., chlorite) (McDougall and Harrison, 1999), leading to a depletion of ^{39}Ar the K-rich phase.

Important interfering reactions are caused by ^{42}Ca and ^{40}Ca that produces ^{39}Ar and ^{36}Ar, respectively (Tab. 6.1). It is also vital to know how much ^{36}Ar was generated by the reactor interfering reactions in order to make an accurate estimate of the non-radiogenic (atmospheric) argon component for model age calculations. To correct for the Ca-interfering reactions, ^{36}Ar and ^{39}Ar are measured relative to ^{37}Ar, an isotope exclusively formed from ^{40}Ca (Tab. 6.1), carried out on an irradiated pure calcium salt, e.g., CaF_2 (McDougall and Harrison, 1999). However, due to the short half-life of about 35 days of ^{37}Ar, the subsequent ^{40}Ar/^{39}Ar analyses have to be done shortly after the irradiation (McDougall and Harrison, 1999). Slow neutron reactions of ^{40}K to ^{40}Ar, ^{38}Ar and ^{37}Ar (Tab. 6.1) can be reduced by cadmium shielding. The correction factors are determined in a similar manner than for calcium through the measurements of ^{40}Ar, ^{38}Ar and ^{37}Ar relative to ^{39}Ar on a pure potassium salt, e.g., K_2SO_4, or on a synthesized potassium-rich silicate glass (McDougall and Harrison, 1999).

Reactions with ^{35}Cl and ^{37}Cl to ^{36}Ar and ^{38}Ar, respectively (Tab. 6.1), are negligible, but could be crucial for minerals with high Cl/^{40}Ar ratios like for hornblende. It can be monitored by using a mineral with known Cl content (McDougall and Harrison, 1999).

6.3.3 ^{40}Ar/^{39}Ar analyses

After the irradiation the samples are stored for several months in order to allow the decay of short-lived radionuclides. For ^{40}Ar/^{39}Ar analyses in Paper II and III, the irradiated samples together with the fluence monitors are transferred into individual mm-sized wells in a stainless steel laser disc (diameter = 6 cm; Fig. 6.2G). The ^{40}Ar/^{39}Ar analyses are carried out at the Quaternary Dating Laboratory (Quadlab), Natural History Museum of Denmark in Copenhagen using a fully automated Nu Instruments Noblesse multi-collector noble gas mass spectrometer (*Fig. Box 6.1A and B*) in which the argon was extracted from the samples in laser step heating experiments (*Fig. Box 6.1C and D*). In a step heating procedure, the argon is released in incremental gas fractions by increasing the output laser power until the sample is completely degassed. As there are several possible argon reservoirs with different isotopic compositions (McDougall and Harrison, 1999), step heating experiments can often detect these different domains. For instance, alteration causes argon loss in a crystal, leading to lower ^{40}Ar*/^{40}K ratios and in consequence, to apparent younger ages at lower power laser steps. Those differences in relation to more retentive sites can be observed by a step heating procedure

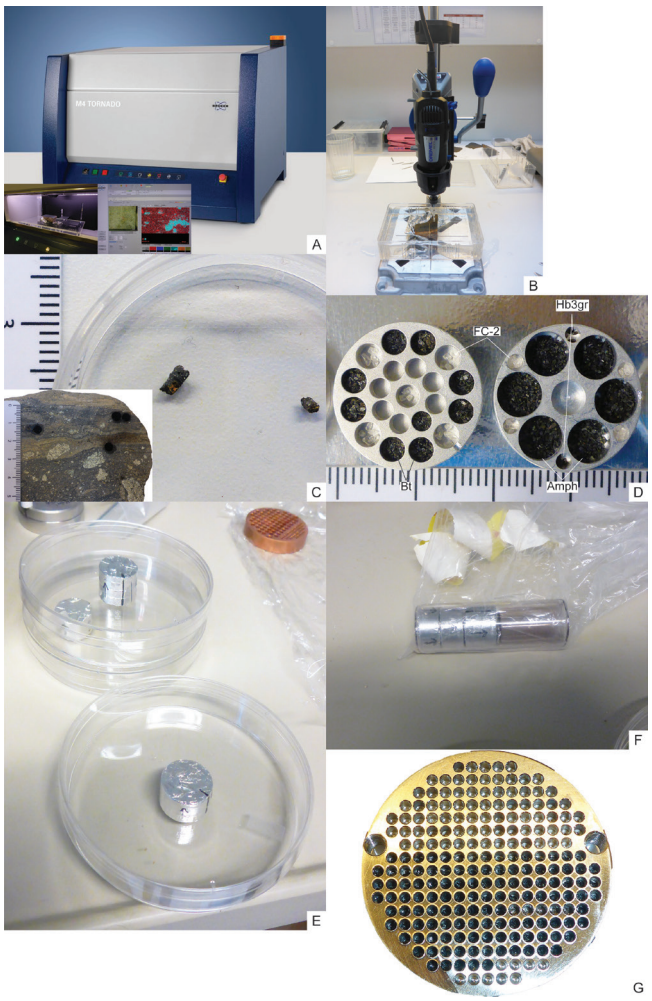

Figure 6.2 A) Bruker M4 Tornado (18/03/2020: https://mms.businesswire.com/media/20160307006074/en/513081/5/4-M4_Tornado.jpg) used for μ-XRF analyses to identify K-rich sites as potential sample sites within the impact melt samples. The right inset shows the sample chamber of the instrumentation. The left inset shows a screen shot of the data acquisition during the scanning of an impact melt sample (HUM 15-01J; see Paper III) (photos of the two insets: author of this thesis, 09/02/2017). B) Dremel mini-driller to take mini cores from the impact melt samples (photo: author of this thesis, 03/03/2017). C) Millimeter-sized mini cores of an impact melt sample. Inset to the left shows the different drilling sites (MIE 15-03J; see Paper III) (photos: author of this thesis, 03/03/2017). D) Aluminium disc used for the irradiation of the sample material. The left disc shows the geometrical arrangement of Fish Canyon sanidine (FC-2; fluence monitor) and biotite samples (for Paper II). The right disc shows the geometrical arrangement between FC-2, and amphibole (for Paper II) and hornblende of Hb3gr, a fluence monitor, however, not used in this thesis (photos: author of this thesis, 21/01/2017). E) Aluminium discs stacked to an irradiation batch (here situation after irradiation) and wrapped in Al foil (photo: author of this thesis, 04/01/2018). F) Stacked Al discs encapsulated in a heat-sealed quartz glass tube (here situation after the irradiation; photo: author of this thesis, 04/01/2018). G) Stainless steel laser disc as used for the analyses of the samples in a step- heating procedure (photo: author of this thesis, 05/01/2018).

and finally excluded from subsequent age calculations. After the cleaning of the released argon from reactive gases in a cold trap and getter pump system (*Fig. Box 6.1E*), the isotopic analysis of unknowns, blanks, and monitor minerals were carried out in identical fashion on the Noblesse mass spectrometer, in which ^{40}Ar and ^{39}Ar were measured on the high-mass Faraday detector (F), ^{38}Ar and ^{37}Ar on the axial ion counter (AxIC), and ^{36}Ar on the low-mass ion counter (LoIC). Measurements of ^{40}Ar, ^{38}Ar, and ^{36}Ar ion beams were carried out simultaneously, followed by sequential measurements of ^{39}Ar and ^{37}Ar. The data collection and reduction were carried out using the program "Mass Spec" (by A. Deino, Berkeley Geochronology Center, Berkeley, CA). Detector intercalibration and instrumental mass fractionation was determined following previously documented procedures (e.g., Storey et al., 2012) by using a series of atmospheric argon aliquots delivered from a calibrated air pipette using the following detector configuration ($^{40}Ar/^{36}Ar$)F/LoIC, ($^{40}Ar/^{38}Ar$)F/AxIC, and ($^{40}Ar/^{36}Ar$)F/AxIC. For more details, see *Box 6*.

6.3.4 Age calculation

Starting with the basic age equation:

$$D = D_0 + N (e^{\lambda t} - 1)$$

Converted to t, it gives the following equation:

$$t = 1\lambda^{-} \ln[DN^{-} + 1]$$

under the assumption $D_0 = 0$ (no initial daughter isotopes, all are exclusively radiogenic) at t = 0.
Transferred to the $^{40}Ar/^{39}Ar$ dating, the ages are calculated by the following equation (McDougall and Harrison, 1999; Kelley, 2002b):

$$t = 1\lambda^{-} \ln[1 + J (^{40}Ar^{*}/^{39}Ar_K)]$$

with t equals time, λ is the decay constant of ^{40}K, J is the irradiation parameter and * means radiogenic.
Due to the branched decay of ^{40}K, its total decay constant includes the partial decay constants from both the β^- decay to ^{40}Ca and the electron capture to ^{40}Ar. They have been re-determined by various studies, summarized in Table 6.2 (Rivera, 2013). In Paper II and III, the total decay constant ($5.463 \pm 0.054 \times 10^{-10}$/yr) of Min et al. (2000) is used.
Errors that must be considered, contributing to the age calculation, are instrumental uncertainties such as detector intercalibration and the analytical precision of individual $^{40}Ar^{*}/^{39}Ar_K$ analyses, the error in J, interference corrections, uncertainties in the age of the fluence monitor, and in the decay constant.

6.4 Data presentation

$^{40}Ar/^{39}Ar$ data can be presented in several ways, where the age data are commonly presented in age spectra and isochron plots, including normal and inverse plots. Further, Arrhenius plots are used to present Ar diffusion

Box 6 Gas-source Mass Spectrometer

A noble gas mass spectrometer consists of two components 1) the ultrahigh vacuum line where the argon is extracted and purified, and 2) a mass spectrometer to analyses the isotopic argon composition of the samples (*Fig. Box 6.2*). The entire extraction system is connected through manually and automatically controlled valves (*Fig. Box 6.2*), where the movement of the release argon gas within the system can be regulated. Due to low blanks the entire system has to be kept under ultrahigh vacuum (UHV), which is achieved by several turbomolecular and ion pumps (*Fig. Box 6.2*).

6.1 Argon release system

The argon release is done by a defocused 50-W Synrad CO_2 laser with a wavelength of 10.6 µm (A, *Fig. Box 6.2*; *Fig Box 6.1B* and *C*). The focus of the laser beam can be controlled by a set of Al coated mirrors and ZnSe lenses (A, *Fig. Box 6.2*; *Fig. Box 6.1B* and *C*). A beam integrator lens is used for the stepwise degassing (*Fig. Box 6.1B* and *C*), which generated a 6 mm-squared laser beam at the focal plane.
The stainless steel laser disc with the irradiated samples and fluence monitors are placed into double vacuum UHV sample chamber (*Fig. Box 6.1F and G*). The chamber has a ZnSe viewport window which is transparent to the infra-red 10.6 µm wavelength of the CO_2 laser (A, *Fig. Box 6.2*; *Fig. Box 6.1F* and *G*). During the incorporation of the laser disc into the extraction system, the sample chamber is exposed to normal atmospheric pressure (*Fig. Box 6.1F*). Thus, it has to be baked for one or two days afterwards under continuous pumping in order to re-establish the vacuum (*Fig. Box 6.1F*). A KBr cover slip on the laser disc hinders evaporated or melted sample material to introduce into the vacuum or to condensate at the ZnSe viewport window during the step heating (*Fig. Box 6.1G*). The entire sample chamber is fixed on a X-Y stage, where the individual samples can be moved under the laser beam. A video camera allows the control of the position of the laser disc in both manual and automatic runs.

6.2 Gas cleaning system

As gases other than argon (e.g., N_2, O_2, H_2, H_2O, CO_2, and hydrocarbons) are released during step heating, the argon-gas mixture has to be cleaned up prior to the isotope analyses by a cold finger and a two getter pump system. The cold finger works at -130°C to freeze the H_2O (B, *Fig. Box 6.2*; *Fig. Box 6.1E*). The two subsequently following SAES GP-50 getters pumps, running at 450°C and room temperature, respectively, first crack the hydrocarbon (C; *Fig. Box 6.2*; *Fig. Box 6.1E*) and second remove the hydrogen (D, *Fig. Box 6.2*; *Fig. Box 6.1E*). After the clean-up, the resulting pure argon gas enters the mass spectrometer, which is directly connected with the ultrahigh vacuum extraction line through an automatic valve.

6.3 Nu Instrument Noblesse

Once the argon gas entered the mass spectrometer, it equilibrates for several minutes until the analyses continues (E; *Fig. Box 6.2*). The Nu Instruments Noblesse gas mass spectrometer works in a static mode to analyse the argon isotopes. The ion source is a Nier-type ionization source where a hot filament (tungsten) emit electrons which are accelerated through the ion source chamber towards a trap due to a small potential difference (E, *Fig. Box 6.2*; McDougall and Harrison, 1999). On their way, they collide with the argon gas molecules, leading to a positive ion beam, due to the removal of electrons from the outer shells of the argon atoms (McDougall and Harrison, 1999).
The ion beam passes through a defining slit and several pairs of Z plates which focus and steer the beam, respectively. It is finally accelerated through a flight tube (F, *Fig. Box 6.2*) to the magnet which has an angle of 75° and a radius of 240 mm. Two small, fixed magnets produce the magnetic field to separates the ions according to their masses (G, *Fig. Box 6.2*).
The detector system consists of one Faraday cup on the high mass position for ^{40}Ar and ^{39}Ar and three ETP ion-counting electron multiplier, sitting on axial position for ^{38}Ar and ^{37}Ar, and on low mass for ^{36}Ar, respectively (H, *Fig. Box 6.2*). This detector geometry enables the simultaneous measurements of up to three isotopes. ^{40}Ar, ^{38}Ar, and ^{36}Ar are recorded simultaneously, followed by peak hopping to measure ^{39}Ar and ^{37}Ar, with baseline acquisition following the same sequence. Two quad lenses between the magnet and the detector system and variations in the magnetic field of the magnet let the beam switch between the different masses without moving of the detectors, which finally facilitates the multi-collector analyses of the different isotopes. In order to keep the consistency in the measurements, all runs of samples, blanks, air aliquots and fluence monitors set on automatic are carried out in an identical fashion with the same detector configurations, based on protocols described by Brumm et al. (2010).

6.4 Air pipette system

The gas preparation system is equipped with an air pipette system (I; *Fig. Box 6.2*) to monitor instrumental mass fractionation and for detector intercalibration. In the Quadlab system about $6x10^{-14}$ mol for argon air aliquot is delivered from a two-liter reservoir (J, *Fig. Box 6.2*). The atmospheric $^{40}Ar/^{36}Ar$ ratio of 298.56 ± 0.31 and $^{38}Ar/^{36}Ar$ ratio of 0.1885 ± 0.0003 (Lee et al., 2006) are used to monitor and correct for instrumental mass fractionation and detector bias on a regular basis, where the isotopic composition of the air aliquot is measured and the discrimination is finally calculated in comparison with the atmospheric ratios (McDougall and Harrison, 1999). The air aliquot is measured under the same detector configuration as for the samples, fluence monitors and blanks. Causes for mass discrimination could be drifts in the magnetic field, variable ionization efficiency, and mass dependency of the detector system.

6.5 Data acquisition

Prior to the analyses are set on automatic run, one to three samples are measured manually to observe their gas release. Based on the degassing behaviour, the laser power and duration of gas extraction is programmed appropriately for each step when running automatically.
Each run starts with a blank, typical with values ~$1x10^{-16}$ mol for ^{40}Ar and ~$1x10^{-18}$ mol ^{36}Ar, and several inbetween to identify any argon gas that still remains in the extraction and cleaning line of the instrument from a previous step or any further contamination.
An entire clean-up set of one run, including gas extraction via step heating and cleaning through the cold finger and getter pumps, takes 600 sec, followed by 30 sec equilibration time prior to start the analyses in the mass spectrometer. The measurements are conducted in 14 data-acquisition cycles, including recording of the baseline in each cycle at half a mass unit off the peak. The baseline for the ETP ion-counting electron multiplier is zero. However, due to the usage of a 10^{11} Ω resistor, which amplifies the signals of ^{40}Ar and ^{39}Ar, the baseline of the Faraday cup exhibits the so-called "Johnson noise". Therefore, the signals of ^{40}Ar and ^{39}Ar has to be at least 2mV, respectively, to distinguish it from the Johnson noise.
After the end of the data collection, linear and parabolic fits are implemented to extrapolated the heights of the peaks back to time zero, where the argon is initially introduced into the mass spectrometer. Argon isotopes of the air aliquots are allocated to parabolic fits and of the blanks to linear fits. For the samples and fluence monitors, ^{40}Ar is allocated to parabolic or linear fits, depending on the analysis of each cycle. ^{39}Ar, ^{38}Ar, ^{37}Ar and ^{36}Ar are allocated to linear fits.
Each analysis is blank-corrected either by using the value before this analysis started, or by using the average of all blanks that are measured over a longer term for each mass. The $^{40}Ar/^{36}Ar$ ratio of 298.56 ± 0.31 and $^{38}Ar/^{36}Ar$ = 0.1885 ± 0.0003 (Lee et al., 2006) are used to correct for instrumental mass fractionation and detector bias.
To calculate the J values, first the J value of a fluence monitor, placed on a certain position within the irradiation batch, is calculated by using the weighted mean of the $^{40}Ar^*/^{39}Ar_K$ ratios of each analysis for that given position. Subsequently, the arithmetic mean of the $^{40}Ar^*/^{39}Ar_K$ ratios of each single fluence monitors are taken to calculated the J value that neighbour the surrounding sample positions within the irradiation batch.
All data collection, reduction and age calculation are done by "Mass Spec", written by Al Deino (Berkeley Geochronology Center).

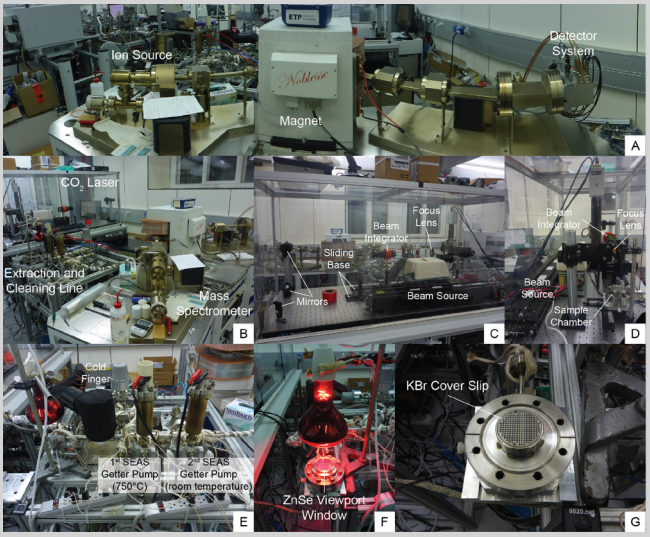

Figure Box 6.1 A) Nu Instruments Noblesse multi-collector noble gas mass spectrometer showing its three main components: left) ion source, centre) magnet, and right) detector system (photo: author of this thesis, 10/01/2018). B) Instrumentation set-up in the Quaternary Dating Laboratory (Quadlab), Natural History Museum of Denmark in Copenhagen, showing the argon extraction line, equipped with a defocused 50-W Synrad CO_2 laser to the left, as well as the fully automated Nu Instruments Noblesse multi-collector noble gas mass spectrometer to the right (photo: author of this thesis, 10/01/2018). C) 50-W Synrad CO_2 laser from the side (photo: author of this thesis, 10/01/2018). D) 50-W Synrad CO_2 laser from the front showing where the sample chamber for the argon extraction is situated (photo: author of this thesis, 10/01/2018). E) Gas cleaning system consisting of a cold finger to freeze the H_2O and two SAES GP-50 getter pumps to remove the hydrocarbons and H_2, respectively (photo: author of this thesis, 10/01/2018). F) Sample chamber with the ZnSe viewport window which transmits the intra-red radiation of the laser beam. The sample chamber is baked under continuous pumping to re-establish the vacuum after the sample loading, where this part of the extraction line is exposed to atmospheric pressure (photo: author of this thesis, 10/01/2018). G) Opened sample chamber during sample loading. This part is exposed to atmospheric pressure. It shows the KBr cover slip right on the copper laser disc. The cover slip prevents that melted or evaporated sample material is introduced into the vacuum or condensate at the ZnSe viewport during the step heating (photo: author of this thesis, 10/01/2018).

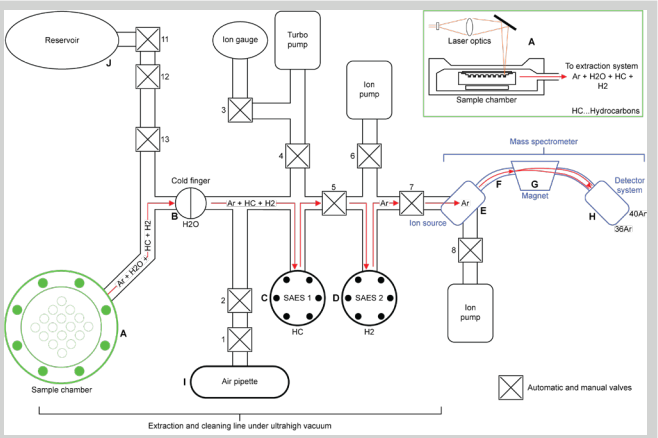

Figure Box 6.2 Schematic illustration of the Nu Instruments Noblesse multi-collector noble gas mass spectrometer as used at the Quaternary Dating Laboratory (Quadlab), Natural History Museum of Denmark in Copenhagen. The bold letter indicate the steps as described in the text.

data and laser-ablation microprobe maps reveal intra-crystalline variations in $^{40}Ar^*$ (Schaen et al., 2020), which are not discussed further. Similar to the U-Pb method, the MSWD enables the evaluation of data sets (see chapter 5.4) presented in age spectra or isochron plots.

6.4.1 Age spectra

Age spectra or $^{40}Ar/^{39}Ar$ release pattern are the most common way to present step heating data, where model ages of each incremental heating step are plotted against the cumulative ^{39}Ar released (e.g., Fig. 6.3A). Assuming an undisturbed isotopic system, the ^{40}Ar and neutron-induced ^{39}Ar have a homogeneous distribution in the sample, where the individual steps of an age spectrum show constant $^{40}Ar/^{39}Ar$ ratios, finally resulting in a plateau (Fig. 6.3A). The age is determined as weighted mean of the steps that define the plateau.

There have been various suggestions by previous authors (e.g., Fleck et al., 1977; Berger and York, 1981; Foland et al., 1986) for criteria that define an $^{40}Ar/^{39}Ar$ age plateau. Most recently Schaen et al. (2020) suggest that an $^{40}Ar/^{39}Ar$ age plateau should: 1) consist of at least five concordant steps that comprise more than 50% of the released ^{39}Ar, 2) concordant steps do not show a slope, i.e., neither an incremental increase or decrease of the apparent ages, and 3) the isochron through all concordant steps reveal an initial $^{40}Ar/^{36}Ar$ ratio close to the atmospheric value at the 95% confidence interval.

The age spectrum plot is suitable to monitor for disturbance of the isotopic system. Partial ^{40}Ar loss results in different $^{40}Ar/^{39}Ar$ ratios and in consequence in so-called stair-cased age spectra during incremental heating (Paper III; Fig. 6.3B). Sites with less Ar retentivity, e.g., altered domains, suffer more ^{40}Ar loss, resulting in low $^{40}Ar/^{39}Ar$ ratios. As argon can diffuse out more easily, those sites release their gas during the first steps in a step heating procedure (Fig. 6.3B). Whilst towards higher steps, the argon is released from more retentive sites, where consequently the $^{40}Ar/^{39}Ar$ ratios are higher and the steps rise to older ages. In summary, the first steps yield the maximum age for the re-heating event, e.g. impact event (Paper III) or hydrothermal activity (Paper II), that caused the isotopic disturbance, whereas the higher steps of an age spectrum represent the minimum for the primary age of a sample (Fig. 6.3B; McDougall and Harrison, 1999).

In an idealized system, all argon trapped in a mineral is radiogenic ($^{40}Ar^*$). However, this is rarely the case as most minerals contain a non-radiogenic argon component and this is typically atmospheric in origin. This assumption is the basis of model K-Ar and $^{40}Ar/^{39}Ar$ age calculations in which the non-radiogenic ^{40}Ar component (determined by measuring ^{36}Ar) is taken as atmospheric in origin. A non-disturbed mineral that has trapped atmospheric argon will yield an age plateau providing air correction has been properly applied. In contrast, the presence of a trapped extraneous argon component (excess and inherited argon; McDougall and Harrison, 1999; Kelley, 2002b) can compromise an $^{40}Ar/^{39}Ar$ age spectrum. For instance, argon, which did not completely diffuse out from the target rock during an impact event, can be still trapped as extraneous argon component in impact melts either within clasts of target material or within the melt matrix (Paper V; Jourdan et al., 2007, 2008, 2012). It can give rise to complex U-shaped age spectra, where the initial high ages fall steeply to younger ages at the intermediates steps and rise again to anomalous old ages at the last degassing steps (Paper V; Fig. 6.3C). In some cases, the minimum at the intermediate steps can approach a meaningful age (Paper V; Fig. 6.3C; McDougall and Harrison, 1999).

The ^{39}Ar recoil effect can result in often hump-shaped age spectra. Due to the displacement of ^{39}Ar from a K-rich phases (e.g., biotite) into a neighbouring K-poor phase (e.g., chlorite) during the fast neutron irradiation, ^{39}Ar is depleted in the K-rich phase. In consequence, some steps

Table 6.2 Summary table of partial and total decay of ^{40}K (Rivera, 2013)

	Steiger and Jäger (1977)	Min et al. (2000)	Renne et al. (2010)	Renne et al. (2011)
λ_ε ($x10^{-10}$/yr)	0.581	0.580±0.007	0.5755±0.0016	0.5757±0.0016
λ_β ($x10^{-10}$/yr)	4.962	4.884±0.049	4.9737±0.0093	4.9548±0.0134
λ_{total} ($x10^{-10}$/yr)	5.543	**5.463±0.054**	5.5492±0.0011	5.5305±0.0015

The decay constant in bold type was used in this thesis to calculate the $^{40}Ar/^{39}Ar$ ages.

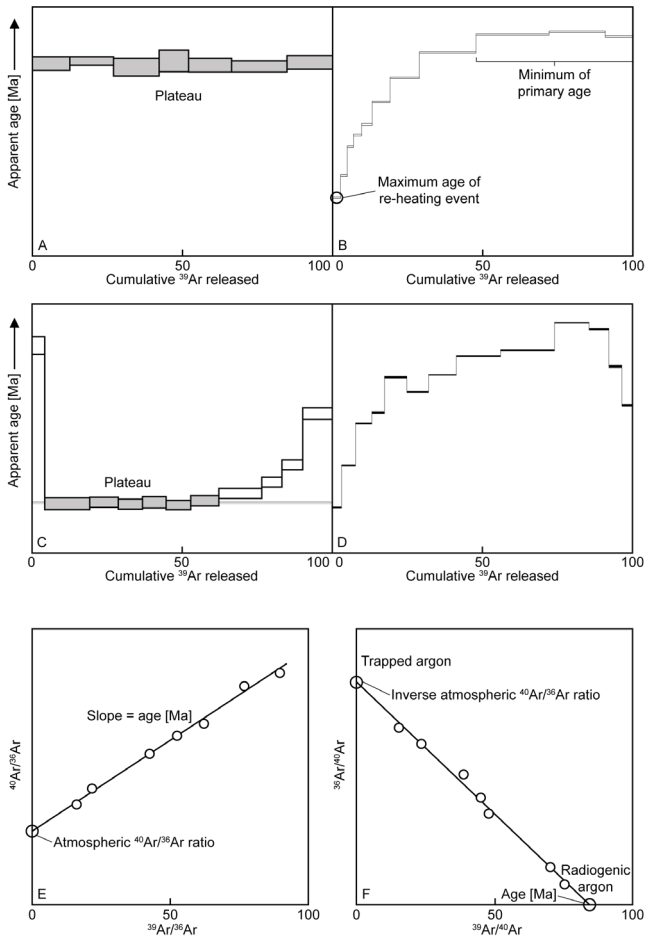

Figure 6.3 A) An example of an age spectrum showing steps with constant $^{40}Ar/^{39}Ar$ ratios and thus, are concordant and form a plateau from which the weighted mean age is finally calculated. Flat age spectrum indicate that isotopic system is undisturbed since the moment of closing. B) Stair-cased age spectra (HUM 15-02-3 from Hummeln impact structure, Sweden, see Paper III) indicating disturbed isotopic system, where the apparent age of the first steps yield the maximum age of the thermal event that induced the opening of the isotopic system, whereas towards increasing steps the apparent ages reflect the minimum of the primary age of the sample (McDougall and Harrison, 1999). C) U-shaped age spectrum (Sample 1251A from Puchezh-Katunki impact structure, Russia, see Paper V) indicating the presence of an extraneous argon component. In this case the steps at the minimum yield a weighted mean plateau age = 192.07 ± 0.64 Ma. D) Humped-shaped age spectrum with steps older than the primary age of the sample (Sample 58-1 from Siljan impact structure, Sweden, with two step ages ~2.0 Ga above the crystallization age of ~1.9-1.7 Ga; see Paper II) indicating that ^{39}Ar recoil, in this case from biotite to chlorite, might have occurred during the neutron irradiation. E) An example of an isochron plot with ^{36}Ar as reference isotope for ^{39}Ar (x-axis) and ^{40}Ar (y-axis). The slope of the positive regression line yields the age and its intercept with the y-axis the initial $^{40}Ar/^{36}Ar$ ratio. F) An example of an inverse isochron with ^{40}Ar as reference isotope for ^{39}Ar (x-axis) and ^{36}Ar (y-axis). The x-intercept of the negative regression line gives the age as inverse of $^{40}Ar/^{39}Ar$ and the y-intercept the inverse initial $^{40}Ar/^{36}Ar$ ratio. The regression line represents the mixing between two argon reservoirs, where the lower end reflects the radiogenic argon and the upper one the trapped argon component with an atmospheric composition of $^{40}Ar/^{36}Ar$ = 298.56 ± 0.31 (Lee et al., 2006).

increase to anomalous old ages (Paper II; Fig. 6.3D; Lo and Onstott, 1989; Di Vincenzo et al., 2003).

6.4.2 Isochron plots

In order to determine the initial argon composition, an isochron plot is rather a better approach (McDougall and Harrison, 1999). In a normal isochron plot, ^{40}Ar and ^{39}Ar are standardized against ^{36}Ar. The slope of a positive, linear correlation yields the age and the intercept with the y-axis the initial isotopic $^{40}Ar/^{36}Ar$ composition (Fig. 6.3E; Heizler and Harrison, 1988; McDougall and Harrison, 1999). However, measurements of ^{36}Ar, which makes 0.3364±0.0006% (McDougall and Harrison, 1999) of the total argon, are not very precisely and can lead to erroneous analyses. Thus, errors, then occurring on both axes, can yield a false linear correlation (McDougall and Harrison, 1999).

Instead ^{40}Ar can be used as reference isotope for ^{36}Ar and ^{39}Ar, such as in inverse isochron plots. Due to its major abundance in argon, ^{40}Ar (99.6%; McDougall and Harrison, 1999) can be measured with a higher precision, leading to small and often negligible errors. An inverse isochron has a negative regression line, where the x-intercept gives the age (inverse $^{40}Ar/^{39}Ar$ ratio) and the y-intercept the inverse of initial isotopic $^{40}Ar/^{36}Ar$ composition (Fig. 6.3F). A robust linear fit, indicated by the MSWD, represents the mixing line between two different argon sources, commonly suggested between radiogenic and trapped argon, where the trapped component is atmospheric in composition und thus, should have a terrestrial $^{40}Ar/^{36}Ar$ ratio of about 298.56 ± 0.31 (Lee et al., 2006). Analyses near the x-axis are assigned to the radiogenic component and near the y-axis contain trapped argon (Fig. 6.3F; Roddick, 1978; Heizler and Harrison, 1988; McDougall and Harrison, 1999). Atmospheric ratios above 298 indicate the presence of extraneous argon (McDougall and Harrison, 1999; Kelley, 2002b), which can compromise the linear regression of an isochron plot. Extraneous argon let rise the ^{40}Ar concentration above that actually produced by the in-situ ^{40}K decay (Kelley, 2002b), leading to too old ages, sometimes even older than the Earth (McDougall and Harrison, 1999).

7. Dating of impact events

Impact cratering is an instantaneous event with extreme P-T conditions affecting the target rocks and minerals profoundly. One would think that the isotopic systems

should be affected in the same fashion and thus should allow for the determination of precise impact ages. Isotopic dating of impact events is commonly applied to lithologies that experienced a complete melting during an impact event, such as impact melt rocks from coherent melt sheets, tektites, spherules, melt-bearing (suevitic), and pseudotachylitic breccias as well as minerals phases newly formed within such melts (Deutsch and Schärer, 1994; Jourdan, 2012; Jourdan et al. 2009, 2012). During an event, shock pressures of more than 100 GPa near the point of impact lead to complete melting of the target rock (Fig. 7). Passing outward, lower shock pressures of 60 GPa still induce rock melting and at shock pressure between 40 and 60 GPa selective melting of individual mineral phases still occurs (French and Koeberl, 2010). Due to the deposit of post-shock waste heat in the target rock during the shock wave passage, the temperature can rise to 2000°C and more (Stöffler, 1971; French, 1998; French and Koeberl, 2010). It exceeds the closure temperatures of the different isotopic systems which means that radiogenic daughter isotopes leave the isotopic systems through diffusion. In the best case this leads to a complete reset of an isotopic system (Fig. 7). Soon after the impact event, the molten target material is recrystallised which prevent newly formed daughter isotopes from escaping. Thus, the recrystallisation of the molten material as well as new crystallised mineral phases within these melts start a new isotopic clock, where the new parent/daughter isotope ratios reflect the time elapsed since the impact event (Fig. 7). However, several drawbacks can compromise this approach and make dating of impact events a challenging task. For instance, impact melts can still preserve an inherited daughter isotope component (pre-impact daughter isotope component) either in clasts, consisting of target material, or trapped within the melt matrix. Additionally, many impact structures on Earth are deeply eroded and therefore no melt material for dating is available. Furthermore, hydrothermal activity, which commonly follows after an impact event, can overprint an isotopic system in such a way that it does not record the impact event. Materials that experienced different degrees of shock metamorphism can coexist in an impact structure and might even be subjected differently to post-impact heating. In summary, in an impact structure pre, syn and post-impact ages can occur side by side (Deutsch and Schärer, 1994; Jourdan, 2012; Jourdan et al., 2009, 2012; Hauser et al., 2019), which warrants careful interpretation of the age data.

The most frequently utilized isotopic techniques in dating impact events are the U-Pb and $^{40}Ar/^{39}Ar$ methods. Reliable impact ages obtained from the U-Pb dating commonly come from zircon either newly formed (e.g., Hodych and Dunning, 1992; Kamo et al., 1996) or with a recrystallised neoblastic texture (e.g., Krogh et al., 1993; Kamo and Krogh, 1995), both extracted from impact melts. As Pb is incompatible in zircon, all Pb accumulated prior to an impact event will be excluded from the newly formed or recrystallised zircon, leading to a reset of the U-Pb system (Fig. 7). Due to the accumulation of new radiogenic Pb, a new U/Pb ratio will be established which should record the impact event (Fig. 7). Since Krogh et al. (1984) reported the first natural shocked zircon at the Sudbury impact structure in Canada, zircon U-Pb dating has long been used in dating impact events and it was mostly conducted by ID-TIMS (e.g., Hodych and Dunning, 1992; Kamo and Krogh, 1995; Kamo et al., 1996). However, recent advancements in EBSD analyses as well as in in-situ dating, such as SIMS (e.g., Moser et al., 2011; Kenny et al., 2017, 2019; Erickson et al., 2020) allow for textural control. Different zircon shock features (see chapter 3.1), recorded by EBSD, can be linked to different degrees of U-Pb age reset and in the best case yield an impact age. For instance, the EBSD analyses combined with ID-TIMS of shocked zircon from the Vredefort impact structure in South Africa by Moser et al. (2011) have shown that zircon grains with planar and curviplanar fracturing as well as twinning experienced little to no U-Pb reset and still preserve the primary age of the target rock. Recrystallised neoblastic zircon grains from the same study area yield impact-related ages (Moser et al., 2011). Combined EBSD and SIMS analyses of neoblastic zircon from the Sudbury impact structure, Canada, by Kenny et al. (2019) revealed a variable age reset within the non-neoblastic domains, whereas large neoblasts yield a complete reset of the U-Pb system related to the impact event about 1856 Ma ago. Furthermore, EBSD analyses can be used to identify FRIGN zircon (see chapter 3.1), a neoblastic zircon formed due to the reversion of reidite (see chapter 3.1) at temperatures above 1200°C. Previous studies (e.g., Hauser et al., 2019; Kenny et al., 2019) have shown that FRIGN zircon is a suitable candidate to date impact events. In Paper IV, we utilize SIMS U-Pb spot dating and ion imaging analyses combined with EBSD analyses conducted on shocked zircon from impact melts of the Mien impact structure, Sweden. Similar to the results of previous studies, it shows that the different shock features (from partly porous to fully neoblastic-textured zircon grains) can be correlated with a different degree of U-Pb age resetting, where in particular FRIGN zircon grains reveal a complete U-Pb reset related to the impact event about 119 Ma. It is consistent with previous studies giving an impact age of about 122 Ma (Bottomley et al., 1990; Schmieder and Kring, 2020) ago. Ion imaging analyses enable the construction of U-Pb distribution maps with grain-internal age information of individual zircon grains. The highest U concentrations, often accompanied with younger $^{206}Pb/^{238}U$ ages, are observed in the neoblastic and porous domains of the zircon grains. It indicates that radiation-damaged domains served as nucleation sites for neoblasts as suggested by previous studies (e.g., Schmieder et al., 2015; Schwarz et al., 2020). Thus, metamictization likely promoted the recrystallisa-

tion of neoblastic and porous textures during the impact event, which finally led to Pb loss in these zircon grains.
In contrast, U-Pb dating of zircon with shock features such as fracturing, planar features, twinning and reidite that record shock pressures of up to 30 GPa often fail to date an impact event and instead preserve the pre-impact age of the target rock (e.g., Moser et al., 2011; Erickson et al., 2013b). Deutsch and Schärer (1990) and Schärer and Deutsch (1990) have shown that shock pressure alone, even rising up to between 35 and 59 GPa, is often not sufficient to cause significant Pb loss in zircon. U-Pb studies by Moser et al. (2011) revealed that zircon extracted from the target rock from the Vredefort impact structure, South Africa, that recorded a maximum shock pressure of 20 GPa, did not experience any resetting of the U-Pb system. Similar results are obtained by the U-Pb studies in Paper I. Zircon grains from the target rock of the Siljan impact structure, Sweden, are characterized by planar features. According to Timms et al. (2017), such features are formed at P-T conditions of T<900°C and P < 20 GPa. It is consistent with PDF studies on quartz grains by Holm-Alwmark et al. (2018) who determined a maximum shock pressure of about 16 GPa for the highly shocked samples of the target rock near the crater centre in Siljan. It suggests that the P-T conditions were insufficient to cause any resetting of the U-Pb system and thus these zircon grains are not suitable to date the impact event, even though that the lower intercept dates overlap temporally with the impact age about 380 Ma ago (Reimold et al., 2005; Jourdan et al., 2012). Instead, we conclude that the U-Pb data reflects preserved information about the residency times at shallow, cool crustal levels of zircon grains located near and distal to the crater centre. Prior to the impact event, zircon near the crater centre resided deep in the crust at warm conditions. Thus, radiation damage annealed continuously, which inhibited Pb loss until the basement was uplifted to shallower, cooler levels during the impact event. In contrast, zircon distal to the crater centre was located at near-surface conditions, residing near the current erosional surface for at least 1260 Ma. Thus, radiation-damaged domains were not able to anneal and these zircon grains lost Pb to a larger extent than zircon grains near the crater centre.
Dating of impact events by the $^{40}Ar/^{39}Ar$ method is mostly applied to material melted by the impact event, such as impact melt rocks (Swisher et al., 1992; Jourdan et al., 2008), tektites (Schmieder et al., 2018), melt-bearing (suevitic) breccia and pseudotachylitic breccia (Reimold et al., 2005), as well as mineral phases newly grown within these melts (Alwmark et al., 2017). As the T_C of argon diffusion in silicate minerals is relatively low (150-580°C; McDougall and Harrison, 1999; Reiners et al., 2005, and reference therein), the initial temperatures during shock wave passage, that can reach 2000°C and more (Stöffler, 1971; French, 1998; French and Koeberl, 2010), should induce a complete degassing of these types of impactites during an impact event. They quenched soon after it, which means that the $^{40}Ar/^{39}Ar$ data of these melts should closely reflect the age of the impact event. The $^{40}Ar/^{39}Ar$ analyses of whole rock impactites (fine-grained volcanic rocks affected by impact) from the Hummeln impact structure, Sweden and impact melt rocks from the Mien and Puchezh-Katunki impact structures, Sweden and Russia, respectively, in Paper III and Paper V suggest that the acquired data can be related to the respective impact events. The $^{40}Ar/^{39}Ar$ data of samples from the Hummeln impact structure, in Paper III indicate a partial reset of the K-Ar system. The $^{40}Ar/^{39}Ar$ analyses of impact melts from the Mien impact structure in Paper III reveal dates between 120 and 118 Ma, which give a slight younger impact age of about 119 Ma compared to the current impact age of 122 Ma (Bottomley et al., 1990; Schmieder and Kring, 2020). The $^{40}Ar/^{39}Ar$ analyses of impact melts from the Puchezh-Katunki impact structure in Paper V revise the impact event to a much older age than the commonly quoted impact age of about 167 Ma (e.g., Masaitis, 1999; Mashchak, 1999). However, due to the presence of an inherited argon component, that did not completely diffuse out during the impact event and thus, is still trapped in clasts or within the melt matrix, a common drawback in $^{40}Ar/^{39}Ar$ dating of impact events (Jourdan et al., 2012), an age range of 196-192 Ma was chosen instead of a precise impact age.
Unless material is molten, a complete reset of the K-Ar system is difficult to achieve. Experiments with shock pressures of up to 60 GPa on individual mineral phases, such as biotite, amphibole and feldspar, as well as whole rocks do not show severe disturbance of the K-Ar system (Davis, 1977; Jessberger and Ostertag, 1982; Stephan and Jessberger, 1992). These experimental analyses are supported by observations from natural impact events. For instance, at shock pressures between 40 and 45 GPa, the K-Ar system of shocked biotite and amphibole from the Nördlinger Ries impact structure, Germany (Jessberger et al., 1978), showed no response to the impact event. The K-Ar system of shocked biotite and feldspar from the Haughton impact structure, Canada, reveal a partial loss of radiogenic argon. (Stephan and Jessberger, 1992). In general, at P-T conditions of T>1000°C and P>45 GPa the breakdown temperature of both biotite and amphibole will be exceeded leading to a thermal decomposition in to a mixture of magnetite and an amorphous phase (glass) rather than melting (Chao, 1967, 1968; Stöffler, 1972). In this sense, decomposition might induce a redistribution of the K and Ar isotopes which could finally lead to loss of radiogenic argon and thus make the material suitable for dating.
In order to induce argon loss of non-molten, relatively low shocked material, such as clasts of less shocked target rock (<10 GPa; French and Koeberl, 2010), it either must be exposed to elevated temperatures for a prolonged time after the impact (Bogard et al., 1987, 1988; Jessberger

and Ostertag, 1982; Stephan and Jessberger, 1992) or be subjected to alteration processes. In this case, the $^{40}Ar/^{39}Ar$ age data post-date an impact rather than are directly related to the event. Bogard et al. (1988) investigated granitic clasts from the suevitic breccia of the Nördlinger Ries impact structure, Germany, which were shocked to various degrees between 10 and 52 GPa. It shows that clasts affected by shock pressure to at least 20 GPa, but subjected to elevated temperatures after the impact event can reveal clear resetting of the K-Ar system. Bogard et al. (1987, 1988) proposed that the post-impact residency at higher temperatures for a sufficient time causes the major argon loss of material which was not molten during impact. Alteration processes are commonly induced by the circulation of hydrothermal fluids that generally follow an impact event (Osinski and Pierazzo, 2013). Previous studies have shown that such hydrothermal systems can be active between 0.6 and 1.6 million years in medium-sized craters, e.g., for the Lappajärvi impact structure, Finland (Schmieder and Jourdan, 2013), and up to 4-6 million years in large-sized craters such as the Chicxulub impact structure, Mexico (Pickersgill et al., 2019). With temperatures (e.g., Komor et al., 1988; Kirsimäe et al., 2002), that can exceed the closure temperature for argon diffusion in silicate minerals, hydrothermal fluid activity seems sufficient to affect the K-Ar system, as shown in Paper II. Biotite and amphibole from the target rock near and distal to the crater centre of the Siljan impact structure, Sweden, is analysed. The $^{40}Ar/^{39}Ar$ data show that biotite near the crater centre, strongly altered to chlorite, reveal a strong disturbance of the K-Ar system. Whilst the K-Ar systems of biotite less altered and distal to the crater centre is less disturbed. Similar results account for amphibole both near and distal to the crater centre. We conclude that the hydrothermal alteration of biotite to chlorite near the crater centre led to loss of radiogenic argon. In contrast, towards to localities distal to the crater centre the fluid activity was less intense and thus, the K-Ar systems of the less altered biotite and amphibole was not overprinted to the same extent.

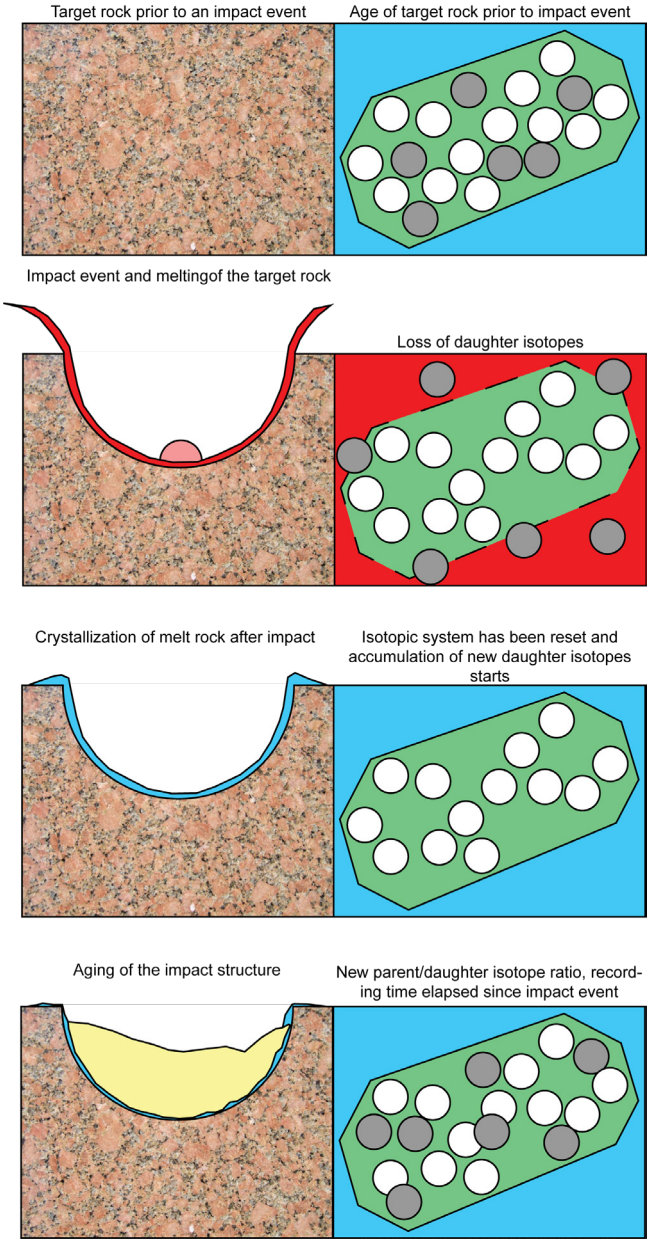

Figure 7 Schematic illustration how an isotopic system is reset in melt rock during an impact event. Right column: in white = parent isotopes and in grey = daughter isotopes.

8. Summary of papers

8.1 Paper I

Herrmann, M., Söderlund, U., Scherstén, A., Næraa, T., Holm-Alwmark, S., and Alwmark, C. The effect of annealing on discordance of U-Pb ages of zircon. Submitted in Scientific Reports.

In this paper, we show that Pb loss and the resulting discordance of U-Pb data of zircon is primarily controlled by the residence time at shallow, "cool" crustal levels rather than linked to a disturbing tectonothermal event. Mezger and Krogstad (1997) hypothesised that diffusional Pb loss occurs only in radiation-damaged zircon residing at shallow, "cool" conditions, below the annealing temperature of 600-650°C. In order to test their hypothesis empirically, we investigated 23 zircon samples by LA-ICP-MS. The samples were taken from the granitoid basement in and around the Siljan impact structure, Sweden (Fig. 8). The rocks were variably affected by different shock pressure

(2-16 GPa; Holm et al., 2011; Holm-Alwmark et al., 2018) during the impact event about 380 Ma ago (Reimold et al., 2005; Jourdan et al., 2012).Our U-Pb data demonstrate that zircon close to the crater centre is significantly less discordant, even down to U concentrations between 200 and 400 ppm U (mean discordance = 3.0 ± 0.4% (1σ) at 200-400 ppm U, mean discordance = 8.3 ± 2.3% (1σ) at 1200-1400 ppm U), than grains from distal localities (mean discordance = 8.5 ± 2.6% (1σ) at 200-400 ppm U, mean discordance = 25.2 ± 4.1% (1σ) at 1200-1400 ppm U). Even though hydrothermal fluids were intensively active near the crater centre (Komor et al., 1988), that could potentially have forced the Pb loss, yet the grains near the crater centre still remain less discordant. We argue that a difference in the residence time at shallow, "cool" crustal levels below the annealing temperature seems a reasonable explanation for the contrasting discordant behaviour of the zircon near and distal to the crater centre. Zircon grains distal to the crater centre have been near the erosional surface >1260 Ma (Söderlund et al., 2006; Lundmark and Lamminen, 2016) and thus, prone to accumulate radiation damage and lose Pb to a larger extent. Whilst zircon near the crater centre resided in greater depth at temperatures sufficient to continuously anneal the radiation damage in kind of alpha recoil and fission tracks until the rock became uplifted due to the impact at ~380 Ma. This model agrees with our data and hence corroborate the hypothesis by Mezger and Krogstad (1997). An estimated uplift of ~8 km (Holm-Alwmark et al., 2017) of the crater centre during the impact, let suggest that the annealing of alpha recoil and fission tracks still proceeds at temperatures as low as ~200-250°C, which is in good agreement with the annealing temperature determined by previous studies (Yamada et al., 1995; Tagami and Shimada, 1996; Tagami et al., 1996).

8.2 Paper II

Herrmann, M., Alwmark, C., and Storey, M. New $^{40}Ar/^{39}Ar$ data on biotite and amphibole from the Siljan impact structure, Sweden – Impact-related or post-impact hydrothermal alteration? Submitted in GSA Special Papers – Proceedings in LMI VI

In this paper, we present $^{40}Ar/^{39}Ar$ data of biotite and amphibole from the Siljan impact structure, Sweden (Fig. 8), in order to see whether the post-impact hydrothermal fluid activity was triggered by the impact event. Previous studies (Johansson and Rickard, 1984; Lindblom and Wickman, 1985; Valley et al., 1988; Komor et al., 1988; AlDahan, 1990; Hode et al., 2003; Drake et al., 2019), indicate that near-surface fluids were likely driven by the impact. Fluid-inclusion analyses on different mineral phases indicate temperatures between 327 and 342°C close to the crater centre, decreasing towards the rim of structure, with 40 to 225°C (Komor et al., 1988; Hode et al., 2003; Drake et al., 2019). Due to the low closure temperature of argon in silicate minerals, the impact-triggered hydrothermal system of Siljan should be seen in the $^{40}Ar/^{39}Ar$ ages (Komor et al., 1988) of biotite (T_C = 280-350°C; Harrison et al., 1985; Grove and Harrison, 1996) and amphibole (T_C = 480-580°C; Harrison, 1981; Dahl, 1996). In total 13 biotite and 6 amphibole samples, separated from whole-rock granite samples taken in and around the Siljan crater, were analysed by $^{40}Ar/^{39}Ar$. Biotite near the crater centre, strongly altered to chlorite, yield strongly disturbed age spectra, where the first (low laser power) step ages (~606-190 Ma) overlap with the Siljan impact event about 379.7 ± 2.0 Ma ago (our recalculation based on decay constant of 5.463 ± 0.214x10^{-10}/yr by Min et al., 2000, and fish canyon sanidine age of 28.201 ± 0.046 Ma by Kuiper et al., 2008). This could indicate an impact relation. However, previous studies (Jessberger et al., 1978; Stephan and Jessberger, 1992; Fel'dman et al., 2006a) have shown that the K-Ar system is highly shock resistant and even at shock pressure up to 45 GPa no significant argon loss can be observed (Stephan and Jessberger, 1992). Maximum shock pressures of the investigated samples are 16 GPa (Holm-Alwmark et al., 2018). Instead, we argue that hydrothermal alteration could explain the disturbances. The alteration temperature of biotite lies between 200 and 340°C (Parry and Downey, 1982; Eggleton and Banfield, 1985), which is in fact in good agreement with the closure temperature of biotite (T_C = 280-350°C). In contrast, biotite distal to the crater centre and amphibole, irrespective from near or distal to the crater centre, show much less alteration, which also can be seen in their less disturbed, near-flat age spectra (~1.6 Ga), close to zircon U-Pb crystallization ages of ~1.9-1.7 Ga (see Paper I). This indicates that the temperature of the hydrothermal fluids near the crater centre were >200 °C sufficient to disturb the K-Ar system of biotite during its chloritization, but too low to affect the amphibole (T_C = 480-580°C). Towards localities distal to the crater centre, the temperature of the hydrothermal fluids seems to drop so far, as no significant disturbance of the K-Ar system can be observed in either biotite or amphibole. This agrees with the trapping temperatures determined on fluid inclusions, where near the crater centre the temperatures lie between 327 and 342°C and thus, overlap with the alteration temperature of biotite (200-340°C). Whilst distal to the crater centre, the fluid inclusions yield temperatures ranging from 40 to 225°C, i.e., too low to induce significant argon loss from biotite.

The overlap of the (low laser power) step ages (~606-190 Ma) with the Siljan impact event (~380 Ma) indicates that the hydrothermal system near the surface in Siljan was impact-triggered.

8.3 Paper III

Herrmann, M., and Storey, M. New $^{40}Ar/^{39}Ar$ dating of the Mien and Hummeln impact structures, Sweden. Manuscript.

The third paper is focused on the $^{40}Ar/^{39}Ar$ analyses of impactites from the Mien and Hummeln impact structures, both located in southern Sweden (Fig. 8), in order to obtain impact-related ages. The impact ages of both craters are either not well-constrained by biostratigraphy (485-470 Ma; Grahn and Nõlvak, 1993; Grahn et al., 1996; Lindström et al., 1999) as for Hummeln, or the age is still debatable as for Mien with a best-estimation of 122.4 ± 2.3 Ma (re-calculated by Schmieder and Kring, 2020). The new $^{40}Ar/^{39}Ar$ analyses, performed in step-heating procedures, were done on several whole rock mm-sized drill cores.
The age spectra of the Mien samples reveal "pseudo-plateau" ages around 120 to 119 Ma, with integrated ages from 118.83 ± 0.08 to 118.02 ± 0.07 Ma and three concordant steps of 119.04 ± 0.08 Ma, consistent with known impact age. However, the smaller uncertainties of the new $^{40}Ar/^{39}Ar$ data, narrow the age-constrain for the time of impact with a tendency to younger ages. Thus, based on our three concordant steps, the impact event is suggested to ~119 Ma. All Hummeln age spectra suffer from disturbance of the K-Ar system, indicative for a partial resetting between 478 and 272 Ma. The older first step ages (477.8 ± 1.0 Ma and 467.6 ± 2.2 Ma) can be chronologically correlated with the biostratigraphic data (485-470 Ma), suggesting a causal link of the partial loss of radiogenic argon with an impact. The disruption of a large L-chondrite parent body at about 470 Ma ago, increased the impact crater formation rate for 10 to 30 Ma following the break-up (Schmitz et al., 2001, 2003). Hummeln, with its temporal overlap of the older first step ages (~478-468 Ma) with the age of the Mid-Ordovician event (485-470 Ma), might belong to the same family of Scandinavian impact structures (e.g., Lockne, Målingen, Tvären) that likely formed as a consequence of this large break-up event. However, as some mineral phases are strongly altered, alteration could be an alternative explanation for the disturbed age spectra. In particular, when K-bearing minerals phases alter, argon is lost (Lo and Onstott, 1989; Que and Allen, 1996). The lower argon retentivity of the altered phases (e.g., chlorite; Hess et al., 1987) force them to degas first during the step-heating analyses. Therefore, the first step ages could also be correlated with the degassing of the altered mineral phases.

8.4 Paper IV

Herrmann, M., Martell, J., Alwmark, C., Kenny, G., and Whitehouse, M. U-Pb systematics of shocked zircon from the Mien impact structure, Sweden: Implications for a new impact age and for metamict-induced zircon texture formation during impact event. Manuscript.

This paper is focused on the investigation of shocked zircon grains from impact melts and suevitic breccia of the Mien impact structure, Sweden (Fig. 8), using SIMS U-Pb spot dating and ion imaging combined with EBSD analyses. The grains display a variety of textures, including pristine-porous, partly porous, completely porous, granular-porous and granular.
The U-Pb spot dating reveals four highly shocked zircon grains that yield seven data points concordant in the lower intercept with an age of 119.7 ± 1.1 Ma. This overlaps with current best-estimate impact age of 122.4 ± 2.3 Ma (Bottomley et al., 1990; Schmieder and Kring, 2020), determined on impact melts by $^{40}Ar/^{39}Ar$. However, as the authors do not explain why they claim it as the best-estimate age for the impact event, together with the fact that their plateaus are not well-defined (Bottomley et al., 1978, 1990), makes the current impact age debatable. Due to a MSWD of 1.04 and a probability of 0.41, the age of this study is more robust and revise the Mien impact event to ~119 Ma. EBSD analyses have shown that the impact age is mainly based on the U-Pb system of FRIGN zircon, which is consistent with other studies (e.g., Hauser et al., 2019). However, one grain, clearly not FRIGN zircon, indicates that even granular-porous zircon with only little mis-orientation can reveal a complete U-Pb reset induced by an impact and thus, a potential candidate to date such events, as well.
Metamictization, the radiation damage of the zircon lattice, enhance the Pb diffusion within zircon (e.g., Nasdala et al., 1998). Previous studies (e.g., Schmieder et al., 2015) speculated that the metamict state of a zircon may promote its alteration into porous and granular texture. In order to prove whether metamictization play a role in their formation, the U-Pb systematics of differently shocked zircon were analysed by ion imaging. This enables the acquisition of U-Pb distribution maps, where for certain regions of interest within a zircon grain the grain-internal ages can be determined. Spot analyses have shown that pristine to partly porous zircon and completely porous, granular-porous to granular zircon build two different populations, revealing contrasting trends of the discordance plotted against the U concentration. In both populations, the highest U concentrations can be observed in the porous and granular domains, indicating that metamictization promoted the formation of both textures during the impact event. Metamict domains are more prone to lose Pb, resulting in younger $^{238}U/^{206}Pb$

ages, as observed in the pristine to partly porous zircon population. The U-rich, porous domains yield younger $^{238}U/^{206}Pb$ ages than the Pb-rich, pristine domains. Hydrothermal fluids, triggered by the Mien impact (Åström, 1996), may have induced the Pb loss from the porous domains. EBSD analyses show no mis-orientation for this zircon population. Thus, recrystallisation into neoblasts as Pb loss process can be excluded. Whilst recrystallisation of neoblasts of complete porous, granular-porous and granular zircon has likely induced the Pb loss, as indicated by EBSD analyses. Recrystallisation can affect more or less an entire zircon grain and thus, leading to generally younger $^{238}U/^{206}Pb$ ages in both U and Pb-rich domains, in particular in fully granular zircon grains with complete U-Pb reset. High U concentrations in their neoblasts indicate on one hand metamictization as a potential nucleation trigger and on the other hand recrystallisation overprinting original magmatic zoning and mobilizing U into neoblasts.

8.5 Paper V

Holm-Alwmark, S., Alwmark, C., Ferriére, L., Lindström, S., Meier, M. M. M., Scherstén, A., Herrmann, M., Masaitis, V. L., Mashchak, M. S., Naumov, M. V., and Jourdan, F. An Early Jurassic age for the Puchezh-Katunki impact structure (Russia) based on $^{40}Ar/^{39}Ar$ data and palynology. Meteoritics and Planetary Science 54:8:1764-1780. DOI: 10.1111/maps.13309.

This paper presents $^{40}Ar/^{39}Ar$ data from step-heating analyses of five impact melt rocks from the Puchezh-Katunki impact structure, Russia (Fig. 8). The data allow us to significantly revise the age range of the crater formation to 196-192 Ma. A new palynological investigation of post-impact sediments, deposited in the crater lake, gives an interval from late Sinemurian to early Pliensbachian (~196-189 Ma; Gradstein et al., 2004) and thus, supports this radiometric age estimate.

Characteristics of the 40-km-in-diameter Puchezh-Katunki crater is an 8-10 km-wide central uplift (Masaitis et al., 1996; Masaitis and Pevzner, 1999), surrounded by an annular depression, which extends laterally between 8-12 km and 25-30 km (Masaitis et al., 1996; Masaitis and Pevzner, 1999). The basement rocks of gneiss and schist are overlain by Proterozoic to Mesozoic sediments of clastics, limestone, carbonates, marl, clays and evaporates (Masaitis et al., 1996; Masaitis and Pevzner, 1999). Previous age studies date the impact event between 203 and 164 Ma, with 167±3 Ma as the commonly quoted impact age (e.g., Masaitis, 1999; Mashchak, 1999).

For the $^{40}Ar/^{39}Ar$ step-heating analyses, five impact melts samples were taken from different depths along the Vorotilovskaya deep drilling hole in the crater centre. For the palynological investigations the sample material comes from the near-surface of the same drilling. Additionally, a previous palynological study (Masaitis and Pevzner, 1999) were re-evaluated. The majority of the $^{40}Ar/^{39}Ar$ analyses, run in two aliquots per sample, yield U-shaped age spectra, indicative for the presence of inherited argon either from incomplete degassed clasts or trapped in the melt matrix during the melting phase of the impact event (Jourdan et al., 2012). One plateau reveals an age of 193.7 ± 1.1 Ma as well as two mini-plateaus have ages of 196.3 ± 0.8 Ma and 192.1 ± 0.6 Ma, where each of them yield additionally two isochron ages of 193.2 ± 2.0 Ma and 190.1 ± 1.3, respectively. The plateau age seems to be a good estimation of the impact age, but the mini-plateau and inverse isochron ages are poorly supportive. Further, the plateau age itself does not reveal a statistically robust inverse isochron, where the $^{40}Ar/^{36}Ar$ ratio of the trapped argon component could be determined. Thus, at the best it can be only tested for the presence of inherited argon. Therefore, only a conservative approach for the impact age is possible with an age range between 196 and 192 Ma, which is currently the best estimation for Puchezh-Katunki crater. It is supported by the palynological analyses. The new investigations and re-evaluation of previous data Masaitis and Pevzner, 1999) reveal an age interval from late Sinemurian to early Pliensbachian (~196-189 Ma; Gradstein et al., 2004) for the impact event.

Figure 8. Map of Europe showing the localities of the impact structures investigated in this thesis.

Table 8.1 Author contributions

	Paper I	Paper II	Paper III	Paper IV	Paper V
Study design	M. Herrmann, C. Alwmark, U. Söderlund, A. Scherstén	M. Herrmann, C. Alwmark	M. Herrmann, C. Alwmark	M. Herrmann	S. Holm-Alwmark
Manuscript writing	M. Herrmann*, C. Alwmark, U. Söderlund*, A. Scherstén*, T. Næraa, S. Holm-Alwmark	M. Herrmann*, C. Alwmark*, M. Storey*	M. Herrmann*, M. Storey*	M. Herrmann*, J. Martell, C. Alwmark, G. Kenny, M. Whitehouse	S. Holm-Alwmark*, C. Alwmark, L. Ferriére, S. Lindström, M. M. M. Meier, A. Scherstén, M. Herrmann, V. L. Masaitis M. S. Mashchak, M. V. Naumov, F. Jourdan
Manuscript illustrations	M. Herrmann	M. Herrmann	M. Herrmann	M. Herrmann	-
Sampling	S. Holm-Alwmark	S. Holm-Alwmark	-	J. Martell	-
Petrography	M. Herrmann	M. Herrmann	M. Herrmann	N.A.	-
SEM	M. Herrmann, C. Alwmark	N.A.	N.A.	M. Herrmann	N.A.
EBSD	N. A.	N.A.	N.A.	M. Herrmann, J. Martell	N.A.
LA-ICP-MS					
- sample preparation	M. Herrmann, T. Næraa	N.A.	N.A.	N.A.	N.A.
- analysis	M. Herrmann, T. Næraa	N.A.	N.A.	N.A.	N.A.
- data reduction	M. Herrmann, T. Næraa	N.A.	N.A.	N.A.	N.A.
- data interpretation	M. Herrmann, C. Alwmark, U. Söderlund, A. Scherstén	N.A.	N.A.	N.A.	N.A.
SIMS					
- sample preparation	N.A.	N.A.	N.A.	M. Herrmann, J. Martell, K. Lindén	N.A.
- U-Pb spot analysis	N.A.	N.A.	N.A.	M. Herrmann, H. Jeon, M. Whitehouse	N.A.
- data reduction (spot analysis)	N.A.	N.A.	N.A.	H. Jeon, M. Whitehouse	N.A.
-ion imaging	N.A.	N.A.	N.A.	M. Herrmann, H. Jeon, M. Whitehouse	N.A.
- data reduction (ion imaging)	N.A.	N.A.	N.A.	M. Herrmann, M. Whitehouse	N.A.
- data interpretation	N.A.	N.A.	N.A.	M. Herrmann	N.A.

Table 8.1 (**continued**) Author contributions

$^{40}Ar/^{39}Ar$					
- sample preparation	N.A.	M. Herrmann, D. Wielandt, M. Storey	M. Herrmann, D. Wielandt, M. Storey	N.A.	-
- analysis	N.A.	M. Herrmann, M. Storey	M. Herrmann, M. Storey	N.A.	-
- data reduction	N.A.	M. Herrmann	M. Herrmann	N.A.	-
- data interpretation	N.A.	M. Herrmann, C. Alwmark, M. Storey	M. Herrmann, M. Storey	N.A.	-

* = Main contributors

N.A. = Not applicable

- = The author of this thesis has not performed the specific activity.

9. What is dated so far and what does the future brings?

According to Schmieder and Kring (2020), there are currently 200 confirmed impact structures on Earth. There are numerous techniques that can be used to characterize an impact structure. However, its age determination is still not routinely included during the documentation process of an impact structure. Thus, many of them are not well-dated or even the age is unknown. Figure 9A shows the number of the current dated craters in [%] in comparison to the numbers [%]. Marked in orange shows the own study based on ages available from the current literature, which is compared with the study by Jourdan et al. (2009), marked in blue. As done in Jourdan et al. (2009), craters with age ranges as well as ages mentioned either vaguely, with a maximum, or with a minimum value, are considered as not constrained. Thus, 81 (41% of the total) of the 200 terrestrial craters are here considered not dated (Fig. 9A). Whilst the remaining 119 craters (60% of the total) are constrained by radiometric dating, (bio-) stratigraphy, fission track dating, cosmogenic nuclides, optical stimulated and thermoluminescence, as well as historical records. Thirty craters (15% of the total) have been dated with a precision better than 10%, 15 craters (8% of the total) with a precision between 10 and 5%, 19 craters (10% of the total) with a precision between 5 and 2%, 18 craters (9% of the total) with a precision between 2 and 1%, and 37 craters (19% of the total) with a precision better than 1% (Fig. 9A). Since Jourdan et al. (2009), the number of dated impact structures increased from 88 (51% of the total) to 119 craters (60% of the total) with a tendency of more craters (this study: 55 craters = 28% of the total; Jourdan et al. (2009): 25 crater = 14% of the total) yielding ages with a precision better than 2% (Fig. 9A), and also with a bias of younger craters (Fig. 9B). It is a trend in the right direction, but still the vast majority of impact structures is not well-constrained or not even dated. The improvement of the database of precisely determined impact ages is crucial in order to understand to what extent impact events drive environmental changes and correlate them with biological crises in the Earth's record as well as with regard to future global catastrophes, based on the estimation of impact flux rate through time.

Up until now, the Chicxulub impact structure, Mexico, is the only crater where the radiometric age (66.07 ± 0.37 Ma; Swisher et al., 1992; Jourdan et al., 2012) can be correlated with the K-Pg mass extinction about 66 Ma ago (Alvarez et al., 1980; Bohor et al., 1987). However, other craters and events were considered, too. Kunk et al. (1989) determined an $^{40}Ar/^{39}Ar$ age of 65.7 ± 1.0 Ma for the Manson impact structure, USA and thus, overlapping temporally with the K-Pg boundary (66.043 ± 0.011 Ma; Renne et al., 2013), too. However, Izett et al. (1998) revised the age to 73.8 ± 0.3 Ma. The 65.82 ± 0.74 Ma-old (Kelley and Gurov, 2002; Meier and Holm-Alwmark, 2017) Boltysh impact structure, Ukraine, with its 24 km in diameter is too small to cause a global catastrophe. The huge eruptions (>1.3 million km3; Schoene et al., 2015) of the flood basalts of the Deccan traps are seen as an alternative explanation for the K-Pg mass extinction. The volcanic activity lasted several million years and peaked about 65.5 Ma ago (e.g., Basu et al., 1993; Hofmann et al., 2000; Widdowson et al., 2000). The above-mentioned example shows how constant updating of the impact ages and their precise refinements enable a better correlation

between different events and even exclude some as in the case of the Manson impact structure.

A similar example is given by the Siljan impact structure, Sweden, regarding whether it is linked to the Late Devonian mass extinction at the Frasnian-Famennian boundary, which affected mostly shallow marine species of the tropical and subtropical environment (e.g., Buggisch, 1991). Previous age determinations (e.g., 361.9 ± 1.1 Ma; Bottomley et al., 1978; 343 ± 4 Ma and 349 ± 3 Ma; Åberg et al., 1989; 368.0 ± 1.1 Ma; Bottomley et al., 1990; 377 ± 2 Ma; Reimold et al., 2005) show a continuously revising of the impact age. The current impact age of 380.9 ± 4.6 Ma (Reimold et al., 2005; Jourdan et al., 2012) suggests a connection to the Frasnian-Famennian boundary, which was considered at 374.5 ± 2.6 Ma or 376.1 ± 1.6 Ma according to Gradstein et al. (2004) and Kaufmann et al. (2004), respectively. However, recent U-Pb zircon studies by Percival et al. (2018) revised the Frasnian-Famennian boundary to 372.36 ± 0.053 Ma, which do not overlap with the Siljan impact age. Thus, for now Siljan as cause for the Late Devonian mass extinction seems not under debate anymore. Instead, other theories, such as sea-level fluctuations (e.g., Joachimski and Buggisch, 1993) or massive volcanic eruptions (e.g., Rampino et al., 2019), are considered for the mass extinction in the Late Devonian. However, the current Siljan impact age of 380.9 ± 4.6 Ma (Reimold et al., 2005; Jourdan et al., 2012) is based on a single best-estimation of the least altered sample material (Reimold et al., 2005), which give new attempts to date Siljan by other techniques in order to get a better age. The U-Pb analyses of zircon have shown that the impact event had not effect on the isotopic system (see Paper I), suggesting the temperature conditions were insufficient to trigger any Pb loss. As the Siljan impact structure is deeply eroded (about 4 km since the crater formation; Holm-Alwmark et al., 2017) and almost no melt material is preserved, an alternative approach could be U-Th/He dating on zircon, apatite, and titanite. In all three mineral phases, this isotopic system has a T_C below 220°C (Reiners et al., 2005, and references therein), implying that a potential heat effect from the impact event could be recorded. Previous studies on the Wetumpka impact structure, USA (Wartho et al., 2012), the Manicouagan impact structure, Canada (Biren et al., 2014), the Morokweng and Vredefort impact structures, South Africa (Wielicki et al., 2014), and Clearwater West and Clearwater East impact structures, Canada (Biren et al., 2016) have shown that the U-Th/He system yields reliable impact-related ages and thus, it offers an alternative way of dating impact events when a structure is deeply eroded and impact melts are missing.

Switching focus to the impact cratering rate through time, the impact dating record reveal that some impact events occurred frequently and cluster around certain time periods. If defining that a cluster is built up by at least three craters with ages that overlap in the 2σ uncertainty and have a precision better than 2%, three clusters can be recognized Figure 9C; the Late-Ordovician (~455 Ma), and two in the Early Cretaceous (~142 Ma and ~123 Ma) (based on the chronostratigraphic chart by Cohen et al., 2013). Whilst other age clusters (3 Ma, 15 Ma, 36 Ma, 48 Ma, 66 Ma, 74 Ma, 94 Ma, 168 Ma, 201 Ma, 215 Ma, 228 Ma, and 252 Ma) cannot be recognized when compared with previous studies (Osinski and Pierazzo, 2013; Rampino and Caldeira, 2015, 2017, 2018; Rampino et al., 2019; Meier and Holm-Alwmark, 2017; Fig. 9C). However, these studies also included ages with uncertainties worse than 2% and accounted already two craters as a cluster. For instance, the cluster at 66 Ma, consisting of two impact structures (Chicxulub and Boltysh), is excluded according the above-mentioned criteria. The Gusev impact structure, Russia, with 63.5 ± 0.54 Ma (Movshovic et al., 1991) plots close but does not show an 2σ overlap. Rampino and Caldeira (2017, 2018) and Rampino et al. (2019) claim that some crater cluster (36 Ma, 66 Ma, 145 Ma, 168 Ma, and 215 Ma) can be correlated with mass extinctions. Further, Rampino and Caldeira (2015, 2017) and Rampino et al. (2019) used such cluster to determine a probability distribution of the cratering rate over the last 260 Ma and concluded that an impact event occurs in a periodicity of about 26 Ma. However, Meier and Holm-Alwmark (2017) questioned this claim, concluding that no evidence for a periodicity can be seen in the current impact age record. As the majority of impact structures do not have a well-constrained age, I agree with Meier and Holm-Alwmark (2017). Thus, more work is needed to obtain better precise ages and in order to see a potential periodicity for the impact cratering rate through time and use it to make estimations for future events.

Nevertheless, the clustering of some impact events seems real, where the crater formation rate was raised drastically for a short time period (Meier and Holm-Alwmark, 2017). The Late-Ordovician cluster is the most robust one where, due to the break-up of a large parental L-chondrite body (radius > 50 km; Haack et al., 1996) about 470 Ma ago, the flux of extraterrestrial material was enhanced about two orders of magnitude than today for 10-30 Ma (Schmitz et al., 2001, 2003). Many impact structures on the Baltic Shield are seen as the result of this event, for example the Lockne impact structure, Sweden. Others, however, are still under debate, such as the Hummeln impact structure, Sweden. The $^{40}Ar/^{39}Ar$ dating on impactites of Paper III are promising, but are not a grounded proof that Hummeln belongs to the family of impact structures that are formed as a consequence of the large break-up event. In order to do additional age determinations and find dateable material, in the best case melt material or shocked zircon which also can be used for U-Th/He dating, a drilling campaign into the Hummeln structure has to be considered in the future as discussed in Alwmark et al. (2015).

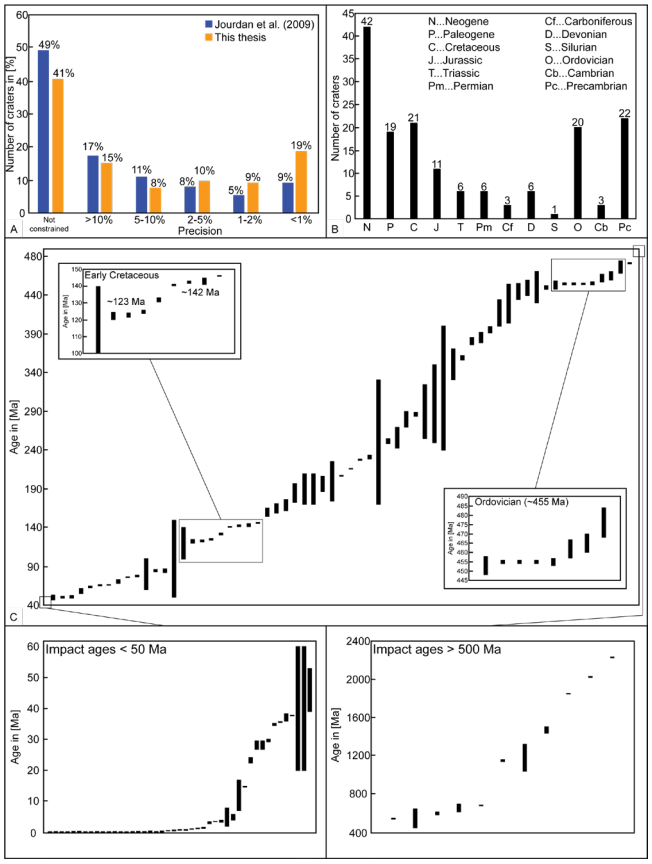

Figure 9 A) Current number of dated and non-dated impact structures in [%] (orange, own study) in comparison to the numbers compiled in Jourdan et al. (2009) (blue) vs the precision in the case for age-constrained craters. The value at each column represents the percentage of craters that are included in each column. A precision of >10% means below than 10% and <1% means better than 1%. B) The amount of craters in each time period, showing a predominant bias to younger craters, but also an increased number of impact structures during the Ordovician and Precambrian time. The value at each column represents the total number of craters included in each column. C) Plot of all ages between 500 and 50 Ma, constrained by radiometric dating, (bio-)stratigraphy, fission track dating, cosmogenic nuclides, optical stimulated and thermoluminescence. There are four cluster (recognizable as "plateaus" consisting of at least three impact ages that overlap in 2σ uncertainty and each of them has a precision better than 2%) during the Ordovician (~461 Ma) and Late Cretaceous (~142 Ma and ~123 Ma), where impact events occurred frequently and increased the crater formation rate for a short time period. The left and the right inset at the bottom include the ages < 50 Ma and > 500 Ma, respectively. Some "plateaus", such as at about <0.008 Ma and 3 Ma in the left as well as at about 555 Ma in the right inset, let suggest a clustering of impact events. However, most of the ages have a precision below 2% and/or have no overlap in the 2σ uncertainty.

References

Åberg, G., Collini, B., and Schmitz, B., 1989, K-Ar isotope analyses from the Siljan Ring meteorite impact structure, Sweden: Geologiska Föreningen i Stockholm Förhandlingar, v. 111, no. 4, p. 355-360.

AlDahan, A. A., 1990, Alteration and mass transfer in cataclasites and mylonites in 6.6 km of granitic crust at the Siljan impact structure, central Sweden: Contributions to Mineralogy and Petrology, v. 105, no. 6, p. 662-676.

Aldrich, L. T., and Nier, A. O., 1948, Argon 40 in Potassium Minerals: Physical Review, v. 74, no. 8, p. 876-877.

Alvarez, L. W., Alvarez, W., Asaro, F., and Michel, H. V., 1980, Extraterrestrial cause for the Cretaceous-Tertiary extinction: Science, v. 208, no. 4448, p. 1095-1108.

Alwmark, C., Bleeker, W., LeCheminant, A., Page, L., and Scherstén, A., 2017, An Early Ordovician 40Ar-39Ar age for the 50 km Carswell impact structure, Canada: GSA Bulletin, v. 129, no. 11-12, p. 1442-1449.

Alwmark, C., Ferriere, L., Holm-Alwmark, S., Ormö, J., Leroux, H., and Sturkell, E., 2015, Impact origin for the Hummeln structure (Sweden) and its link to the Ordovician disruption of the L chondrite parent body: Geology, v. 43, no. 4, p. 279-282.

Andersen, T., 2002, Correction of common lead in U–Pb analyses that do not report 204Pb: Chemical geology, v. 192, no. 1-2, p. 59-79.

Artemieva, N. A., and Shuvalov, V. V., 2016, From Tunguska to Chelyabinsk via Jupiter: Annual Review of Earth and Planetary Sciences, v. 44, p. 37-56.

Aston, F. W., 1921, XLIX. The mass spectra of the alkali metals: The London, Edinburgh, and Dublin Philosophical Magazine and Journal of Science, v. 42, no. 249, p. 436-441.

Åström, K., 1996, Geophysical signature of the Lake Mien meteorite crater, southern Sweden: GFF, v. 118, no. S4, p. 92-93.

Badash, L., 1968, Rutherford, Boltwood, and the Age of the Earth: The Origin of Radioactive Dating Techniques: Proceedings of the American Philosophical Society, v. 112, no. 3, p. 157-169.

Basu, A. R., Renne, P. R., DasGupta, D. K., Teichmann, F., and Poreda, R. J., 1993, Early and late alkali

igneous pulses and a high-3He plume origin for the Deccan flood basalts: Science, v. 261, no. 5123, p. 902-906.

Beckman, V., Möller, C., Söderlund, U., and Andersson, J., 2017, Zircon growth during progressive recrystallization of gabbro to garnet amphibolite, Eastern Segment, Sveconorwegian orogen: Journal of Petrology, v. 58, no. 1, p. 167-187.

Berger, G. W., and York, D., 1981, Geothermometry from 40Ar39Ar dating experiments: Geochimica et Cosmochimica Acta, v. 45, no. 6, p. 795-811.

Biren, M., van Soest, M., Wartho, J.-A., Hodges, K., and Spray, J., 2016, Diachroneity of the Clearwater West and Clearwater East impact structures indicated by the (U–Th)/He dating method: Earth and Planetary Science Letters, v. 453, p. 56-66.

Biren, M. B., Van Soest, M., Wartho, J.-A., and Spray, J. G., 2014, Dating the cooling of exhumed central uplifts of impact structures by the (U–Th)/He method: a case study at Manicouagan: Chemical Geology, v. 377, p. 56-71.

Black, L. P., Kamo, S. L., Allen, C. M., Davis, D. W., Aleinikoff, J. N., Valley, J. W., Mundil, R., Campbell, I. H., Korsch, R. J., and Williams, I. S., 2004, Improved 206Pb/238U microprobe geochronology by the monitoring of a trace-element-related matrix effect; SHRIMP, ID–TIMS, ELA–ICP–MS and oxygen isotope documentation for a series of zircon standards: Chemical Geology, v. 205, no. 1-2, p. 115-140.

Bogard, D., Hörz, F., and Johnson, P., 1987, Shock effects and argon loss in samples of the leedey l6 chondrite experimentally shocked to 29–70 GPa pressures: Geochimica et Cosmochimica Acta, v. 51, no. 7, p. 2035-2044.

Bogard, D., Hörz, F., and Stöffler, D., 1988, Loss of radiogenic argon from shocked granitic clasts in suevite deposits from the Ries Crater: Geochimica et Cosmochimica Acta, v. 52, no. 11, p. 2639-2649.

Bohor, B. F., Betterton, W. J., and Krogh, T. E., 1993, Impact-shocked zircons: discovery of shock-induced textures reflecting increasing degrees of shock metamorphism: Earth and Planetary Science Letters, v. 119, no. 3, p. 419-424.

Bohor, B. F., Modreski, P. J., and Foord, E. E., 1987, Shocked quartz in the Cretaceous-Tertiary boundary clays: Evidence for a global distribution: Science, v. 236, no. 4802, p. 705-709.

Bottomley, R. J., York, D., and Grieve, R. A. F., 1978, 40Ar-39Ar ages of scandinavian impact structures: I Mien and Siljan: Contributions to Mineralogy and Petrology, v. 68, no. 1, p. 79-84.

-, 1990, Argon-40-argon-39 Dating of Impact Craters: Lunar and Planetary Science Conference, p. 421-431.

Brumm, A., Jensen, G. M., van den Bergh, G. D., Morwood, M. J., Kurniawan, I., Aziz, F., and Storey, M., 2010, Hominins on Flores, Indonesia, by one million years ago: Nature, v. 464, no. 7289, p. 748.

Buggisch, W., 1991, The global Frasnian-Famennian» Kellwasser Event «: Geologische Rundschau, v. 80, no. 1, p. 49-72.

Cavosie, A. J., Timms, N. E., Ferrière, L., and Rochette, P., 2018, FRIGN zircon—The only terrestrial mineral diagnostic of high-pressure and high-temperature shock deformation: Geology, v. 46, no. 10, p. 891-894.

Chao, E. C. T., 1968, Pressure and temperature histories of impact metamorphosed rocks—based on petrographic observations: Shock metamorphism of natural materials, p. 135-158.

Chao, E. C. T., 1967, Shock Effects in Certain Rock-Forming Minerals: Science, v. 156, no. 3772, p. 192-202.

Cherniak, D. J., Lanford, W. A., and Ryerson, F. J., 1991, Lead diffusion in apatite and zircon using ion implantation and Rutherford backscattering techniques: Geochimica et Cosmochimica Acta, v. 55, no. 6, p. 1663-1673.

Cherniak, D. J., and Watson, E. B., 2000, Pb diffusion in zircon: Chemical Geology, v. 172, no. 1-2, p. 5-24.

-, 2003, Diffusion in zircon: Reviews in mineralogy and geochemistry, v. 53, no. 1, p. 113-143.

Cohen, K. M., Finney, S. C., Gibbard, P. L., and Fan, J.-X., 2013, The ICS international chronostratigraphic chart: Episodes, v. 36, no. 3, p. 199-204.

Cox, M. A., Cavosie, A. J., Bland, P. A., Miljković, K., and Wingate, M. T., 2018, Microstructural dynamics of central uplifts: Reidite offset by zircon twins at the Woodleigh impact structure, Australia: Geology, v. 46, no. 11, p. 983-986.

Dahl, P. S., 1996, The effects of composition on retentivity of argon and oxygen in hornblende and related amphiboles: A field-tested empirical model: Geochimica et Cosmochimica Acta, v. 60, no. 19, p. 3687-3700.

Davis, D. W., Krogh, T. E., and Williams, I. S., 2003, Historical development of zircon geochronology: Reviews in mineralogy and geochemistry, v. 53, no. 1, p. 145-181.

Davis, P. K., 1977, Effects of shock pressure on 40Ar -39Ar radiometric age determinations: Geochimica et Cosmochimica Acta, v. 41, no. 2, p. 195-205.

Davy, H., 1808, I. The Bakerian Lecture, on some new

phenomena of chemical changes produced by electricity, particularly the decomposition of the fixed Alkalies, and the exhibition of the new substances which constitute their bases; and on the general nature of alkaline bodies: Philosophical Transactions of the Royal Society of London, no. 98, p. 1-44.

Dempster, T., and Chung, P., 2013, Metamorphic zircon: tracking fluid pathways and the implications for the preservation of detrital zircon: Journal of the Geological Society, v. 170, no. 4, p. 631-639.

Deutsch, A., and Schärer, U., 1990, Isotope systematics and shock-wave metamorphism: I. U-Pb in zircon, titanite and monazite, shocked experimentally up to 59 GPa: Geochimica et Cosmochimica Acta, v. 54, no. 12, p. 3427-3434.

-, 1994, Dating terrestrial impact events: Meteoritics, v. 29, p. 301-322.

Di Vincenzo, G., Viti, C., and Rocchi, S., 2003, The effect of chlorite interlayering on 40Ar–39Ar biotite dating: an 40Ar–39Ar laser-probe and TEM investigations of variably chloritised biotites: Contributions to Mineralogy and Petrology, v. 145, no. 6, p. 643-658.

Dodson, M. H., 1973, Closure temperature in cooling geochronological and petrological systems: Contributions to Mineralogy and Petrology, v. 40, no. 3, p. 259-274.

Drake, H., Roberts, N. M., Heim, C., Whitehouse, M. J., Siljeström, S., Kooijman, E., Broman, C., Ivarsson, M., and Åström, M. E., 2019, Timing and origin of natural gas accumulation in the Siljan impact structure, Sweden: Nature communications, v. 10, no. 1, p. 1-14.

EAG labs, SIMS tutorial, 2020, https://www.eag.com/resources/tutorials/sims-tutorial-theory/

Eggleton, R. A., and Banfield, J. F., 1985, The alteration of granitic biotite to chlorite: American Mineralogist, v. 70, no. 9-10, p. 902-910.

Erickson, T. M., Cavosie, A. J., Moser, D. E., Barker, I. R., and Radovan, H. A., 2013a, Correlating planar microstructures in shocked zircon from the Vredefort Dome at multiple scales: Crystallographic modeling, external and internal imaging, and EBSD structural analysis: American Mineralogist, v. 98, no. 1, p. 53-65.

Erickson, T. M., Cavosie, A. J., Moser, D. E., Barker, I. R., Radovan, H. A., and Wooden, J., 2013b, Identification and provenance determination of distally transported, Vredefort-derived shocked minerals in the Vaal River, South Africa using SEM and SHRIMP-RG techniques: Geochimica et Cosmochimica Acta, v. 107, p. 170-188.

Erickson, T. M., Kirkland, C. L., Timms, N. E., Cavosie, A. J., and Davison, T. M., 2020, Precise radiometric age establishes Yarrabubba, Western Australia, as Earth's oldest recognised meteorite impact structure: Nature Communications, v. 11, no. 1, p. 1-8.

Erickson, T. M., Pearce, M. A., Reddy, S. M., Timms, N. E., Cavosie, A. J., Bourdet, J., Rickard, W. D., and Nemchin, A. A., 2017, Microstructural constraints on the mechanisms of the transformation to reidite in naturally shocked zircon: Contributions to Mineralogy and Petrology, v. 172, no. 1, p. 6.

Ewing, R. C., Chakoumakos, B. C., Lumpkin, G. R., and Murakami, T., 1987, The metamict state: MRS Bulletin, v. 12, no. 4, p. 58-66.

Ewing, R. C., Meldrum, A., Wang, L., Weber, W. J., and Corrales, L. R., 2003, Radiation effects in zircon: Reviews in Mineralogy and Geochemistry, v. 53, no. 1, p. 387-425.

Farnan, I., Balan, E., Pickard, C. J., and Mauri, F., 2003, The effect of radiation damage on local structure in the crystalline fraction of ZrSiO4: Investigating the 29Si NMR response to pressure in zircon and reidite: American Mineralogist, v. 88, no. 11-12, p. 1663-1667.

Faure, G., and Mensing, T. M., 2005, Isotopes - Principles and applications, 3rd Edition, Hoboken, New Jersey, John Wiley & Sons, p. 897.

Fel'dman, V. I., Sazonova, L. V., Milyavskii, V. V., Borodina, T. I., Sokolov, S. N., and Zhuk, A. Z., 2006a, Shock metamorphism of some rock-forming minerals: Izvestiya, Physics of the Solid Earth, v. 42, no. 6, p. 477-480.

Fel'dman, V. I., Sazonova, L. V., and Kozlov, E. A., 2006b, Shock metamorphism of some rock-forming minerals: Experimental results and natural observations: Petrology, v. 14, no. 6, p. 540-566.

Fleck, R. J., Sutter, J. F., and Elliot, D. H., 1977, Interpretation of discordant 40Ar/39Ar age-spectra of Mesozoic tholeiites from Antarctica: Geochimica et Cosmochimica Acta, v. 41, no. 1, p. 15-32.

Flude, S., Haschke, M., and Storey, M., 2017, Application of benchtop micro-XRF to geological materials: Mineralogical Magazine, v. 81, no. 4, p. 923-948.

Foland, K., Gilbert, L. A., Sebring, C. A., and Jiang-Feng, C., 1986, 40Ar/39Ar ages for plutons of the Monteregian Hills, Quebec: Evidence for a single episode of Cretaceous magmatism: Geological Society of America Bulletin, v. 97, no. 8, p. 966-974.

French, B. M., 1998, Traces of catastrophe: A handbook of shock-metamorphic effects in terrestrial meteorite impact structures, LPI Contribution.

French, B. M., and Koeberl, C., 2010, The convincing

identification of terrestrial meteorite impact structures: What works, what doesn't, and why: Earth-Science Reviews, v. 98, no. 1, p. 123-170.

Garner, E., Murphy, T. J., Gramlich, J., Paulsen, P., and Barnes, I., 1975, Absolute isotopic abundance ratios and the atomic weight of a reference sample of potassium: Journal of Research of the National Bureau of Standards. Section A, Physics and Chemistry, v. 79, no. 6, p. 713.

Gasperini, L., Alvisi, F., Biasini, G., Bonatti, E., Longo, G., Pipan, M., Ravaioli, M., and Serra, R., 2007, A possible impact crater for the 1908 Tunguska Event: Terra Nova, v. 19, no. 4, p. 245-251.

Geisler, T., Pidgeon, R. T., Kurtz, R., van Bronswijk, W., and Schleicher, H., 2003, Experimental hydrothermal alteration of partially metamict zircon: American Mineralogist, v. 88, no. 10, p. 1496-1513.

Geisler, T., Pidgeon, R. T., van Bronswijk, W., and Kurtz, R., 2002, Transport of uranium, thorium, and lead in metamict zircon under low-temperature hydrothermal conditions: Chemical Geology, v. 191, no. 1, p. 141-154.

Geisler, T., Schaltegger, U., and Tomaschek, F., 2007, Re-equilibration of zircon in aqueous fluids and melts: Elements, v. 3, no. 1, p. 43-50.

Geisler, T., Ulonska, M., Schleicher, H., Pidgeon, R. T., and van Bronswijk, W., 2001, Leaching and differential recrystallization of metamict zircon under experimental hydrothermal conditions: Contributions to Mineralogy and Petrology, v. 141, no. 1, p. 53-65.

Glass, B. P., and Liu, S., 2001, Discovery of high-pressure ZrSiO4 polymorph in naturally occurring shock-metamorphosed zircons: Geology, v. 29, no. 4, p. 371-373.

Gradstein, F. M., Ogg, J. G., Smith, A., Bleeker, W., and Lourens, L. J., 2004, A new geologic time scale, with special reference to Precambrian and Neogene: Episodes, v. 27, no. 2, p. 83-100.

Grahn, Y., and Nõlvak, J., 1993, Chitinozoan dating of Ordovician impact events in Sweden and Estonia. A preliminary note: Geologiska Föreningen i Stockholm Förhandlingar, v. 115, no. 3, p. 263-264.

Grahn, Y., Nõlvak, J., and Paris, F., 1996, Precise chitinozoan dating of Ordovician impact events in Baltoscandia: Journal of Micropalaeontology, v. 15, no. 1, p. 21-35.

Grieve, R., and Masaitis, V., 1994, The economic potential of terrestrial impact craters: International Geology Review, v. 36, no. 2, p. 105-151.

Grieve, R. A. F., 2005, Economic natural resource deposits at terrestrial impact structures: Geological Society, London, Special Publications, v. 248, no. 1, p. 1-29. Grove, M., and Harrison, T. M., 1996, 40Ar* diffusion in Fe-rich biotite: American Mineralogist, v. 81, no. 7-8, p. 940-951.

Gualtieri, A., Norby, P., Hanson, J., and Hriljac, J., 1996, Rietveld refinement using synchrotron X-ray powder diffraction data collected in transmission geometry using an imaging-plate detector: application to standard m-ZrO2: Journal of Applied Crystallography, v. 29, no. 6, p. 707-713.

Haack, H., Farinella, P., Scott, E. R. D., and Keil, K., 1996, Meteoritic, asteroidal, and theoretical constraints on the 500 Ma disruption of the L chondrite parent body: Icarus, v. 119, no. 1, p. 182-191.

Harrison, T. M., 1981, Diffusion of 40 Ar in hornblende: Contributions to Mineralogy and Petrology, v. 78, no. 3, p. 324-331.

Harrison, T. M., Duncan, I., and McDougall, I., 1985, Diffusion of 40Ar in biotite: Temperature, pressure and compositional effects: Geochimica et Cosmochimica Acta, v. 49, no. 11, p. 2461-2468.

Hasebe, N., Mori, S., Tagami, T., and Matsui, R., 2003, Geological partial annealing zone of zircon fission-track system: additional constrains from the deep drilling MITI-Nishikubiki and MITI-Mishima: Chemical Geology, v. 199, no. 1-2, p. 45-52.

Hauser, N., Reimold, W. U., Cavosie, A. J., Crósta, A. P., Schwarz, W. H., Trieloff, M., Da Silva Maia de Souza, C., Pereira, L. A., Rodrigues, E. N., and Brown, M., 2019, Linking shock textures revealed by BSE, CL, and EBSD with U-Pb data (LA-ICP-MS and SIMS) from zircon from the Araguainha impact structure, Brazil: Meteoritics & Planetary Science, v. 54, no. 10, p. 2286-2311.

Hay, D. C., and Dempster, T. J., 2009, Zircon behaviour during low-temperature metamorphism: Journal of Petrology, v. 50, no. 4, p. 571-589.

Hazen, R. M., and Finger, L. W., 1979, Crystal structure and compressibility of zircon at high pressure: American Mineralogist, v. 64, no. 1-2, p. 196-201.

Hearty, P. J., Karner, D. B., Renne, P. R., Olson, S. L., and Fletcher, S., 2005, 40Ar/39Ar age of a young rejuvenation basalt flow: implications for the duration of volcanism and the timing of carbonate platform development during the Quaternary on Kaua'i, Hawaiian Islands: New Zealand Journal of Geology and Geophysics, v. 48, no. 2, p. 199-211.

Heizler, M. T., and Harrison, T. M., 1988, Multiple trapped argon isotope components revealed by 40AR39AR isochron analysis: Geochimica et Cosmochimica Acta, v. 52, no. 5, p. 1295-1303.

Hess, J., Lippolt, H., and Wirth, R., 1987, Interpretation of 40Ar39Ar biotites: Evidence from hydrothermal

degassing experiments and TEM studies: Chemical Geology: Isotope Geoscience section, v. 66, no. 1-2, p. 137-149.

Hode, T., von Dalwigk, I., and Broman, C., 2003, A Hydrothermal System Associated with the Siljan Impact Structure, Sweden—Implications for the Search for Fossil Life on Mars: Astrobiology, v. 3, no. 2, p. 271-289.

Hodych, J. P., and Dunning, G. R., 1992, Did the Manicouagan impact trigger end-of-Triassic mass extinction?: Geology, v. 20, no. 1, p. 51-54.

Hofmann, C., Feraud, G., and Courtillot, V., 2000, 40Ar/39Ar dating of mineral separates and whole rocks from the Western Ghats lava pile: further constraints on duration and age of the Deccan traps: Earth and Planetary Science Letters, v. 180, no. 1-2, p. 13-27.

Holm-Alwmark, S., Rae, A. S. P., Ferriere, L., Alwmark, C., and Collins, G. S., 2017, Combining shock barometry with numerical modeling: Insights into complex crater formation—The example of the Siljan impact structure (Sweden): Meteoritics & Planetary Science, p. 1-29.

Holm-Alwmark, S., Ferrière, L., Alwmark, C., and Poelchau, M., 2018, Estimating average shock pressures recorded by impactite samples based on universal stage investigations of planar deformation features in quartz—Sources of error and recommendations: Meteoritics & Planetary Science, v. 53, no. 1, p. 110-130.

Holm, S., Alwmark, C., Alvarez, W., and Schmitz, B., 2011, Shock barometry of the Siljan impact structure, Sweden: Meteoritics & Planetary Science, v. 46, no. 12, p. 1888-1909.

Hölzl, S., Hofmann, A., Todt, W., and Köhler, H., 1994, U-Pb geochronology of the Sri Lankan basement: Precambrian Research, v. 66, no. 1-4, p. 123-149.

Huneke, J. C., and Smith, S. P., 1976, The realities of recoil: 39 Ar recoil out of small grains and anomalous age patterns in 40 Ar-39 Ar dating: Proceedings of the Lunar and Planetary Science Conference, p. 1987-2008.

Ireland, T. R., and Williams, I. S., 2003, Considerations in zircon geochronology by SIMS: Reviews in mineralogy and geochemistry, v. 53, no. 1, p. 215-241.

Izett, G. A., Cobban, W. A., Dalrymple, B. G., and Obradovich, J. D., 1998, 40Ar/39Ar age of the Manson impact structure, Iowa, and correlative impact ejecta in the Crow Creek Member of the Pierre Shale (Upper Cretaceous), South Dakota and Nebraska: GSA Bulletin, v. 110, no. 3, p. 361-376.

Jackson, S. E., Pearson, N. J., Griffin, W. L., and Belousova, E. A., 2004, The application of laser ablation-inductively coupled plasma-mass spectrometry to in situ U–Pb zircon geochronology: Chemical Geology, v. 211, no. 1-2, p. 47-69.

Jessberger, E., Staudacher, T., Dominik, B., Kirsten, T., and Schaeffer, O., 1978, Limited response of the K–Ar system to the Nordlinger Ries giant meteorite impact: Nature, v. 271, no. 5643, p. 338-339.

Jessberger, E. K., and Ostertag, R., 1982, Shock-effects on the K-Ar system of plagioclase feldspar and the age of anorthosite inclusions from North-Eastern Minnesota: Geochimica et Cosmochimica Acta, v. 46, no. 8, p. 1465-1471.

Joachimski, M. M., and Buggisch, W., 1993, Anoxic events in the late Frasnian—Causes of the Frasnian-Famennian faunal crisis?: Geology, v. 21, no. 8, p. 675-678.

Johansson, Å., and Rickard, D., 1984, Isotopic composition of phanerozoic ore leads from the Swedish segment of the Fennoscandian Shield: Mineralium Deposita, v. 19, no. 4, p. 249-255.

Joo, S., and Liang, H., 2013, Secondary Ion Mass Spectroscopy (SIMS), in Wang, Q. J., and Chung, Y.-W., eds., Encyclopedia of Tribology: Boston, MA, Springer US, p. 2989-2994.

Jourdan, F., 2012, The 40Ar/39Ar dating technique applied to planetary sciences and terrestrial impacts: Australian Journal of Earth Sciences, v. 59, no. 2, p. 199-224.

Jourdan, F., Reimold, W. U., and Deutsch, A., 2012, Dating terrestrial impact structures: Elements, v. 8, no. 1, p. 49-53.

Jourdan, F., Renne, P. R., and Reimold, W. U., 2007, The problem of inherited 40Ar* in dating impact glass by the 40Ar/39Ar method: Evidence from the Tswaing impact crater (South Africa): Geochimica et Cosmochimica Acta, v. 71, no. 5, p. 1214-1231.

-, 2008, High-precision 40Ar/39Ar age of the Jänisjärvi impact structure (Russia): Earth and Planetary Science Letters, v. 265, no. 3-4, p. 438-449.

-, 2009, An appraisal of the ages of terrestrial impact structures: Earth and Planetary Science Letters, v. 286, no. 1, p. 1-13.

Kaiser, A., Lobert, M., and Telle, R., 2008, Thermal stability of zircon (ZrSiO4): Journal of the European Ceramic Society, v. 28, no. 11, p. 2199-2211.

Kamo, S. L., and Krogh, T. E., 1995, Chicxulub crater source for shocked zircon crystals from the Cretaceous-Tertiary boundary layer, Saskatchewan: Evidence from new U-Pb data: Geology, v. 23, no. 3, p. 281-284.

Kamo, S. L., Reimold, W. U., Krogh, T. E., and

Colliston, W. P., 1996, A 2.023 Ga age for the Vredefort impact event and a first report of shock metamorphosed zircons in pseudotachylitic breccias and Granophyre: Earth and Planetary Science Letters, v. 144, no. 3, p. 369-387.

Kaufmann, B., Trapp, E., and Mezger, K., 2004, The numerical age of the upper Frasnian (Upper Devonian) Kellwasser horizons: A new U-Pb zircon date from Steinbruch Schmidt (Kellerwald, Germany): The Journal of Geology, v. 112, no. 4, p. 495-501.

Kelley, S., 2002a, K-Ar and Ar-Ar dating: Reviews in Mineralogy and Geochemistry, v. 47, no. 1, p. 785-818.

Kelley, S., 2002b, Excess argon in K–Ar and Ar–Ar geochronology: Chemical Geology, v. 188, no. 1, p. 1-22.

Kelley, S. P., and Gurov, E., 2002, Boltysh, another end-Cretaceous impact: Meteoritics & Planetary Science, v. 37, no. 8, p. 1031-1043.

Kenny, G. G., Morales, L. F., Whitehouse, M. J., Petrus, J. A., and Kamber, B. S., 2017, The formation of large neoblasts in shocked zircon and their utility in dating impacts: Geology, v. 45, no. 11, p. 1003-1006.

Kenny, G. G., Schmieder, M., Whitehouse, M. J., Nemchin, A. A., Morales, L. F. G., Buchner, E., Bellucci, J. J., and Snape, J. F., 2019, A new U-Pb age for shock-recrystallised zircon from the Lappajärvi impact crater, Finland, and implications for the accurate dating of impact events: Geochimica et Cosmochimica Acta.

Kirsimäe, K., Suuroja, S., Kirs, J., Kärki, A., Polikarpus, M., Puura, V., and Suuroja, K., 2002, Hornblende alteration and fluid inclusions in Kärdla impact crater, Estonia: Evidence for impact-induced hydrothermal activity: Meteoritics & Planetary Science, v. 37, no. 3, p. 449-457.

Klemperer, O., 1935, On the radioactivity of potassium and rubidium: Proceedings of the Royal Society of London. Series A-Mathematical and Physical Sciences, v. 148, no. 865, p. 638-648.

Koeberl, C., 1993, Chicxulub crater, Yucatan: tektites, impact glasses, and the geochemistry of target rocks and breccias: Geology, v. 21, no. 3, p. 211-214.

Komor, S. C., Valley, J. W., and Brown, P. E., 1988, Fluid-inclusion evidence for impact heating at the Siljan Ring, Sweden: Geology, v. 16, no. 8, p. 711-715.

Košler, J., 2008, Laser ablation sampling strategies for concentration and isotope ratio analyses by ICP-MS, Laser ablation ICP-MS in the Earth sciences: current practices and outstanding issues, Volume 40, Centre for Geobiology and Department of Earth Science Bergen, p. 79-92.

Krogh, T., Davis, D., Corfu, F., and Pye, E., 1984, Precise U-Pb zircon and baddeleyite ages for the Sudbury area, The geology and ore deposits of the Sudbury structure, Volume 1, Ontario Geological Survey Toronto, p. 431-446.

Krogh, T. E., Kamo, S. L., Sharpton, V. L., Marin, L. E., and Hildebrands, A. R., 1993, U–Pb ages of single shocked zircons linking distal K/T ejecta to the Chicxulub crater: Nature, v. 366, p. 731.

Kuiper, K., Deino, A., Hilgen, F., Krijgsman, W., Renne, P., and Wijbrans, J., 2008, Synchronizing rock clocks of Earth history: science, v. 320, no. 5875, p. 500-504.

Kunk, M. J., Izett, G. A., Haugerud, R. A., and Sutter, J. F., 1989, 40Ar-39Ar Dating of the Manson Impact Structure: A Cretaceous-Tertiary Boundary Crater Candidate: Science, v. 244, no. 4912, p. 1565-1568.

Kusaba, K., Syono, Y., Kikuchi, M., and Fukuoka, K., 1985, Shock behavior of zircon: Phase transition to scheelite structure and decomposition: Earth and Planetary Science Letters, v. 72, no. 4, p. 433-439.

Lee, J.-Y., Marti, K., Severinghaus, J. P., Kawamura, K., Yoo, H.-S., Lee, J. B., and Kim, J. S., 2006, A redetermination of the isotopic abundances of atmospheric Ar: Geochimica et Cosmochimica Acta, v. 70, no. 17, p. 4507-4512.

Lee, J. K., Williams, I. S., and Ellis, D. J., 1997, Pb, U and Th diffusion in natural zircon: Nature, v. 390, no. 6656, p. 159-162.

Leroux, H., Reimold, W. U., Koeberl, C., Hornemann, U., and Doukhan, J. C., 1999, Experimental shock deformation in zircon: a transmission electron microscopic study: Earth and Planetary Science Letters, v. 169, no. 3, p. 291-301.

Lindblom, S., and Wickman, F. E., 1985, Fluid inclusions in quartz from a quartz breccia in the Siljan Ring structure, central Sweden: Geologiska Föreningen i Stockholm Förhandlingar, v. 107, no. 1, p. 53-58.

Lindström, M., Flodén, T., Grahn, Y., Hagenfeldt, S., Ormö, J., Sturkell, E. F. F., and Törnborg, R., 1999, The Lower Palaeozoic of the probable impact crater of Hummeln, Sweden: Geologiska Föreningen i Stockholm Förhandlingar, v. 121, no. 3, p. 243-252.

Lo, C.-H., and Onstott, T. C., 1989, 39Ar recoil artifacts in chloritized biotite: Geochimica et Cosmochimica Acta, v. 53, p. 2697-2711.

Longo, G., 2007, The Tunguska event, in Bobrowsky, P., and Rickman, H., eds., Comet/asteroid impacts and human society: Berlin, Heidelberg, Springer, p. 303-330.

Ludwig, K. R., 2012, Users's Manual for Isoplot 3.75 - A Geochronological Toolkit for Microsoft Excel: Berkeley Geochronological Center Special Publications, v. 5.

Lundmark, A. M., and Lamminen, J., 2016, The provenance and setting of the Mesoproterozoic Dala Sandstone, western Sweden, and paleogeographic implications for southwestern Fennoscandia: Precambrian Research, v. 275, p. 197-208.

Martell, J., 2018, Shock metamorphic features in zircon grains from the Mien impact structure: clues to conditions during impact, Master thesis, Lund University, p. 80.

Masaitis, V., Mashchak, M., and Naumov, M., 1996, The Puchezh-Katunki astrobleme: A structural model of a giant impact crater: SoSyR, v. 30, no. 1, p. 3.

Masaitis, V., and Pevzner, L., 1999, Deep drilling in the Puchezh-Katunki impact structure: VSEGEI-Press, St. Petersburg.

Masaitis, V. L., 1999, Impact structures of northeastern Eurasia: The territories of Russia and adjacent countries: Meteoritics & Planetary Science, v. 34, no. 5, p. 691-711.

Mashchak, M. S., 1999, Dating of the impact event, in Masaitis, V. L., and Pevzner, L. A., eds., Deep drilling in the Puchezh-Katunki impact structure: Saint Petersburg, VSEGEI-Press, p. 242-244.

McDougall, I., and Harrison, T. M., 1999, Geochronology and Thermochronology by the 40Ar/39Ar Method, 2nd Edition, New York, Oxford University Press on Demand, p. 269.

McGregor, M., McFarlane, C. R., and Spray, J. G., 2019, In situ multiphase U–Pb geochronology and shock analysis of apatite, titanite and zircon from the Lac La Moinerie impact structure, Canada: Contributions to Mineralogy and Petrology, v. 174, no. 7, p. 62.

Meier, M. M., and Holm-Alwmark, S., 2017, A tale of clusters: no resolvable periodicity in the terrestrial impact cratering record: Monthly Notices of the Royal Astronomical Society, v. 467, no. 3, p. 2545-2551.

Meldrum, A., Boatner, L., Weber, W., and Ewing, R., 1998, Radiation damage in zircon and monazite: Geochimica et Cosmochimica Acta, v. 62, no. 14, p. 2509-2520.

Meredith, R. W., Janečka, J. E., Gatesy, J., Ryder, O. A., Fisher, C. A., Teeling, E. C., Goodbla, A., Eizirik, E., Simão, T. L., and Stadler, T., 2011, Impacts of the Cretaceous Terrestrial Revolution and KPg extinction on mammal diversification: science, v. 334, no. 6055, p. 521-524.

Merrihue, C., 1965, Trace-element determinations and potassium-argon dating by mass spectroscopy of neutron-irradiated samples: Trans Am Geophys Union, v. 46, p. 125.

Merrihue, C., and Turner, G., 1966, Potassium-Argon Dating by Activation with Fast Neutrons: Journal of Geophysical Research, v. 71, no. 11, p. 2852-2857.

Mezger, K., and Krogstad, E. J., 1997, Interpretation of discordant U-Pb zircon ages: An evaluation: Journal of metamorphic Geology, v. 15, p. 127-140.

Min, K., Mundil, R., Renne, P. R., and Ludwig, K. R., 2000, A test for systematic errors in 40Ar/39Ar geochronology through comparison with U/Pb analysis of a 1.1-Ga rhyolite: Geochimica et Cosmochimica Acta, v. 64, no. 1, p. 73-98.

Mitchell, J., 1968, The argon-40argon-39 method for potassium-argon age determination: Geochimica et Cosmochimica Acta, v. 32, no. 7, p. 781-790.

Morozova, I., 2015, Strength study of zircon under high pressure, Master thesis: The University of Western Ontario, p. 125.

Moser, D. E., Flowers, R. M., Bowman, J. R., Wooden, J., and Hart, J. R., 2011, New zircon shock phenomena and their use for dating and reconstruction of large impact structures revealed by electron nanobeam (EBSD, CL, EDS) and isotopic U–Pb and (U–Th)/He analysis of the Vredefort dome: Canadian Journal of Earth Sciences, v. 48, p. 117-139.

Movshovic, Y. V., Milyavsk, A. Y., and Titova, G., 1991, Geology of the northeastern margin of Donets ridge and dating of the Kamensk and Gusev impact craters: International Geology Review, v. 33, no. 7, p. 623-635.

Nasdala, L., Pidgeon, R., Wolf, D., and Irmer, G., 1998, Metamictization and U-Pb isotopic discordance in single zircons: a combined Raman microprobe and SHRIMP ion probe study: Mineralogy and Petrology, v. 62, no. 1-2, p. 1-27.

Nasdala, L., Wenzel, M., Vavra, G., Irmer, G., Wenzel, T., and Kober, B., 2001, Metamictisation of natural zircon: accumulation versus thermal annealing of radioactivity-induced damage: Contributions to Mineralogy and Petrology, v. 141, no. 2, p. 125-144.

Newman, F., and Walke, H., 1935, LX. The radioactivity of potassium and rubidium: The London, Edinburgh, and Dublin Philosophical Magazine and Journal of Science, v. 19, no. 128, p. 767-773.

Nier, A. O., 1935, Evidence for the existence of an isotope of potassium of mass 40: Physical Review, v. 48, no. 3, p. 283.

Onstott, T. C., Miller, M. L., Ewing, R. C., Arnold, G. W., and Walsh, D. S., 1995, Recoil refinements:

Implications for the 40Ar/39Ar dating technique: Geochimica et Cosmochimica Acta, v. 59, no. 9, p. 1821-1834.

Osinski, G. R., and Pierazzo, E., 2013, Impact cratering: Processes and products, Chichester, West Sussex, John Wiley and Sons, Impact Cratering, p. 316 p.

Parry, W., and Downey, L., 1982, Geochemistry of hydrothermal chlorite replacing igneous biotite: Clays and Clay Minerals, v. 30, no. 2, p. 81-90.

Paton, C., Hellstrom, J., Paul, B., Woodhead, J., and Hergt, J., 2011, Iolite: Freeware for the visualisation and processing of mass spectrometric data: Journal of Analytical Atomic Spectrometry, v. 26, no. 12, p. 2508-2518.

Patterson, C., 1956, Age of meteorites and the earth: Geochimica et Cosmochimica Acta, v. 10, no. 4, p. 230-237.

Percival, L. M., Davies, J. H., Schaltegger, U., De Vleeschouwer, D., Da Silva, A.-C., and Föllmi, K. B., 2018, Precisely dating the Frasnian–Famennian boundary: implications for the cause of the Late Devonian mass extinction: Scientific reports, v. 8, no. 1, p. 1-10.

Petrus, J. A., and Kamber, B. S., 2012, VizualAge: A novel approach to laser ablation ICP-MS U-Pb geochronology data reduction: Geostandards and Geoanalytical Research, v. 36, no. 3, p. 247-270.

Pickersgill, A., Christou, E., Mark, D., Lee, M., Tremblay, M., Rasmussen, C., Morgan, J., Gulick, S., Schmieder, M., and Bach, W., 2019, Six Million Years of Hydrothermal Activity at Chicxulub?, LPI-Co, Volume 2136, p. 5082.

Pickersgill, A., Osinski, G. R., and Flemming, R. L., 2015, Shock effects in plagioclase feldspar from the Mistastin Lake impact structure, Canada: Meteoritics and Planetary Science, v. 50, no. 9, p. 1546-1561.

Pidgeon, R. T., Neil, J. R., and Silver, L. T., 1966, Uranium and Lead Isotopic Stability in a Metamict Zircon under Experimental Hydrothermal Conditions: Science, v. 154, no. 3756, p. 1538-1540.

Popova, O. P., Jenniskens, P., Emel'yanenko, V., Kartashova, A., Biryukov, E., Khaibrakhmanov, S., Shuvalov, V., Rybnov, Y., Dudorov, A., and Grokhovsky, V. I., 2013, Chelyabinsk airburst, damage assessment, meteorite recovery, and characterization: Science, v. 342, no. 6162, p. 1069-1073.

Press, F., and Siever, R., 2003, Allgemeine Geologie - Einfuehrung in das System Erde, Muenchen, Elsevier GmbH, Spektrum Akademischer Verlag.

Que, M., and Allen, A. R., 1996, Sericitization of plagioclase in the Rosses granite complex, Co. Donegal, Ireland, De Gruyter.

Rampino, M. R., and Caldeira, K., 2015, Periodic impact cratering and extinction events over the last 260 million years: Monthly Notices of the Royal Astronomical Society, v. 454, no. 4, p. 3480-3484.

-, 2017, Correlation of the largest craters, stratigraphic impact signatures, and extinction events over the past 250 Myr: Geoscience Frontiers, v. 8, no. 6, p. 1241-1245.

-, 2018, Comparison of the ages of large-body impacts, flood-basalt eruptions, ocean-anoxic events and extinctions over the last 260 million years: a statistical study: International Journal of Earth Sciences, v. 107, no. 2, p. 601-606.

Rampino, M. R., Caldeira, K., and Prokoph, A., 2019, What causes mass extinctions? Large asteroid/comet impacts, flood-basalt volcanism, and ocean anoxia—Correlations and cycles: Koeberl, C., and Bice, DM, eds, v. 250, p. 271-302.

Rayleigh, L., and Ramsay, W., 1895, Argon, a new constituent of the atmosphere: Philosophical Transactions of the Royal Society of London. A, v. 186, p. 187-241.

Reddy, S. M., Johnson, T. E., Fischer, S., Rickard, W. D. A., and Taylor, R. J. M., 2015, Precambrian reidite discovered in shocked zircon from the Stac Fada impactite, Scotland: Geology, v. 43, no. 10, p. 899-902.

Reid, A., and Ringwood, A., 1969, Newly observed high pressure transformations in Mn3O4, CaAl2O4, and ZrSiO4: Earth and Planetary Science Letters, v. 6, no. 3, p. 205-208.

Reimold, W. U., Kelley, S. P., Sherlock, S. C., Henkel, H., and Koeberl, C., 2005, Laser argon dating of melt breccias from the Siljan impact structure, Sweden: Implications for a possible relationship to Late Devonian extinction events: Meteoritics & Planetary Science, v. 40, no. 4, p. 591-607.

Reimold, W. U., Leroux, H., and Gibson, R. L., 2002, Shocked and thermally metamorphosed zircon from the Vredefort impact structure, South Africa a transmission electron microscopic study: European Journal of Mineralogy, v. 14, no. 5, p. 859-868.

Reiners, P. W., Ehlers, T. A., and Zeitler, P. K., 2005, Past, Present, and Future of Thermochronology: Reviews in Mineralogy and Geochemistry, v. 58, no. 1, p. 1-18.

Renne, P. R., Balco, G., Ludwig, K. R., Mundil, R., and Min, K., 2011, Response to the comment by WH Schwarz et al. on "Joint determination of 40K decay constants and 40Ar*/40K for the Fish Canyon sanidine standard, and improved accuracy for 40Ar/39Ar geochronology" by PR Renne et al.

(2010): Geochimica et Cosmochimica Acta, v. 75, no. 17, p. 5097-5100.

Renne, P. R., Deino, A. L., Hilgen, F. J., Kuiper, K. F., Mark, D. F., Mitchell, W. S., Morgan, L. E., Mundil, R., and Smit, J., 2013, Time scales of critical events around the Cretaceous-Paleogene boundary: Science, v. 339, no. 6120, p. 684-687.

Rivera, T. A., 2013, Geomagnetic reversal boundaries of the last 3 million years - What are their real ages?, Doctoral thesis, Roskilde University, p. 208.

Rizvanova, N., Levchenkov, O., Belous, A., Bezmen, N., Maslenikov, A., Komarov, A., Makeev, A., and Levskiy, L., 2000, Zircon reaction and stability of the U-Pb isotope system during interaction with carbonate fluid: experimental hydrothermal study: Contributions to Mineralogy and Petrology, v. 139, no. 1, p. 101-114.

Roddick, J. C., 1978, The application of isochron diagrams in 40Ar-39Ar dating: A discussion: Earth and Planetary Science Letters, v. 41, no. 2, p. 233-244.

Sazonova, L., Milyavskii, V., Borodina, T., Sokolov, S., and Zhuk, A., 2007, Shock metamorphism of plagioclase and amphibole (experimental data): Izvestiya, Physics of the Solid Earth, v. 43, no. 8, p. 707-712.

Schaen, A. J., Jicha, B. R., Hodges, K. V., Vermeesch, P., Stelten, M. E., Mercer, C. M., Phillips, D., Rivera, T. A., Jourdan, F., and Matchan, E. L., 2020, Interpreting and reporting 40Ar/39Ar geochronologic data: GSA Bulletin.

Schaepe, K., Jungnickel, H., Heinrich, T., Tentschert, J., Luch, A., and Unger, W. E. S., 2020, Chapter 4.7 - Secondary ion mass spectrometry, in Hodoroaba, V.-D., Unger, W. E. S., and Shard, A. G., eds., Characterization of Nanoparticles, Elsevier, p. 481-509.

Schaltegger, U., Schmitt, A., and Horstwood, M., 2015, U–Th–Pb zircon geochronology by ID-TIMS, SIMS, and laser ablation ICP-MS: recipes, interpretations, and opportunities: Chemical Geology, v. 402, p. 89-110.

Schärer, U., and Deutsch, A., 1990, Isotope systematics and shock-wave metamorphism: II. U-Pb and Rb-Sr in naturally shocked rocks; the Haughton Impact Structure, Canada: Geochimica et Cosmochimica Acta, v. 54, no. 12, p. 3435-3447.

Schmieder, M., and Jourdan, F., 2013, The Lappajärvi impact structure (Finland): Age, duration of crater cooling, and implications for early life: Geochimica et Cosmochimica Acta, v. 112, p. 321-339.

Schmieder, M., Kennedy, T., Jourdan, F., Buchner, E., and Reimold, W. U., 2018, A high-precision 40Ar/39Ar age for the Nördlinger Ries impact crater, Germany, and implications for the accurate dating of terrestrial impact events: Geochimica et Cosmochimica Acta, v. 220, p. 146-157.

Schmieder, M., and Kring, D. A., 2020, Earth's Impact Events Through Geologic Time: A List of Recommended Ages for Terrestrial Impact Structures and Deposits: Astrobiology, v. 20, no. 1, p. 91-141.

Schmieder, M., Tohver, E., Jourdan, F., Denyszyn, S. W., and Haines, P. W., 2015, Zircons from the Acraman impact melt rock (South Australia): Shock metamorphism, U–Pb and 40Ar/39Ar systematics, and implications for the isotopic dating of impact events: Geochimica et Cosmochimica Acta, v. 161, p. 71-100.

Schmitz, B., Häggström, T., and Tassinari, M., 2003, Sediment-dispersed extraterrestrial chromite traces a major asteroid disruption event: Science, v. 300, no. 5621, p. 961-964.

Schmitz, B., Tassinari, M., and Peucker-Ehrenbrink, B., 2001, A rain of ordinary chondritic meteorites in the early Ordovician: Earth and Planetary Science Letters, v. 194, no. 1-2, p. 1-15.

Schoene, B., 2014, U-Th-Pb Geochronology, in Holland, H. D., and Turekian, K. K., eds., Treatise on geochemistry, Elsevier Science, p. 341-370.

Schoene, B., Samperton, K. M., Eddy, M. P., Keller, G., Adatte, T., Bowring, S. A., Khadri, S. F., and Gertsch, B., 2015, U-Pb geochronology of the Deccan Traps and relation to the end-Cretaceous mass extinction: Science, v. 347, no. 6218, p. 182-184.

Schulte, P., Alegret, L., Arenillas, I., Arz, J. A., Barton, P. J., Bown, P. R., Bralower, T. J., Christeson, G. L., Claeys, P., Cockell, C. S., Collins, G. S., Deutsch, A., Goldin, T. J., Goto, K., Grajales-Nishimura, J. M., Grieve, R. A. F., Gulick, S. P. S., Johnson, K. R., Kiessling, W., Koeberl, C., Kring, D. A., MacLeod, K. G., Matsui, T., Melosh, J., Montanari, A., Morgan, J. V., Neal, C. R., Nichols, D. J., Norris, R. D., Pierazzo, E., Ravizza, G., Rebolledo-Vieyra, M., Reimold, W. U., Robin, E., Salge, T., Speijer, R. P., Sweet, A. R., Urrutia-Fucugauchi, J., Vajda, V., Whalen, M. T., and Willumsen, P. S., 2010, The Chicxulub Asteroid Impact and Mass Extinction at the Cretaceous-Paleogene Boundary: Science, v. 327, no. 5970, p. 1214-1218.

Schwarz, W. H., Hanel, M., and Trieloff, M., 2020, U-Pb dating of zircons from an impact melt of the Nördlinger Ries crater: Meteoritics & Planetary Science, v. 55, no. 2, p. 312-325.

Sepúlveda, J., Wendler, J. E., Summons, R. E., and Hinrichs, K.-U., 2009, Rapid Resurgence of Marine Productivity After the Cretaceous-Paleogene Mass Extinction: Science, v. 326, no. 5949, p. 129-132.

Shand, S. J., 1916, The pseudotachylyte of Parijs (Orange free State), and its relation to 'Trap-Shotten Gneiss' and 'Flinty Crush-rock': Quarterly Journal of the Geological Society, v. 72, no. 1-4, p. 198-221.

Singleton, A., Osinski, G., and Shieh, S., 2015, Microscopic effects of shock metamorphism in zircons from the Haughton impact structure, Canada: Geological Society of America Special Papers, v. 518, p. 135-148.

Sinha, A. K., Wayne, D. M., and Hewitt, D. A., 1992, The hydrothermal stability of zircon: preliminary experimental and isotopic studies: Geochimica et Cosmochimica Acta, v. 56, no. 9, p. 3551-3560.

Smythe, W., and Hemmendinger, A., 1937, The radioactive isotope of potassium: Physical Review, v. 51, no. 3, p. 178.

Söderlund, U., Elming, S.-Å., Ernst, R. E., and Schissel, D., 2006, The central Scandinavian dolerite Group—Protracted hotspot activity or back-arc magmatism?: Constraints from U–Pb baddeleyite geochronology and Hf isotopic data: Precambrian Research, v. 150, no. 3-4, p. 136-152.

Söderlund, U., Hellström, F., and Kamo, S., 2008, Geochronology of high-pressure mafic granulite dykes in SW Sweden: tracking the P–T–t path of metamorphism using Hf isotopes in zircon and baddeleyite: Journal of Metamorphic Geology, v. 26, no. 5, p. 539-560.

Stacey, J. S., and Kramers, J. D., 1975, Approximation of terrestrial lead isotope evolution by a two-stage model: Earth and Planetary Science Letters, v. 26, no. 2, p. 207-221.

Steiger, R. H., and Jäger, E., 1977, Subcommission on geochronology: Convention on the use of decay constants in geo- and cosmochronology: Earth and Planetary Science Letters, v. 36, no. 3, p. 359-362.

Stephan, T., and Jessberger, E. K., 1992, Isotope systematics and shock-wave metamorphism: III. K-Ar in experimentally and naturally shocked rocks; the Haughton impact structure, Canada: Geochimica et cosmochimica acta, v. 56, no. 4, p. 1591-1605.

Stöffler, D., 1971, Progressive metamorphism and classification of shocked and brecciated crystalline rocks at impact craters: Journal of Geophysical Research, v. 76, no. 23, p. 5541-5551.

-, 1972, Deformation and transformation of rock-forming minerals by natural and experimental shock processes. I-Behavior of minerals under shock compression.: Fortschritte der Mineralogie, v. 49, p. 50-113.

Storey, M., Roberts, R. G., and Saidin, M., 2012, Astronomically calibrated 40Ar/39Ar age for the Toba supereruption and global synchronization of late Quaternary records: Proceedings of the National Academy of Sciences, v. 109, no. 46, p. 18684-18688.

Stosch, H.-G., 1999, Einführung in die Isotopengeochemie, Institut für Mineralogie und Geochemie.

Swisher, C. C., Grajales-Nishimura, J. M., Montanari, A., Margolis, S. V., Claeys, P., Alvarez, W., Renne, P., Cedillo-Pardoa, E., Maurrasse, F. J. M. R., and Curtis, G. H., 1992, Coeval 40Ar/39Ar ages of 65.0 million years ago from Chicxulub crater melt rock and Cretaceous-Tertiary boundary tektites: Science, v. 257, no. 5072, p. 954-958.

Tagami, T., Carter, A., and Hurford, A. J., 1996, Natural long-term annealing of the zircon fission-track system in Vienna Basin deep borehole samples: constraints upon the partial annealing zone and closure temperature: Chemical Geology, v. 130, no. 1-2, p. 147-157.

Tagami, T., and Shimada, C., 1996, Natural long-term annealing of the zircon fission track system around a granitic pluton: Journal of Geophysical Research: Solid Earth, v. 101, no. B4, p. 8245-8255.

Tilton, G. R., 1960, Volume diffusion as a mechanism for discordant lead ages: Journal of Geophysical Research, v. 65, no. 9, p. 2933-2945.

Timms, N. E., Erickson, T. M., Pearce, M. A., Cavosie, A. J., Schmieder, M., Tohver, E., Reddy, S. M., Zanetti, M. R., Nemchin, A. A., and Wittmann, A., 2017, A pressure-temperature phase diagram for zircon at extreme conditions: Earth-Science Reviews, v. 165, p. 185-202.

Turner, G., 1971, Argon 40-argon 39 dating: The optimization of irradiation parameters: Earth and Planetary Science Letters, v. 10, no. 2, p. 227-234.

Turner, G., and Cadogan, P. H., 1974, Possible effects of 39Ar recoil in 40Ar-39Ar dating: Geochimica et Cosmochimica Acta, v. 2, p. 1601-1615.

Ul-Hamid, A., 2018, A Beginners' Guide to Scanning Electron Microscopy, Springer.

Valley, J., Komor, S., Baker, K., Jeffrey, A., Kaplan, I., and Raheim, A., 1988, Calcite crack cements in granite from the Siljan Ring, Sweden: Stable isotopic results, Deep drilling in crystalline bedrock, Volume 1, Springer Berlin, p. 156-179.

Von Weizsäcker, C., 1937, Über die Möglichkeit eines dualen β-Zerfalls von Kalium: Physikalische Zeitschrift, v. 38, p. 623-624.

Wartho, J. A., Van Soest, M. C., King Jr, D. T., and Petruny, L. W., 2012, An (U-Th)/He age for the shallow-marine Wetumpka impact structure, Alabama, USA: Meteoritics & Planetary Science, v. 47, no. 8, p. 1243-1255.

Watson, E. B., Chemiak, D., Hanchar, J. M., Harrison, T. M., and Wark, D., 1997, The incorporation of Pb into zircon: Chemical Geology, v. 141, no. 1-2, p. 19-31.

Wetherill, G. W., 1956, Discordant uranium-lead ages, I: Eos, Transactions American Geophysical Union, v. 37, no. 3, p. 320-326.

Widdowson, M., Pringle, M., and Fernandez, O., 2000, A post K–T boundary (Early Palaeocene) age for Deccan-type feeder dykes, Goa, India: Journal of Petrology, v. 41, no. 7, p. 1177-1194.

Wiedenbeck, M., Alle, P., Corfu, F., Griffin, W., Meier, M., Oberli, F. v., Quadt, A. v., Roddick, J., and Spiegel, W., 1995, Three natural zircon standards for U-Th-Pb, Lu-Hf, trace element and REE analyses: Geostandards newsletter, v. 19, no. 1, p. 1-23.

Wiedenbeck, 2017, Course notes – Introduction to Secondary Ion Mass Spectrometry, 13-17 November 2017, GFZ Potsdam, Germany.

Wielicki, M. M., Harrison, T. M., and Stockli, D., 2014, Dating terrestrial impact structures: U-Pb depth profiles and (U-Th)/He ages of zircon: Geophysical Research Letters, v. 41, no. 12, p. 4168-4175.

Wittmann, A., Kenkmann, T., Schmitt, R. T., and Stöffler, D., 2006, Shock-metamorphosed zircon in terrestrial impact craters: Meteoritics & Planetary Science, v. 41, no. 3, p. 433-454.

Yamada, R., Tagami, T., Nishimura, S., and Ito, H., 1995, Annealing kinetics of fission tracks in zircon: an experimental study: Chemical geology, v. 122, no. 1-4, p. 249-258.

Zhang, A. C., Hsu, W. B., Li, X. H., Ming, H. L., Li, Q. L., Liu, Y., and Tang, G. Q., 2011, Impact melting of lunar meteorite Dhofar 458: Evidence from polycrystalline texture and decomposition of zircon: Meteoritics & Planetary Science, v. 46, no. 1, p. 103-115.

Svensk sammanfattning

När en nedslagskrater bildas frigörs enorma mängder energi under väldigt kort tid. Detta resulterar i fysiska förhållanden (extrema temperaturer och tryck) som inte förekommer vid några andra naturliga geologiska processer på jorden, så som vid vulkanutbrott eller jordskalv. På grund av destruktiva geologiska processer, till exempel erosion, bergskedjebildning och subduktionszoner, är nedslagsstrukturer relativt ovanliga på jordytan. Idag känner vi bara till ungefär 200 nedslagsstrukturer på jorden. Minst en gång i jordens historia har en katastrofal kollision utlöst en biologisk kris på jorden. Det var för cirka 66 miljoner år sedan, när en ca. 10 km stor asteroid kolliderade med jorden strax utanför Yucatanhalvön i nuvarande Mexiko, och skapade den 150 km stora Chicxulubkratern, vilket ledde till ett massutdöende på jorden, då till exempel dinosaurierna dog ut. Nedslagskratrar kan också vara ekonomiskt intressanta, då stora volymer uppsprucket berg genomströmmas av varmt vatten efter nedslaget. Det här kan leda till bildning av mineraliseringar av ekonomiskt intressanta grundämnen. Ett exempel är Sudbury strukturen i Kanada, där man bryter bland annat koppar och nickel. Det uppspruckna berget kan även tjäna som fällor för kolväten och nedslagsbildade bergarter används också som byggsten, till exempel bergarten suevit från Riesstrukturen i Tyskland. Sedan 1960-talet, när forskarsamhället insåg att nedslagshändelser har spelat en viktig roll i formandet av jordens yta och för att förändra dess geologiska historia, har vi lärt oss mycket om jordens nedslagskratrar och processerna som råder vid bildandet av en krater. För att vi ska kunna förstå hur nedslagshändelser påverkat jorden behöver man känna till när specifika nedslagsstrukturer bildades. Åldrar behövs också för att man ska kunna analysera hur inflödet av kraterbildande kroppar till jorden sett ut, eller förändrats, över tid. I förlängningen vill man också förstå vad det här kan ha för konsekvenser för jorden i framtiden. Majoriteten av nedslagskratrar på jorden är dock inte väl daterade, eller i vissa fall är åldern till och med i princip okänd.

Den här avhandlingens fokus ligger påradiometriska dateringar av tre svenska nedslagskratrar (Siljan, Mien och Hummeln) och en rysk nedslagskrater (Puchezh-Katunki). Radiometrisk datering möjliggör bestämning av absoluta åldrar baserade på radioaktivt sönderfall av instabila, radioaktiva föräldraisotoper till stabila dotterisotoper. Sönderfallet leder till en minskning av föräldrarisotoper och därmed en ökning av dotterisotoper som ackumuleras i ett slutet system över tid. Bildningsåldern kan då

beräknas utifrån förhållandet mellan nybildade dotterisotoper och föräldraisotoper som fortfarande finns kvar i systemet. Idag finns det ett brett spektrum av så kallade kronometrar, som man kan likna vid olika typer av klockor, baserade på olika radioaktiva sönderfallssystem. Dessa kan användas för att åldersbestämma händelser från de tidigaste perioderna av jordens historia till nyare geologiska händelser. I denna avhandling användes $^{40}Ar/^{39}Ar$- och U-Pb-metoderna för att undersöka om och hur dessa isotopsystem påverkas av en nedslagshändelse samt de processer som följer efter nedslaget. För att göra det analyserades både enskilda mineralkorn av zirkon, amfibol och biotit, och hela prover av berg som bildats vid nedslag genom uppsmältning av målberggrunden, så kallad nedslagssmälta.

När kratern Siljan bildades så lyftes djupt belägen berggrund upp till grunda nivåer i jordskorpan. Det sker på grund av att det stora hål som bildas när en stor himlakropp träffar jordytan inte är gravitationsmässigt stabilt, utan det fylls delvis igen genom att djupt belägen berggrund lyfts upp. Genom att studera zirkoner från den tidigare djupt belägna berggrunden så kunde vi visa att de mineralkorn som varit belägna djupt i jordskorpan under andra temperaturförhållanden än korn närmre ytan behållit ett mer stabilt U-Pb-system, som resulterade i mer lättutlästa åldrar. Bly, som bildas genom sönderfall av uran, har en tendens att smita när zirkoner kommer i kontakt med till exempel vatten, men de förhållanden som råder djupare ner i jordskorpan förhindrar att det här sker. De analyserade zirkonkristallerna som kom från prover utanför Siljansringen visade mer tecken på att vara påverkade av förlust av bly. I en av de andra studierna som presenteras i den här avhandlingen kunde vi vidare visa att också $^{40}Ar/^{39}Ar$-systemet i mineralkorn påverkats av nedslaget vid Siljan. Mineralen biotit och amfibol, som innehåller kalium som sönderfaller till argon, visar hur berggrunden påverkats genom att varma vätskeblandningar, så kallade hydrotermala lösningar, flödat genom alla de sprickor som bildades vid nedslaget.

Med $^{40}Ar/^{39}Ar$-systemet analyserades också prover från Hummeln i Småland och nedslagskratern Puchezh-Katunki i Ryssland. Datan visade att halten av dotterisotoper påverkats av respektive nedslag, och vi kunde dra slutsatsen att nedslagssmälta från Puchezh-Katunki, och alltså själva kratern, bildades för 192-196 miljoner år sedan. $^{40}Ar/^{39}Ar$-datan från proverna från Hummeln visade sig vara mer svårtolkade då de inte hade påverkats i samma utsträckning.

Vidare analyserades också zirkoner från nedslagskratern Mien i Småland med hjälp av U-Pb-metoden. Tidigare var åldern på nedslaget, ca. 122 miljoner år, känd genom analys med $^{40}Ar/^{39}Ar$-metoden, men vi kunde också visa att zirkonerna gav en statistiskt mer tillförlitlig ålder på nedslaget (119.7 ± 1.1 Ma). Studien visade också at bildningen av chocktexturer i zirkon främjas i korn som skadats av strålning på grund av U-Pb sönderfall.

Supplementary A

Conference abstracts are not included in this thesis.

Herrmann, M., Alwmark, C., Scherstén, A., Næraa, T., and Söderlund, U., 2018, LA-ICP-MS U-Pb Dating of Shocked Zircons of Siljan Impact Structure, Sweden – Impact-related Ages or Post-impact Hydrothermal Pb loss? 81st Annual Meeting of the Meteoritical Society. Abstract #6218.

Herrmann, M., Alwmark, C., and Storey, M., 2019, $^{40}Ar/^{39}Ar$ dating of the Hummeln and Mien impact structures, Sweden. International Conference "Impact and their role in the Evolution of Life".

Herrmann, M., Martell., J., Alwmark, C., and Whitehouse, M. J., 2019, SIMS U-Pb dating and EBSD structural analyses of granular zircon from the Mien impact structure, Sweden. Large Meteorite Impacts and Planetary Evolution VI. Abstract #5022.

All Supplementary and Data Repository of paper I to IV can be found online at http://lup.lub.lu.se/record/0502696f-26cd-4ca3-af64-dcb438c3a2d8

The online links to the individual supplementary material of paper I to IV are:

Paper I: https://lup.lub.lu.se/search/ws/files/82600288/Paper_I_Supplementary_.pdf

Paper II: https://lup.lub.lu.se/search/ws/files/82600290/Paper_II_Data_Repository.pdf

Paper III: https://lup.lub.lu.se/search/ws/files/82600292/Paper_III_Supplementary.pdf

Paper IV
Item DR1: https://lup.lub.lu.se/search/ws/files/82600294/Paper_IV_Data_Repository_1.pdf
Item DR 2: https://lup.lub.lu.se/search/ws/files/82600296/Paper_IV_Data_Repository_2.pdf
Item DR 3: https://lup.lub.lu.se/search/ws/files/82600298/Paper_IV_Data_Repository_3.pdf
Item DR 4: https://lup.lub.lu.se/search/ws/files/82600300/Paper_IV_Data_Repository_4.pdf
Item DR 5: https://lup.lub.lu.se/search/ws/files/82600302/Paper_IV_Data_Repository_5.pdf
Item DR 6: https://lup.lub.lu.se/search/ws/files/82600304/Paper_IV_Data_Repository_6.pdf